

Probing Nano-Environments of Single Molecules

Habilitationsschrift

zur Erlangung der *Venia Legendi*
für das Fach Physikalische Chemie

vorgelegt von

Taras Plakhotnik

Laboratorium für Physikalische Chemie

Eidgenössische Technische Hochschule

Zürich 2000

References were updated: 22.05.2001

Part of this work is based on the following publications:

- [1] T. Plakhotnik, D. Walser, M. Pirota, A. Renn, U.P. Wild. Nonlinear Spectroscopy of a Single Quantum System: Two-Photon Absorption of a Single Molecule. *Science* **271** (1996) 1703.
- [2] T. Plakhotnik, D. Walser, A. Renn, U. P. Wild. Light induced single molecule frequency shift. *Phys. Rev. Lett.* **77** (1996) 5365.
- [3] D. Walser, T. Plakhotnik, A. Renn, U. P. Wild. One- and two-photon spectroscopy on single molecules of diphenyloctatetraene. *Chem. Phys. Lett.* **270** (1997) 16.
- [4] T. Plakhotnik, D. Walser. Time resolved single molecule spectroscopy. *Phys. Rev. Lett.* **80** (1998) 4064.
- [5] E. A. Donley, T. Plakhotnik, H. Bach, and U. P. Wild, Coupling constant distribution measured for dynamical interactions between probe molecules and an amorphous polymer host, *Opt. Spectrosc. (Engl. Transl.)* **87** (1999) 616.
- [6] T. Plakhotnik. Time-dependent single molecule spectral lines. *Phys. Rev. B* **59** (1999) 4658.
- [7] E. A. Donley, H. Bach, U. P. Wild, T. Plakhotnik. Coupling strength distributions for dynamic interactions experienced by probe molecules in a polymer host. *J. Phys. Chem. A* **103** (1999) 2282.
- [8] E. A. Donley, V. Burzomato, U. P. Wild, T. Plakhotnik. The distribution of linewidth of single probe molecules in a crystalline host at milliKelvin temperatures. *J. Lumin.* **84-85** (1999) 255.
- [9] T. Plakhotnik. Spectral lines of single molecules in a fluctuating environment. *J. Lumin.* **84-85** (1999) 221.
- [10] E. A. Donley, S. Bonsma, V. Palm, V. Burzomato, U. P. Wild, T. Plakhotnik. Zero-phonon lines of single molecules in polyethylene down to milliKelvin temperatures. *J. Lumin.* **87-89** (2000) 109.
- [11] T. Plakhotnik, E.A. Donley. Statistics of single terrylene molecule in hexadecane. *J. Lumin.* **86** (2000) 175.
- [12] D. Walser, G. Zumofen, T. Plakhotnik. Symmetry breaking and spectra of diphenyloctatetraene in n-alkanes, *J. Chem. Phys.* **113** (2000) 8047.
- [13] T. Nonn, T. Plakhotnik. Non-Lorentzian single-molecule line shape: Pseudolocal phonons and coherence transfer. *Phys. Rev. Lett.* **85** (2000) 1556.
- [14] T. Plakhotnik. Single molecules in varying environments (review article). *Photonics Science News* **6** (2000) 148.
- [15] E. A. Donley, T. Plakhotnik. Spectral diffusion in polyethylene: Single molecule studies performed between 30 mK and 1.8 K. *J. Chem. Phys.* **113** (2000) 9294
- [16] D. Walser, G. Zumofen, A. Renn, T. Plakhotnik. Matrix dynamics and nonlinear effects in one- and two-photon single molecule spectroscopy. *J. Phys. Chem. A* **105** (2001) 3022.
- [17] E. A. Donley, T. Plakhotnik. Luminescence lifetimes of single molecules in disordered media. *J. Chem. Phys.* **114** (2001).
- [18] T. Plakhotnik. Spectral line shapes of single molecules beyond the sudden jump model. *J. Chem. Phys.* **114** (2001) 5631.
- [19] E. A. Donley, T. Plakhotnik. Statistics for single-molecule spectroscopy data, *Single Molecules* **2** (2001) 23.
- [20] T. Nonn, T. Plakhotnik. Fluorescence excitation spectroscopy of vibronic transitions in single molecules. *Chem. Phys. Lett.* **336** (2001) 97.

Contents

| | |
|---|-----|
| Abbreviations | 4 |
| Preface | 5 |
| Introduction | 7 |
| A Tour of Single Molecule Spectroscopy | 8 |
| Molecules Interact with Light | 11 |
| Model for Molecule's Environment | 20 |
| Principles of Data Analysis | 24 |
| Intensity-Time-Frequency Correlation Spectroscopy | 27 |
| Details | 30 |
| Nonequilibrium Phonons and ac-Stark Effect | 43 |
| Details | 47 |
| Non-Lorentzian Line Shapes | 63 |
| Details | 66 |
| Spectral Diffusion in Polyethylene and other Polymers | 82 |
| Details | 86 |
| Distribution of Radiative Lifetimes | 97 |
| Details | 101 |
| Perspectives | 111 |
| Acknowledgments | 113 |
| References | 114 |
| Lebenslauf | 122 |

Abbreviations

| | |
|------|---|
| ACF | Auto correlation function |
| cps | Counts per second |
| CLT | Central limit theorem |
| COA | Cut-off approximation |
| DPOT | all-trans-1,8-diphenyl-1,3,5,7-octatetraene |
| FWHM | Full width half maximum |
| HWHM | Half width at half maximum |
| ISC | Inter system crossing |
| ITFC | Intensity-Time-Frequency Correlation |
| LISD | Light induced spectral diffusion |
| ME | Master equation |
| MW | Microwave |
| NQP | Non-equilibrium phonons |
| OPE | one-photon excitation |
| PDF | Probability density function |
| Pc | Pentacene |
| PE | Polyethylene |
| PLV | Pseudo localized vibration |
| p-TP | p-terphenyl |
| PVB | Polyvinylbutyral |
| SD | Spectral diffusion |
| SFS | Statistical fine structure |
| SJM | Sudden jump model |
| SM | Single molecule |
| SMS | Single molecule spectroscopy |
| TD | n-tetradecane |
| TLS | Two-level system |
| TPE | Two-photon excitation |
| ZPL | Zero phonon line |

I. Preface

The field of single molecules is growing rapidly [1- 8]; particularly in its application to the study of biological systems and chemical processes [1, 9]. The main idea behind these applications is based on the sensitivity of a single molecule to its nano-environment. But this idea is productive only if basic principles of the data analysis and most essential molecule-environment interactions are understood. For such studies, biological objects may not be the best choice because of their complexity. In this *Habilitationsschrift* several effects that were investigated in more simple and better understood systems (polymers and crystals) are presented.

If the difference between single molecules and ensemble measurements has to be expressed in a single word, the word is *fluctuations*. Here we use *fluctuations* in its broadest sense, including both static and dynamic (on the time scale of our measurements) variations of molecular environments in a macroscopically homogeneous sample. Fluctuations are usually unobservable in ensemble measurements and direct access to fluctuations (which are characterized by the statistical distribution function) make single molecules an attractive analytical tool. All the effects and theoretical considerations discussed below are related to or deal with fluctuations which are the most common and most striking feature of single molecule studies.

First the concept of time-dependent spectra is introduced. This concept is nontrivial when applied to a single molecule. Second, an effect of equilibrium and nonequilibrium phonons emitted owing to nonradiative processes in the matrix is analyzed. Third, we consider precise measurements of excitation line shapes in the presence of a pseudolocal vibration. It is shown that the line deviates from well-known Lorentzian which is the response function of a classical harmonic oscillator. The last two chapters are closely related. A fourth topic deals with the distribution of linewidths for single terrylene molecules in polyethylene which are investigated in a broad temperature range. The distributions are compared to the distributions simulated with the tunnelling two-level system model for low-temperature glasses. This comparison revealed a distribution of coupling constants between the probe molecules and the two-level systems and gives an

evidence for the distribution of radiative lifetimes. In detail the influence of the environments on the radiative lifetimes of an optical transition is considered in the final chapter.

Each chapter (except for *Introduction*) consists of two sections — a brief review and *Details*. In the first section the main results are explained in a self consistent manner. *Details* gives a more complete account about the subject and can be considered as a supplement to the first part. Theoretical concepts and models are introduced gradually when corresponding experimental results are discussed.

II. Introduction

“An atom is a body which cannot be cut in two. A molecule is the smallest possible portion of a particular substance. No one has ever seen or handled a single molecule. Molecular science, therefore, is one of those branches of study which deal with things invisible and imperceptible by our senses, and which cannot be subjected to direct experiment.” — J.C. Maxwell in a lecture before the British Association at Bradford (1873).

“... we never experiment with just one electron or atom or molecule. In thought experiments we sometimes assume that we do; this invariably entails ridiculous consequences... In the first place it is fair to state that we are not experimenting with single particles, any more than we can raise Ichthyosauria in the zoo.” E. Schrödinger, Br. J. Philos. Sci. III, 1952, August

Despite being about ten years old [10, 11], single molecule studies are still a new subject for most physicists and chemists. The technology was available to allow this field of scientific activities to emerge thirty years ago. However, there is a substantial psychological barrier (partially built on a historical scepticism which surrounds this subject) to the idea of working with just one molecule and yet achieving a reasonable signal-to-noise ratio. Assuming that the reader (if he or she is not familiar with the field) can also have such a barrier, we begin with a few simple and appealing examples.

A Tour of Single Molecule Spectroscopy

In this section, the technical details of the experimental apparatuses are kept at a minimum. We simply state that under certain conditions (photo stability, low intersystem crossing, high emission rates, high luminescence quantum yield, etc.) it is possible to detect a signal from one molecule. Moreover not simply to detect but also to measure spectra and other parameters for that molecule. One should not think about single-molecule spectra as something barely visible. With an appropriate system, the signal-to-background ratio can be higher than 1000:1. In Fig. 1 such a spectrum is shown for terrylene in a naphthalene crystal. Each peak corresponds to a 0-0 electronic transition in a single terrylene molecule. The signal-to-background ratio for the molecule E is approximately 1000:1 and the dark counts of the photomultiplier contribute about 50% to the background level.

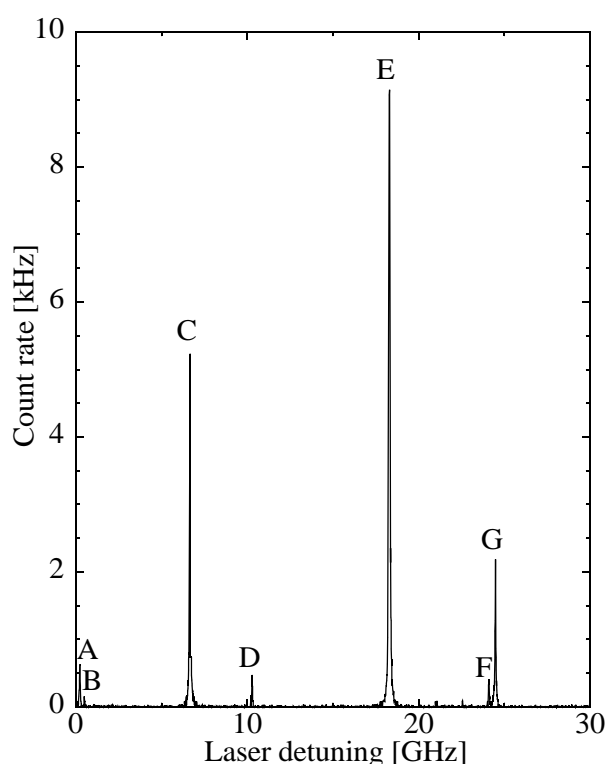


Fig. 1 These seven single-molecule lines of terrylene in a naphthalene crystal measured at a temperature of 1.65 K show that the noise in single molecule spectra can be comparable to that in bulk measurements.

The sensitivity and selectivity of single-molecule spectroscopy is such that it is also possible to measure a single-molecule analogue to second harmonic generation. Two-photon excited emission spectra of a single molecule were first reported in [12] for diphenylotatetraene (DPOT) doped in a n-tetradecane (TD) crystal. With a few MW/cm^2 single mode infrared laser intensity, the transition from the 1^1A_g ground state to the first excited singlet state 2^1A_g , which is one-photon electric dipole forbidden by parity, was excited by two photons. Weak one-photon emission proportional to the square of the laser power

could be observed, as a result of coupling of the 2^1A_g state with the nearby 1^1B_u state. In

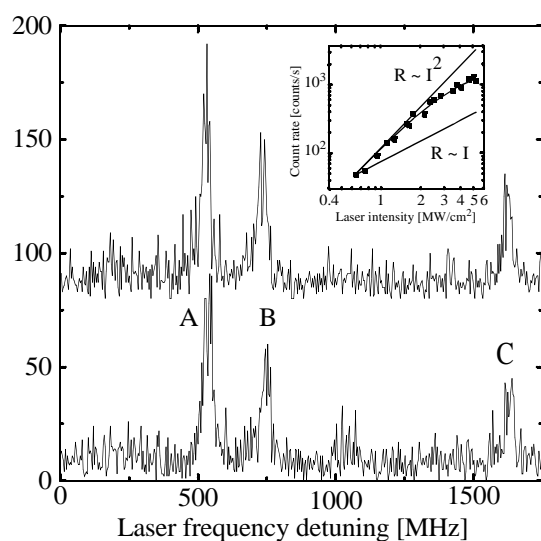


Fig. 2 A high resolution scan in the wing of the inhomogeneous band shows three SM lines labeled with A, B, and C, the laser power was 2.5 MW/cm^2 . The second scan (shifted up for clarity) shows data reproducibility. Dependence of the count rate R of the molecule B on the laser intensity. The lines $R \sim I$ and $R \sim I^2$ are shown for comparison.

[12] the saturation behavior under two-photon excitation (TPE) was characterized, and the photophysical parameters were measured. These experiments opened new possibilities for high resolution nonlinear spectroscopy.

An interesting point which might not be obvious for non-specialists, and therefore deserves a brief discussion here, is how to prove that the observed peak corresponds to a single molecule but not to several molecules with accidentally overlapping 0-0 lines. This proof can be obtained if the second order correlation function of the detected photo counts is measured. Such a correlation function is defined by the relation $g^{(2)}(\tau) = \langle n(t)n(t+\tau) \rangle / \langle n(t) \rangle^2$, where $n(t)dt$ and $n(t+\tau)dt$ are the number of photons detected within the time interval dt at times t and $t+\tau$ respectively. $g^{(2)}(\tau)d\tau$ is nothing more than the normalized conditional probability to detect a photon at time $t+\tau$ if a photon was counted at time t . The emission of a single molecule, or better to say, a single quantum system has a peculiarity that such a conditional probability approaches zero when $\tau \rightarrow 0$ [13]. This is the so-called antibunching of single-molecule luminescence. A molecule can not emit the second photon right after the first because it takes time for the molecule to be excited. It can be shown that the probability to emit the second photon at time τ is equal to the probability to find the system in the excited state provided that the system was in the ground state at zero time, which is indicated by the first detected photon. Such correlation functions have been measured for a number of quantum systems [14-16]. An example is shown in Fig. 3. The correlation function was measured for a single terrylene molecule embedded in a naphthalene crystal. In addition to the antibunching

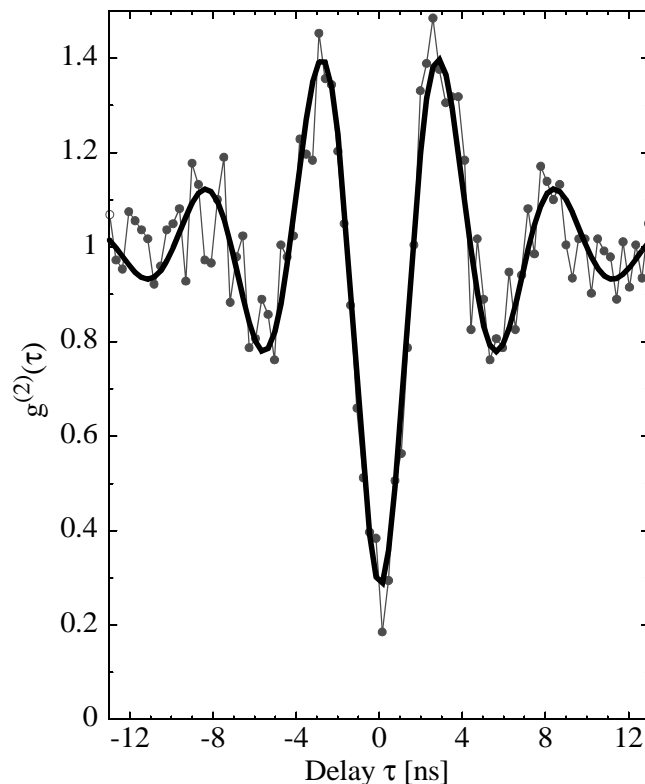


Fig. 3 Antibunching of single-molecule photo counts. The data were fitted to the function $1 - A \cdot \exp(-|\tau|\Theta) \cdot [\Theta/\Omega \cdot \sin(\Omega|\tau) + \cos(\Omega|\tau)]$ [17], where the two-parameter fit gives the following results: $\Omega = 1.13$ GHz and $A = 0.72$. The linewidth at 1.65 K and life time limited linewidth were measured independently: $\Gamma_v = (\pi T_2)^{-1} = 52$ MHz and $(2\pi T_1)^{-1} = 42$ MHz. Consequently the third parameter was fixed at $\Theta = (1 + T_2/T_1)/(2T_2) = 0.21$ GHz.

at $\tau = 0$, a few oscillations are clearly visible. These oscillations (Rabi oscillations) reflect changes in the population of the excited state under resonance excitation. The high laser power required to make oscillations visible was the reason for the relatively high background and as a consequence the dip at $\tau = 0$ ns does not reach zero. The presence of negative delay times should not confuse the reader. In the actual experiment two photo detectors were used. The signal from the first detector was delayed by 31 ns and was used as a start signal for a clock. The signal from the second detector produced a stop signal for the clock. A negative time means simply that the delay between the “start” count and the delayed “stop” count was smaller than the 31 ns which were then subtracted from τ . Of course for a well-studied system it is not necessary to do correlation measurements every time. The judgement can be based on the observed linewidths of distinct peaks, their shape, and spectral density. But a new system should be considered very carefully before a conclusion about the achievement of single-molecule sensitivity can be made. This be-

comes a nontrivial exercise if a Raman scattering signal rather than luminescence is detected [18, 19]. The Raman scattering does not show an antibunching effect and there is always room for speculation about whether a signal corresponds to one molecule or to a molecular cluster or a micro crystal.

Molecules Interact with Light

Despite its mysterious name, the main idea of single molecule spectroscopy (SMS) is very simple. Two things are of great importance. Only one probed molecule should be in the volume under study, and the light emitted by the molecule should be distinguishable from the experimental noise. The first condition is relatively easy to fulfill. A concentration of about $10^{-10} M$ and a volume of $10 \mu\text{m}^3$ are required. This can be straightforwardly achieved by focusing a laser beam into a very dilute solution. But in the same volume there will be about 10^{11} solvent molecules, and it is not easy to distinguish one molecule from one hundred billion others. To do this, we use spectroscopy, i.e. the interaction of electromagnetic radiation with matter. The stronger this interaction for the SM, the smaller the relative solvent contribution to the detected signal. A quantitative measure of this strength is the interaction cross section σ . The number of elementary acts caused by light of intensity I (pure absorptions, scatterings, ionizations, etc.) per second, is equal to σI , where I is measured in $\text{photons} \cdot \text{cm}^{-2} \cdot \text{s}^{-1}$. It is well known [20] that the resonance scattering cross section σ_{scat} and the total cross-section σ_{tot} (which includes scattering and pure absorption) for a two-level atom (or a classical harmonic oscillator) without radiationless energy losses are given by

$$\sigma_{scat} = \sigma_{tot} = 3\lambda^2 / (2\pi). \quad (1)$$

Thus they depend only on the light wavelength λ . σ_{scat} calculated according to Eq. (1) is of the order of 10^{-9}cm^2 for visible light, i.e. 10^5 times bigger than geometrical cross-section of a molecule!

Unfortunately, such a large value can be achieved only if a molecule or an atom does not interact with its environment. Such interactions increase the uncertainty in the transition frequency (the linewidth) from the radiative limit γ to a larger value Γ_0 . Under normal conditions the absorption cross-section of a good dye molecule in liquid solution is

only on the order of 10^{-17} cm^2 . Fortunately this interaction depends on temperature [21] and at liquid He temperature the cross-section may be closer to the one defined by Eq. (1). While the cross section increases, the spectral line narrows and may reach a width of a few MHz. This complicates the experimental setup since an optical liquid He cryostat is required to obtain the low temperature and a narrow band single mode laser is necessary to observe the narrow features. But it is well worth making the effort to build the apparatus. Their narrow lines makes SMs very sensitive to external perturbations, which is crucial for many applications.

In fact, because a molecule can be treated as a two-level system only approximately, its cross-section is:

$$\sigma_{tot} = Y \frac{3\lambda^2}{2\pi} \cdot \frac{\gamma}{\Gamma_0}, \quad (2)$$

where Y is the probability that when illuminated by light with wavelength λ a molecule will scatter a photon and return to its initial state, as it should in a truly two-level system. Excitation of molecular vibrations or phonons can cause Y to be less than one. On this ground Y can be called the generalized Frank-Condon factor. Many dye molecules have $Y = 0.1$ at low temperature, so their cross-section is 10^{-10} cm^2 . Since the number of solvent molecules is 10^{11} , the cross-section of the light-solvent interaction should be smaller than 10^{-21} cm^2 . For comparison, the nonresonance Raman scattering cross section of benzene is only 10^{-28} cm^2 [22], which is much smaller than the upper limit for the light-solve interaction cross-section. At room temperature, SM sensitivity can be achieved by reducing the excited volume using molecular monolayers and conventional [23] or near field [24] microscopy or by exploiting the time characteristics of luminescence [25].

In fact, the concentration of SMs in the solvent can be much higher than has been estimated above. Even doped in a crystal matrix, SMs have slightly different frequencies. A crystal is never ideal and every molecule has different surroundings and hence a different solvent shift of the resonance frequency [26]. The overlap of spectral lines builds the inhomogeneously broadened band. If many molecules are in the excited volume only those which are in resonance with the laser frequency are excited.

When many molecules are excited simultaneously the so-called statistical fine structure (SFS) is observed [27]. SFS is the reproducible fluctuation of the luminescence inten-

sity during the laser frequency scan, resulting from the statistical deviation of the number of molecules in the excited volume from the average value. In the case of Poisson's distribution law, the standard deviation is equal to the square root of the average number. The SFS contains information about the average spectral width of the SM lines building the inhomogeneous band. The auto-correlation function (ACF) of the SFS or the cross-correlation function between two scans made in the same spectral region, $g(\nu)$, is given by:

$$g(\nu) = \frac{\langle R_1(\nu')R_2(\nu' + \nu) \rangle - \langle R_1 \rangle \langle R_2 \rangle}{\sqrt{\{\langle R_1^2 \rangle - \langle R_1 \rangle^2\} \{\langle R_2^2 \rangle - \langle R_2 \rangle^2\}}}, \quad (3)$$

where $R_{1,2}(\nu)$ and $\langle R_{1,2} \rangle$ are the luminescence rates as a function of the laser frequency ν and their average values respectively. The function is a Lorentzian with a width of twice the SM linewidth [27], assuming a Lorentzian SM line shape.

A typical setup for SM spectroscopy is shown in Fig 4. The ability of a SM to emit

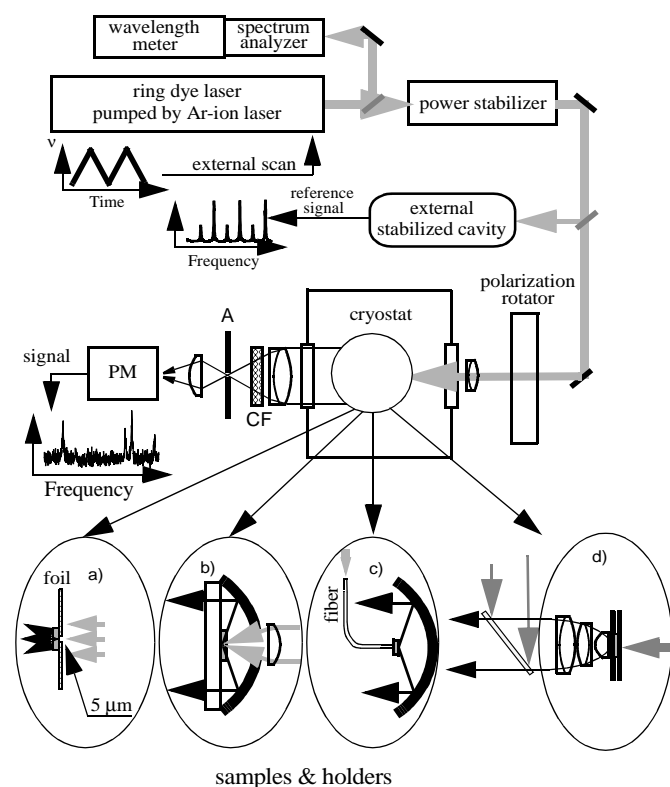


Fig. 4 Experimental setup. An intensity-stabilized beam from a ring dye laser illuminates the sample. The fluorescence is collected by a set of lenses outside the cryostat (a) and/or by a high efficiency optical system placed inside the cryostat (b, c, d) and directed onto a cooled photomultiplier (PM) with single-photon counting electronics. The scattered exciting laser light and, unfortunately, the 0-0 fluorescence are cut off with filters (CF). The laser frequency is monitored simultaneously with a spectrum analyzer and a wavemeter. In version b) the luminescence is collected by a parabolic mirror but excitation light is focused by an additional small lens. In version c) the sample is excited through a single mode fiber. In version d) the emitted light is gathered by a microscope objective with high numerical aperture. The thin grey lines show a version when the same objective is used for the excitation. Different combinations of these four versions, for example, a) and d), are possible. Using an aperture A yields a confocal setup.

light with a wavelength shifted to the red side of spectra from excitation wavelength (as a result of transitions to the vibrationally excited levels of the ground electronic state) is crucial in the case of one-photon excitation since the stray laser light must be cut off. Unfor-

tunately, the unshifted 0-0 emission is blocked too. In the case of two-photon excitation, when the exciting wavelength is twice the resonance one, light emitted by a SM at all frequencies can be collected [12].

This simple analysis implies that SM spectroscopy is an easy exercise and should be possible for almost every molecule. Unfortunately this is not true. Though the number of solvent-solute systems where SM spectral lines have been observed is growing, this number is still less than 30. Very careful choice of the chromophore and the host matrix is required. To understand the reason a more thorough analysis is necessary.

First of all, dark counts from the photo detector, luminescence from cutoff filters, impurities in the solvent, and statistical fluctuations of the detected signal, rather than inelastic scattering in the matrix give the main contribution to the experimental noise. Hence the absolute value of the SM emission rate R has to be large. We consider the molecular level scheme shown in Fig. 5. The electric field $\vec{E} = \vec{E}_0 \cos(\omega t)$ interacts with the 0-0 transition. This interaction is characterized by the Rabi frequency $\Omega = \vec{E}_0 \cdot \vec{d} / \hbar$. The steady state solution of the optical Bloch equations for $R = \rho_{22} / T_{rad}$, where T_{rad} is the radiative life time of the level 2 is

$$R = \frac{\Omega^2 T_1 T_2 / (2T_{rad})}{1 + ((\omega - \omega_0)T_2)^2 + \Omega^2 T_1 T_2 K}, \quad (4)$$

where ω_0 is the transition frequency, $K = 1 + 0.5 \sum k_{23}^m / k_{31}^m$, and $T_1 = (k_{21} + \sum k_{23}^m)^{-1}$ is the total life time of level 2. From Eq. (4), it follows that the emission rate can not exceed $R_\infty = (2KT_{rad})^{-1}$ and that the unsaturated SM linewidth is $\Gamma_0 = 2 / T_2$. When $\Omega^2 T_1 T_2 K = 1$ the emission rate at resonance excitation ($\omega = \omega_0$) equals $R_\infty / 2$ and the linewidth is $\sqrt{2}\Gamma_0$. This is the so-called saturation regime. If $\vec{E} \parallel \vec{d}$ the corresponding electric field amplitude equals

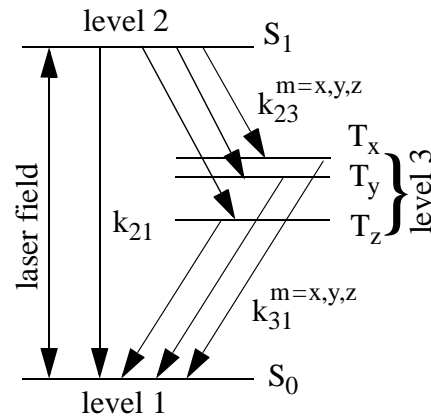


Fig. 5 The standard three-level model. S_0 and S_1 are the ground and the excited singlet states respectively. T_x , T_y , and T_z are three sublevels of the triplet state. The real splitting between these sublevels is much smaller and is important only for single spin experiments but not for the simple saturation effect.

$$E_{sat}^2 = \frac{\hbar^2}{d^2 K T_1 T_2}. \quad (5)$$

A two-level SM ($K = 1$) with the typical lifetime T_{rad} on the order of 10 ns has a maximum emission rate on the order of $5 \times 10^{-7} s^{-1}$. In experiments, such large values are observed very rarely. The main problem is associated with the triplet state. The radiative transition from the triplet state to the ground state is forbidden and, as a consequence, this state has a very slow decay. Due to the ISC, a molecule may be transferred from the excited singlet state to the triplet state. Such a molecule will not emit any photons and will not return to the ground singlet state until time $1 / k_{31}$ passes. This changes the maximum count rate and the saturation conditions dramatically. Usually $k_{23} \approx (10^6 - 10^8) s^{-1}$ [28], but very often k_{31} at low temperature is on the order of $(1 - 10^4) s^{-1}$ [28,29], and hence the coefficient $K \approx 10^2 - 10^5$. Molecules with $K < 10$ are considered to be good candidates for SMS, for which $R_\infty \approx 5 \times 10^6 s^{-1}$ is a realistic estimate. A photomultiplier count rate, R_{PM} , of $10^4 s^{-1}$ is expected taking into account the total (PM and the optics) photo detection efficiency of 2×10^{-3} .

In the literature there has been some confusion about the importance of the local field factor. The electric field amplitude in Equations 4-5 is the local electric field amplitude E_{loc} which would be observed in the position of the SM if it were removed. This electric field differs from the laser electric field E_{ext} outside of the crystal and from the internal macroscopic electric field E_{int} . The local field is proportional to the internal field in the matrix $E_{loc} = L E_{int}$ where L is the local field correction factor. In the Lorentz approximation [30] $L = (\epsilon + 2) / 3$, where ϵ is the relative dielectric constant of the matrix.

According to the Fresnel formulae for normal incidence [20], $E_{int} = 2 / (\sqrt{\epsilon} + 1) \cdot E_{ext}$ (note that $\mathfrak{R} = 4 / (\sqrt{\epsilon} + 1)^2$ is the reflection coefficient), thus

$$E_{loc} = 2L / (\epsilon^{1/2} + 1) \cdot E_{ext}. \quad (6)$$

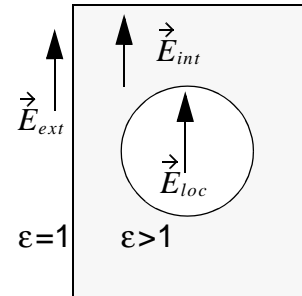


Fig. 6 External, internal (electric field averaged over a volume much smaller than λ^3 but much larger than the volume occupied by a single molecule), and local (actually acting on the molecule) fields.

Usually the average energy flux $I_{ext} = 0.5E_{ext}^2\sqrt{\varepsilon_0/\mu_0}$ is measured in an experiment, where ε_0 and μ_0 are the permittivity and permeability of vacuum [20]. From Equations (5) and (6) one gets the corresponding saturation intensity

$$I_{sat}^{(int)} = \frac{1}{L^2} \times \frac{\varepsilon_0 c \hbar^2}{2d_{vac}^2 T_1 T_2 K} \quad (7)$$

where d_{vac} is the value of the transition dipole moment when the molecule is in vacuum, and $c = 1/\sqrt{\varepsilon_0\mu_0}$ is the speed of light in vacuum. The total cross section at resonance conditions

$$\sigma_{tot} = \frac{h\nu\rho_{22}}{T_1 I_{ext}} = \frac{\omega(Ld_{vac})^2}{\hbar\varepsilon_0 c} T_2 = 4\pi^2 \frac{(Ld_{vac})^2}{h\varepsilon_0 \lambda} T_2 = \frac{3\lambda^2 A_{21}}{2\pi n \Gamma_0}, \quad (8)$$

where $n = \sqrt{\varepsilon}$ is the refraction index of the matrix. To derive the last equality in (8), the relations $A_{21} = \omega^3 n L^2 d_{vac}^2 / (3\pi\hbar\varepsilon_0 c^3)$ and $\Gamma_0 = 2/T_2$ have been used. The coefficient A_{21} is the radiative decay rate from the purely electronic excited state to the ground state. The saturation intensity can be now rewritten as

$$I_{sat}^{(int)} = \frac{2\pi\hbar\omega n}{3\lambda^2 A_{21} T_1 T_2 K} = \frac{\hbar\omega}{2\sigma_{tot} T_1 K}, \quad (9)$$

If there are radiative transitions from the purely electronic excited state to vibrationally excited states then $A_{21} = \Upsilon\Gamma_{rad}$, where $\Gamma_{rad} = 1/T_{rad}$ (cf. Eq. (2)).

$$\sigma_{tot} = \frac{3\lambda^2 T_2 \Upsilon}{4\pi n T_{rad}} = \frac{3\lambda^2 T_2 \Upsilon \eta}{2\pi n 2T_1} \quad (10)$$

The scattering cross-section can be expressed as a multiplication of σ_{tot} by the luminescence quantum yield $\eta = \Gamma_{rad}/\Gamma_\tau$, where $\Gamma_\tau = 1/T_1$.

$$\sigma_{scat} = \frac{13\lambda^2}{n 2\pi} \Upsilon \frac{\Gamma_{rad}^2}{\Gamma_0 \Gamma_\tau} \quad (11)$$

Besides a high emission rate, the SM should have high photo stability. Otherwise it can “disappear” before enough photo counts are accumulated. Photo instability is connected with the hole burning effect [31], which has many applications itself but limits the number of molecules suitable for SMS. Since a) it is difficult to design a detection system with an overall collection efficiency of greater than 1%, b) approximately 100 photo

counts are necessary for recording the line shape, and c) $\eta \approx 10\%$ — a molecule should be able to emit 10^5 photons before a bleaching occurs and thus the quantum yield of the photo transformation should be smaller than 10^{-5} .

Electron vibrational spectroscopy

The first measurements of the dispersed fluorescence from SMs excited at 0-0 transition frequency [32 -36] were done relatively soon after the publication of the excitation spectra of the 0-0 line. It took much longer for electron vibrational excitation spectra. The cross section of vibronic transitions is a few orders of magnitude smaller than the cross section of 0-0 lines. This makes electron-vibrational spectroscopy more difficult but not impossible. For example, the vibronic cross section of terrylene in naphthalene is 10^{-13} cm^2 or approximately 500 times smaller than that for purely electronic transitions. Nevertheless single molecule vibronic lines can be registered as shown in Fig. 7.

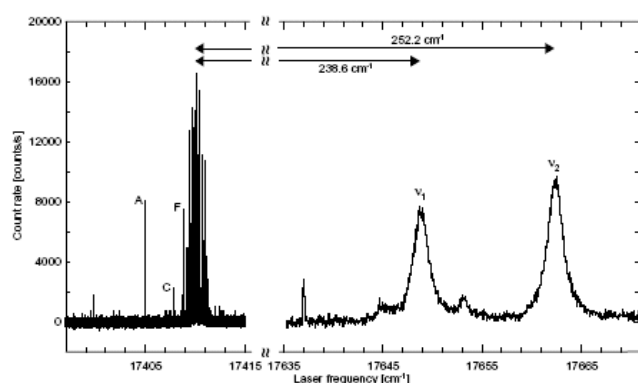


Fig. 7 Fluorescence excitation spectrum of terrylene in naphthalene. To the left, narrow lines due to the excitation of the purely electronic transition of individual molecules are visible. To the right, vibronic bands of two low frequency vibrations of terrylene appear. It was shown [37] that the weak signal at 17658 cm^{-1} corresponds to a vibronic transition of molecule A. The origin of the narrow line at 17642 cm^{-1} is unclear.

The investigation of vibrations of large organic molecules embedded in solids yields important information on the host-guest interaction and the local environments of probe molecules. Among others, questions about mechanisms and time scales of vibrational relaxation, the extent of vibrational energy inhomogeneity and its correlation with electronic transition energy inhomogeneity are of particular interest.

SM absorption and near-field excitation

Chronologically, in the first paper [10] it was the absorption of SMs that was detected rather than emission. Later, this technique was abandoned because the absorption is very

weak and can barely be seen on the large background of stray laser light. If the cross section of the laser beam is S , the relative change in the beam intensity I/I_0 can be estimated from the following simple formula

$$I/I_0 = 1 - \sigma_{tot} / S . \quad (12)$$

By inserting into this equation $\sigma_{tot} = 10^{-10} \text{ cm}^2$ and $S = 10^{-7} \text{ cm}^2$ one gets $I/I_0 = 0.999$. Since I_0 should not saturate the electronic transition and must be kept at a low level, the shot noise of the laser light may hide the absorption effect. It follows from Eq. (12) that achievement of a large relative absorption requires very small S . This can be realized in the so-called near field microscope.

The main idea of near field microscopy is that on the shadow side of an illuminated opaque screen with a small hole, the region with strong electromagnetic field is determined by the hole diameter rather than the light wavelength [38] and hence the theoretical limit for resolution of a classical optical microscope can be overcome. The first attempt to combine the high spatial resolution of the near-field and high spectral resolution of SMS at low temperatures was made in [39]. Here we briefly consider only one fundamental question connected with the direct measurement of SM absorption.

Under near-field excitation, the value S can be very small, even smaller than the SM absorption cross section. In this case Eq. (12) should be modified. This has been done in [40] where the absorption of a SM located in the waist of a Gaussian beam of a small radius a is described. The modified expression reads

$$\frac{I}{I_0} = \left(1 - \frac{\sigma_{tot}}{2\pi a^2}\right)^2 + \frac{1 - \Upsilon}{\Upsilon} \left(\frac{\sigma_{tot}}{2\pi a^2}\right)^2 . \quad (13)$$

The increase of the relative light intensity when the hole radius a is much smaller than the light wavelength λ can be easily understood. Such a hole works like an antenna which has dimensions smaller than the wavelength and hence very low efficiency. In the case of resonance the effective size of the emitting system is equal to the molecular cross section rather than the hole area and the intensity increase is observed.

If the molecule is placed near a perfectly conducting screen with a small circular hole, the light intensity in the far field region can be calculated from the solution of Maxwell's equations with appropriate boundary conditions. These calculations also show an increase

in the light intensity at subwavelength hole diameters but when the hole becomes too small, the SM emission is suppressed by the mirror surface currents on the screen. The main conditions for detecting SM absorption are large absorption cross section, high photo stability, and $K \approx 1$. These conditions are identical to the ones for luminescence detection. On the other hand if a SM has only unshifted 0-0 emission it can not be detected using luminescence excitation techniques but would be the best candidate for an absorption experiment.

Single-spin Rabi oscillations

Although magnetic resonance is not a subject of this work, a briefly review is appropriate because it shows how sensitive to fluctuations single molecules can be.

Magnetic resonance for SMs was first observed independently by two groups who showed that the fluorescence emission rate for pentacene (Pc) in p-terphenyl (p-TP) could be decreased by applying microwave (MW) pulses that coupled the hyperfine triplet levels [41, 42]. The reason for the decrease is easy to understand. Due to the ISC, the molecules primarily decay into the T_x and T_y sublevels (Fig. 5), which also have the fastest decay rates. By transferring them to the longer lived T_z state with resonant MW radiation, they spend a longer time in the triplet manifold and hence the fluorescence rate is reduced. For $T_x - T_z$ and $T_y - T_z$ resonant MWs, a 25% and 15% reduction in the fluorescence were observed, respectively [42]. The $T_x - T_y$ resonance was missing, implying that the lifetimes of the T_x and T_y states are similar. The kinetics of this process have since been analyzed in detail [43].

Significant broadening of the MW resonance lines compared to those measured from electron spin echo experiments was explained by spectral diffusion due to the second order hyperfine interaction between the triplet spin and the 14 proton spins in the Pc molecule that can flip when the molecule is in the singlet manifold. This hypothesis was later corroborated [44] when broadening from ^{13}C substituted Pc molecules was shown to be larger because the nonzero ^{13}C nuclear spin contributes. The linewidth could be reduced by a factor of 40 by using deuterated Pc [45]. Deuterium has only 15% the nuclear magnetic moment of protons, and the huge line narrowing results because the hyperfine interaction is a second order effect in zero magnetic field.

These experiments enabled the single spin coherence experiments that followed [46, 47]. In [46], oscillations of the fluorescence level as a function of the length of applied MW pulses were measured. The fluorescence intensity oscillates synchronously with oscillation in the population of the T_x and T_z levels depending on the pulse length. A decay in the oscillations was also observed, showing dephasing from nuclear spin flip-flops occurred in p-TP molecules. Magnetic resonance coherence has also been demonstrated with electron spin echo experiments [47], where “ $\pi/2 - \pi - \pi/2$ ” pulse trains were used to measure triplet state coherence for Pc in p-TP. A dispersion of a factor of three was observed for the spin dephasing time, which might come from crystal defects in the vicinity of some molecules, although the estimated necessary average distortion (about 10% of the lattice constant) seems too large.

Model for Molecule's Environment

Even in the case of a single probe molecule in a crystal, the environment of that molecule has a very complex structure because the perfect crystal periodicity is distorted by the impurity or by uncorrelated nuclear spins. The situation is still more complex if the probe molecule is embedded in a polymer or a glass where a detailed description even for a pure host matrix is not available.

Some simplification comes from low temperatures. The complex multidimensional potential energy surface of the multi particle system can be reduced to several local potential minima. Those minima are separated by high barriers and can be in the first approximation treated independently. Many states can exist in such wells but again, recollecting that we are dealing with the low temperature limit, it is enough to take into account only the *two lowest states* in each local well. The dynamics is then governed by the interaction between these localized states and long-wavelength thermally-activated acoustic phonons, phonons which are not very sensitive to the microscopic structure of the elastic media. The interaction causes transitions between the two states assisted by emission or absorption of phonons and thus the states become pseudo localized. Successive excitations and relaxations of the pseudo localized states create fluctuating electrical (elastic) fields which affect the probe molecule. The concept of *two-level systems* (TLSs) interacting with acoustic phonons and with probe molecules is the corner stone of theoretical models considered in

this *Habilitationsschrift*. Probably, the most direct evidence of the TLS existence can be found by measuring an phonon-echo effect [48, 49] which is a counterpart of the well known nuclear spin echo effect in NMR and photon-echo effect [50, 51].

From the model described above, it is clear that the properties of different solids at low temperatures vary according to the variations of TLS parameters because properties of acoustic phonons are essentially universal and can be satisfactorily described by the Debye model. It was found empirically that in amorphous solids (glasses and polymers) the TLS parameters should have extremely broad distributions. A standard distribution function which is usually used in calculation is given below

$$P(E, K) = \frac{P_0}{K\sqrt{1 - K / K_{max}(E, T)}}, \quad (14)$$

where E is the energy difference between the two states, and K is the relaxation rate of the excited state which spans a range from nanoseconds to months.

To explain such broad distributions, a tunneling mechanism was suggested [52, 53, 54, 55]. A tunneling process between two minima (from state $|1\rangle$ to state $|1'\rangle$ in Fig. 8) depends exponentially on the height and width of the potential barrier and thus small variations of these two parameters cause a large variation in the transition rate. During a transition from a higher to lower energy state a phonon is emitted with a frequency corresponding to the energy difference between the two states. Of course, in the presence of thermal phonons with frequencies such that $h\nu = E$ an excitation from $|1\rangle$ to $|1'\rangle$ can take place too.

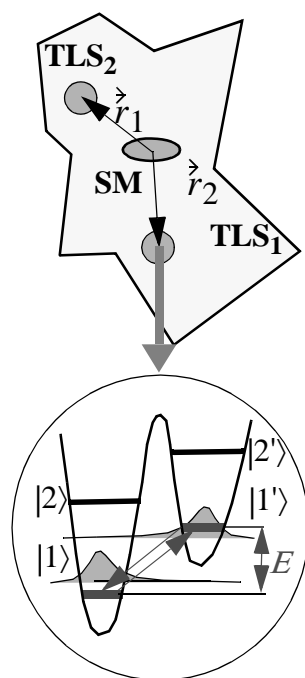


Fig. 8 A pictorial presentation of the model. The environment consists of a set of two-level systems (TLSs) interacting with the probe molecules (SM). The two lowest states of the TLSs are states of a particle in a single well or a double-well potentials. In the latter case the transition between these states is governed by the tunneling under the barrier process.

When a TLS jumps back and forth between the two states this creates fluctuating fields. These fields interact with the probe molecule and the molecular wave function

starts to fluctuate and so does the transition frequency and other molecular parameters. As a consequence, the spectrum of the probe molecule changes. Spectral lines broaden and their shapes become complex and time dependent. These variations of the spectrum are called spectral diffusion (SD) [56].

The TLS relaxation rate calculated in the approximation of one-phonon emission is

$$K = W \cdot \left(\frac{T}{E}\right)^2 \cdot E^3 \cdot \coth\left(\frac{E}{2k_{\text{B}}T}\right), \quad (15)$$

where $(T/E)^2$ emphasizes that the TLS transition dipole moment is proportional to the square of the tunneling matrix element T and inversely proportional to the square of the TLS energy [52]. This equation is analogous to that for the emission rate of a one-photon allowed optical transition.

If the double well potential asymmetry is A , the TLS energy

$$E = \sqrt{A^2 + T^2} \quad (16)$$

For a given energy, the maximum relaxation rate is given by

$$K_{\text{max}} = W \cdot E^3 \cdot \coth\left(\frac{E}{2k_{\text{B}}T}\right), \quad (17)$$

Eqs. (14) and (17) are usually referred to as a **standard TLS model** for amorphous solids. For polymers $W \cdot k_{\text{B}} \approx 10^{10} \text{ Hz K}^{-3}$ [57, 58]. Because W is very large, for many TLSs $K \ll K_{\text{max}}$ and the TLS distribution function can be written approximately as

$$P(E, K) = \frac{P_0}{K}. \quad (18)$$

Less is known about interactions between the TLSs and the probe molecule. Most often, this interaction is described as a dipole-dipole interactions. Usually it is assumed that the difference of the TLS dipole moments in the two states is proportional to the double well potential asymmetry A and inversely proportional to the TLS energy [59].

$$D \propto \frac{A}{E} = \frac{\sqrt{E^2 - T^2}}{E} = \sqrt{1 - \left(\frac{T}{E}\right)^2}. \quad (19)$$

Eqs. (17, 15) allows us to write Eq. (19) in the form

$$D \propto \sqrt{1 - K/K_{max}}. \quad (20)$$

Except for TLSs with $K \approx K_{max}$, D is approximately constant.

The presence of a large number of states localized in such double well potentials explains many observations (see [60] and references therein). It is really amazing that such a simple model can describe a variety of optical phenomena and thermodynamical properties.

Another source for matrix dynamics is the transition between states $|1\rangle$ and $|2\rangle$ ($|1'\rangle$ and $|2'\rangle$). Such transitions do not involve tunneling and usually have relatively narrow distributions of relaxation rates.

An example of SD is shown in Fig. 9. In the experiment the laser frequency was scanned repeatedly over the SM resonance line with a frequency step of 4 MHz and a period of 2.56 s/scan for more than an hour. For each scan, the resonance line was fit to a Lorentzian function. The line position obtained is plotted against the measuring time in the Figure 9. The spectral line occupies six spectral positions; whereas interaction with several TLSs should lead to the number of states which is a power of two. This example demon-

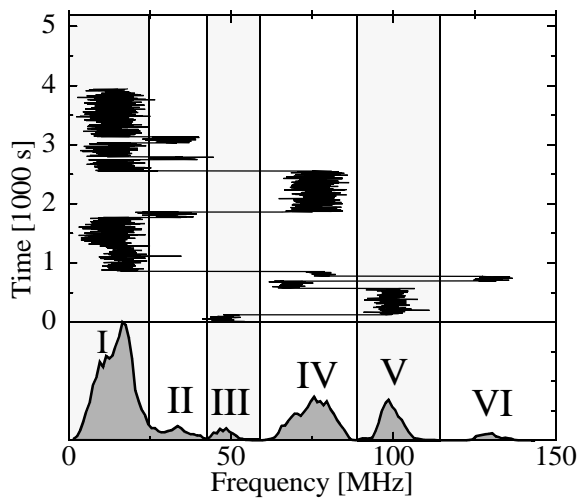


Fig. 9 The frequency trajectories for a single terrylene molecule in n-hexadecane undergoing light-induced spectral diffusion. The shaded vertical bars indicate the frequency ranges used to differentiate the six sites. Along the bottom of the trajectories, the frequency-position histograms are shown.

strates that general arguments suggesting that at low temperatures every system can be considered as a TLS should be taken with a precaution especially when the system is affected by strong external fields.

Principles of Data Analysis

In this section we discuss the principles of the interpretation of rare events. When observing single molecules, there are times when some molecules appear to exhibit peculiar behavior. This is a good reason for studying single molecules, since such behavior may not be observable with ensemble techniques. The analysis of such behavior may someday shed light on the microscopic structure of the molecules themselves and their local environments, but may also be misleading.

Single molecules sometimes exhibit unusual (non classical) behavior, which is relatively easy to document for cases when all molecules behave the same way, as with photon antibunching, for example, but such examples are an exception. More typically, each SM data set is irreproducible owing to either the SM's unique local environment or to the fundamental probabilistic nature of the microscopic world, and extra effort is required to extract useful information from the data.

Examples of complex SM behavior have been documented by Boiron et al. [61], for example. In their study they check the consistency of the spectral trails of single molecules (similar to that shown in Fig. 9) with the tunneling two-level system model. It is actually a minor point in their paper when they mention that one of the ~ 70 molecules studied jumped 45 times between three states A , B , and C always in the direction $A \rightarrow B \rightarrow C \rightarrow A$ like an "engine," but this is a very good example for our discussion here. If the molecule had an equal probability to jump to either of the two unoccupied states, the probability of observing such a sequence would be $(1/2)^{45}$, or 10^{-14} . This behavior appeals for an explanation because it is simple.

A fundamental principle of the data analysis is that the quality of an explanation can only be judged in relation to others. Probability theory can be used for formalizing such a judgment. These techniques are described in detail by Sivia in his chapter titled "model selection" [62]. Here we adopt those general arguments to the above engine molecule example.

Say there are two models for describing the spectral trail. Model A says that the jump ordering is random. Model B asserts that the order is not always random, but for a certain range of values for a parameter λ , the jump order can show regular behavior. It is an over-

simplification to specify the jump sequence by a single parameter, but nevertheless we proceed to do so to keep the discussion simple. An important ingredient of model B is an estimate for the probability density functions (PDF) of possible values for λ deduced either from the model or based on previous experience. This estimate must be made *before* the analysis of the data. To simplify the discussion, we take this PDF as constant between λ_{min} and λ_{max} , and zero otherwise. The relative merit of the two models may be written as the ratio of the probabilities of the models proving to be correct after data analysis:

$$\frac{P(A|D, I)}{P(B|D, I)} \approx \frac{P(A|I)}{P(B|I)} \times \frac{P(D|A, I)}{P(D|B, \lambda_0, I)} \times \frac{\lambda_{max} - \lambda_{min}}{\delta\lambda} \quad , \quad (21)$$

where $P(X|Y)$ is a conditional probability of X given Y , and I stands for prior information. The first fraction on the right hand side is the ratio of the prior PDFs for the two competing models -- a measure of the relative faith one has in the two models before the analysis of the data at hand. If both hypotheses are viewed with equal merit then this term can be set equal to one. The second term is the ratio of the likelihood functions for the two models (probabilities of observing a specific set of data given the truth of the corresponding hypothesis), where λ_0 is the best estimate of the fit parameter λ . Since λ_0 is found by a fit to the data, the ratio of the likelihood functions is automatically less than one. It can be as small as 10^{-14} in this case. The cost for having the extra parameter in the theory is contained in the third term, which is the most crucial term for our discussion. This term is sometimes called the Ockham factor. Without this factor more sophisticated explanations would always be preferred over simpler ones. The denominator $\delta\lambda$ is the width of the likelihood function $P(D|B, \lambda, I)$. The sticking point here is that enough ambiguity has to be placed in the prior PDF for λ to guarantee that it can describe the character of all observed molecules and not only the one showing engine-like behavior. This can dramatically increase the posterior ratio in Eq. (21). If someone suggests a model for the molecular engine by assuming very special microscopic surroundings for that molecule he or she should explain why the probability for creating such structure in the process of sample preparation is larger than 10^{-14} .

If the range for λ is determined from the measurements, then an estimate of the posterior ratio in Eq. (21) can only be obtained with a new set of data not available before. If these crucial quantities — the widths of the parameter distribution functions — are esti-

mated based on experimental results, the experimental results become an essential part of the theory and can not be considered as an argument supporting the theoretical model. This is where reproducibility comes in. If the probability for observing a certain type of SM behavior is not fundamentally limited (by rare decay channels, for example), the need for repeated measurements suggests that the macroscopic conditions (sample preparation, external fields, etc.) should be specified in a way to insure a certain level of reproducibility. A criterion commonly accepted for ensemble measurements of 5% or higher can also be applied to single-molecule data.

Just because a certain type of behavior is improbable does not mean that it is insignificant, but precise probabilistic methods for the interpretation and characterization of the rare events should be applied. Meyer points out in his book on statistics [63] that if Lord Rutherford's students had disregarded the small fraction of scatterings that occurred at very large angles when they bombarded a gold foil with α particles, they would not have discovered the nucleus.

PDFs are not calculated for data and theories presented in this manuscript. But in most cases the reader can at least qualitatively see how such calculations can be done. And it is an interesting and instructive exercise to think about PDFs and parameter distributions every time single molecule data are addressed.

III. Intensity-Time-Frequency Correlation Spectroscopy

A common characteristic feature of single molecules (SM), single quantum dots, or any other single quantum systems is that each successive spectral measurement performed on the same SM can reveal a new “spectrum” even when the macroscopic conditions do not change [64, 65]. Of course time and frequency obey the uncertainty principle and one can speak about time-dependent “spectra” only when the measuring procedure is exactly described. There are a few methods for measuring time-dependent spectra of ensembles (two- and three-pulse photon echo, “hole burning” etc.). To simplify the discussion, let us assume that a spectrum is measured with a spectrometer having a shutter in front of its entrance. The shutter is opened for a time τ and a spectrum of the incoming light is measured. If the system consists of billions of molecules and is in thermodynamic equilibrium, the “spectrum” obtained will be a function of τ only. If we repeat the measurement, the same result will be obtained because for a large system in most cases the fluctuations can be neglected. But the situation is dramatically different if only one molecule is studied. The micro environment of every single molecule strongly influences the observed spectrum in a unique and time-dependent way. This makes the results “non reproducible”. In addition, data are obscured by the fluctuations of the number of photons emitted in the time interval τ . In general, the better the time resolution that is needed, the bigger are the overall fluctuations, and conventionally one has to trade one for the other. A new approach called intensity-time-frequency correlation (ITFC) spectroscopy [66, 67] allows one to preserve high time resolution without sacrificing the signal-to-noise ratio.

ITFC spectroscopy works in three steps: a) N laser scans over the same spectral region are acquired and the SM luminescence intensity as a function of the laser frequency is measured, b) a correlation function is calculated for each scan, and c) these functions are averaged. Mathematically this can be written in the following way:

$$S_{ITFC}(\omega', \delta_t) \equiv \lim_{N \rightarrow \infty} \frac{1}{N} \sum_{k=1}^N \int_{\omega_0} I_k(\omega) I_k^{\delta_t}(\omega + \omega') d\omega, \quad (22)$$

where $I_k(\omega)$ is the k -th single scan and $I_k^{\delta_t}(\omega)$ is the scan starting with a time delay δ_t with respect to the moment when $I_k(\omega)$ is completed. The laser frequency $\omega(t) = rt$, where r is the frequency scan rate and t is the time measured from the beginning of the corresponding scan. The upper integration limit ω_0 is the spectral scan length and hence $\omega_0 r^{-1}$ is the time needed for a single scan. $\delta_t = 0$ corresponds to an auto correlation, otherwise $\delta_t \geq \omega_0 r^{-1}$. The idea of the ITFC method is based on the fact that a correlation function between two scans is sensitive only to dynamics on the time scale on the order of or shorter than the time delay between the two scans. A conventional photon correlation technique where the laser frequency is fixed [68, 69] allows one to gain insight into fast SM dynamics but does not provide spectral information.

If the single-molecule resonance frequency, a parameter in optical Bloch equations, is considered as a stationary stochastic function of time $\vartheta(t)$, the linearized approximation for $S_{ITFC}(\omega', t_w)$ can be written in the following way [67]

$$S_{ITFC}(\omega', t_w) \sim \text{Re} \left(\int_0^{\infty} e^{-i\omega'\tau} \frac{e^{-\tau/T_1}}{1 + (T_1 r \tau)^2} \left\langle \exp \left[i \int_{\omega' r^{-1} + \delta_t + \tau}^{\omega' r^{-1} + \delta_t + 2\tau} \vartheta(u) du - i \int_0^{\tau} \vartheta(u) du \right] \right\rangle d\tau \right), \quad (23)$$

where T_1 is the lifetime of the SM excited state and $t_w = \omega' r^{-1} + \delta_t$. This equation is valid for $t_w \gg T_1$. The value of t_w determines the time resolution of the ITFC spectra. If $T_1^2 r \ll 1$ and $\omega' \ll \delta_t r$, $S_{ITFC}(\omega', t_w)$ is identical to the expression for a spectral hole or a Fourier transform of an echo amplitude measured in a “gedanken” hole burning or three-pulse photon echo experiment done on a sample which consists of many probe molecules [70] but in statistically identical microscopic environments.

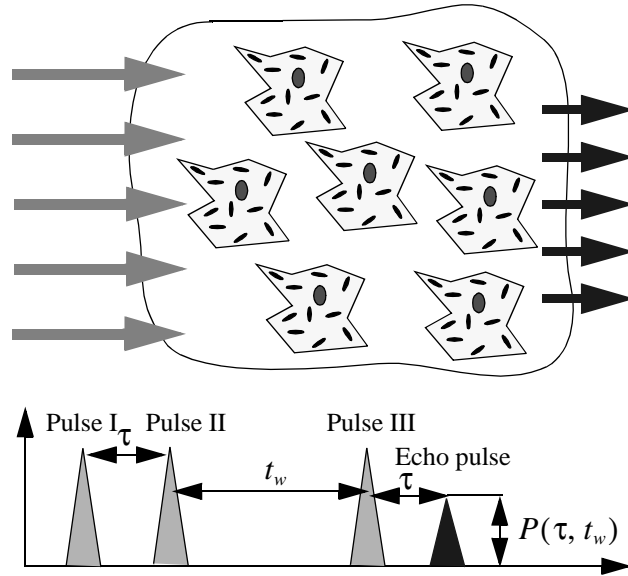


Fig. 10 A “gedanken” three-pulse photon echo experiment. The sample consists of molecules (shown as large ellipses) having statistically identical microscopic environments i.e interacting with identical sets of TLSs (black bars). Flips of neither of two TLSs are correlated. The echo amplitude is a function of the two time delays τ , t_w , and parameters of all TLSs.

strates a fundamental connection between single-molecule data and ensemble measurements.

The advantage of ITFC with respect to ordinary spectroscopy is displayed in two-photon excitation spectra of diphenyloctatetraene (DPOT) molecules embedded in n-tetradecane. When the first spectra of single DPOT molecules were measured at 1.8 K [12], a significant and unexpected difference between the observed linewidth and the lifetime-limited linewidth was noted. Such a difference could be explained by temperature effects owing to the nonzero bath temperature or because of local heating by laser illumination. These two explanations did not pass experimental tests. The difference was independent of laser power and the lifetime-limited linewidth was close to the linewidth measured at the same

bath temperature under one-photon excitation. The problem has been solved by applying the ITFC technique [66]. Two-photon excitation lines were narrowed by a factor of two in ITFC spectra when they were measured with a time resolution better than 50 ms (see Fig. 11), a time resolution which was not possible to achieve otherwise. In the ITFC spectra the time resolution was defined by the time needed to scan a spectral region which covers a single-molecule line. Thus in this case a light-induced spectral diffusion (LISD) was observed. At present only a phenomenological description is available for this effect. At the wavelength of the exciting light (888 nm) there is a weak absorption of the CH-band (3rd overtone) of tetradecane. The absorbed energy dissipates into the matrix and leads to some rearrangements of the local environment of the probe molecules and thus to a change in

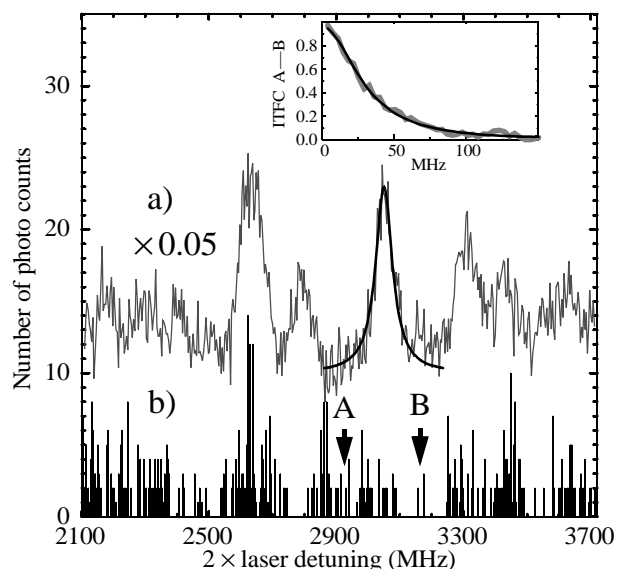


Fig. 11 (a) A two-photon excitation spectrum recorded by averaging 200 single scans recorded with frequency steps of 3.6 MHz and 5 ms accumulation time at each frequency position. The spectrum has a time resolution ~ 500 s. (b) Example of a single scan. The SM line at 3030 MHz has a count rate of about 1.3 counts/trace at the maximum. In spectrum (a) the line has a width of 62 MHz (the thick grey line is a Lorentzian fit). The inset shows the average over 200 single scan auto correlation functions, calculated for the spectral region between arrows A and B. The decay of the ITFC corresponds to a linewidth of 28 MHz (a Lorentzian fit is shown).

their transition frequencies. This change (repeated many times) causes an apparent line broadening. When measured conventionally with lower laser power, the spectra become too noisy and need long accumulation times (on average approximately only ten photo counts at the absorption peak of a single molecule are detected in a time interval of 50 ms). A longer accumulation time increases diffusional broadening. Note that the excitation rate is proportional to the square of the laser intensity while the LISD is proportional to the first power of the laser intensity. To keep the signal-to-noise ratio at a constant value with two times lower laser power one would need a four times longer accumulation time.

Details

It is difficult to produce a mathematically correct definition for a single molecule spectrum in a fluctuating environment. For example, an approach based on the fluctuation dissipation theorem [71] has often been used, though neither an ensemble nor time averaging can be realized with a single molecule. To get around this problem, a “cut-off” approximation (COA) was used [72-80], but without much discussion of its validity. We first analyze the accuracy of the COA and then describe a way out of the difficulties associated with this approximation by using the Intensity-Time-Frequency-Correlation technique.

Linearized Bloch equations and “cut-off” approximation

As it was explained in the Introduction, the environment is described by a set of TLSs interacting with a single molecule and with acoustic phonons. Each TLS is characterized by the energy difference between the two states, by the relaxation rate, and by the coupling strength of the SM-TLS interaction, which is assumed to be dipole-dipole in nature. Intrinsically, the ensemble of TLSs is characterized by a distribution of the first two parameters and a special kind of this distributions is assumed in the standard TLS model. Because of interactions with phonons, each TLS flips between its two states and these flips cause changes of the single molecule resonance frequency.

At low laser powers we can neglect the triplet state (see Fig. 5) and can treat a SM as a two-level atom, whose behavior is described by a 2×2 density matrix ρ . The probability for the atom to emit a spontaneous photon at a time t is then proportional to the density

matrix element $\rho_{22}(t)$. The time evolution of the density matrix is described by the optical Bloch equations.

$$\dot{\tilde{\rho}}_{12} = (i\omega(t) - i\vartheta(t) - \gamma)\tilde{\rho}_{12} + \frac{i}{2}\Omega(\rho_{22} - \rho_{11}) \quad (24)$$

$$\dot{\rho}_{22} = -2\gamma\rho_{22} + \frac{i}{2}\Omega(\tilde{\rho}_{12} - \tilde{\rho}_{21}), \quad (25)$$

where the SM transition frequency $\vartheta(t)$ is an arbitrary stationary stochastic function of time, $\omega(t)$ is the time dependent laser frequency, $\tilde{\rho}_{12} = \rho_{12} \cdot \exp[-i\int_0^t \omega(\tau)d\tau]$, Ω is the Rabi frequency which is proportional to the amplitude of the laser light, and $2\gamma = 1/T_1$ is the decay rate of the excited state. The particular form of $\vartheta(t)$ assumed in the TLS model is not essential for most of the following discussion. For simplicity and brevity, we assume that the laser frequency is scanned with a uniform speed $\omega(t) = \omega_{min} + rt$, where the initial frequency ω_{min} is zero.

At low laser power $\rho_{11} \approx 1$, $\rho_{22} \approx 0$ and hence Eq. (24) reads

$$\dot{\tilde{\rho}}_{12} = (i\omega(t) - i\vartheta(t) - \gamma)\tilde{\rho}_{12} - \frac{i}{2}\Omega. \quad (26)$$

The solution of linear Eqs. (25, 26) is straightforward.

$$\rho_{22}(t) = -\Omega \int_0^t e^{-2\gamma(t-v)} \text{Im}[\tilde{\rho}_{12}(v)] dv \quad (27)$$

and

$$\tilde{\rho}_{12}(t) = -i\frac{\Omega}{2} \cdot \left[\int_0^t e^{-\gamma t''} \exp\left(i \int_{t-t''}^t (\omega(u) - \vartheta(u)) du \right) dt'' \right] \quad (28)$$

where the initial conditions are $\rho_{12}(0) = \rho_{22}(0) = 0$. Substituting expression (28) in (27), $\rho_{22}(t)$ can be written in the following form:

$$\rho_{22}(t) = \frac{\Omega^2}{2} \text{Re} \left(\int_0^t e^{-2\gamma(t-v)} \int_0^v e^{-\gamma t''} \exp\left(i \int_{v-t''}^v (\omega(u) - \vartheta(u)) du \right) dt'' v \right)$$

$$= \frac{\Omega^2}{2} \operatorname{Re} \left(\int_0^t e^{-2\gamma t'} \int_0^{t-t'} e^{-\gamma t''} \exp \left(i \int_{t-t'-t''}^{t-t'} (\omega(u) - \vartheta(u)) du \right) dt'' dt' \right), \quad (29)$$

where the substitution $t - \nu = t'$ is used.

The integrals over dt'' and dt' are essentially different from zero when $t' \leq (2\gamma)^{-1}$ and $t'' \leq \gamma^{-1}$ or, if these conditions are expressed in a different way, when $rt't'' \leq 2^{-1}r/\gamma^2$ and $rt''^2 \leq r/\gamma^2$. If additionally $r/\gamma^2 \ll 1$ (slow scan approximation) then $\int_{t-t'-t''}^{t-t'} \omega(u) du = rtt'' - rt't'' - rt''^2 / 2 \approx rtt'' = \omega t''$. If only long time behavior ($\gamma t \gg 1$) of $\rho_{22}(t)$ is of interest than the upper limits in the two integrals can be set to an infinity and finally

$$\rho_{22}(t) = \frac{\Omega^2}{2} \operatorname{Re} \left\{ \int_0^\infty e^{-2\gamma t'} \int_0^\infty e^{-\gamma t''} e^{-i\omega t''} \exp \left(i \int_{t-t'-t''}^{t-t'} \vartheta(u) du \right) dt'' dt' \right\} \quad (30)$$

The stationary optical line shape $R(\omega)$ can be defined as follows:

$$R(\omega) \propto \frac{1}{t_m} \int_0^{t_m} \rho_{22}(t) |_{\omega=\text{const}} dt, \quad (31)$$

Ideally the measuring time t_m should be much longer than the longest correlation time of the system. In this case $R(\omega)$ is independent of the measuring time and

$$\begin{aligned} R(\omega) &\propto \operatorname{Re} \left\{ \int_0^\infty e^{-2\gamma t'} \int_0^\infty e^{-\gamma t''} e^{-i\omega t''} \left\langle \exp \left(i \int_0^{t''} \vartheta(u) du \right) \right\rangle dt'' dt' \right\} \\ &\propto \operatorname{Re} \left\{ \int_0^\infty e^{-\gamma t''} e^{-i\omega t''} \left\langle \exp \left(i \int_0^{t''} \vartheta(u) du \right) \right\rangle dt'' \right\}, \end{aligned} \quad (32)$$

where an average over all possible trajectories (denoted by $\langle \rangle$) replaces the time average. For a stationary stochastic function $\vartheta(u)$ this average depends only on the length of the integration interval over du . This interval is equal to $t - t' - (t - t' - t'') = t''$.

For the relaxation time distribution assumed in the standard TLS model, such t_m is equal to infinity and the stationary spectrum can not be measured in a finite time experiment.

In the cut-off approximation, all TLSs having a relaxation rate slower than the inverse of a measuring time t_m are neglected, and the measuring time for the remaining TLSs is set to infinity.

Fig. 12 illustrates an emerging problem. Direct numerical simulations based on the linearized optical Bloch equations (see Eqs. (30) and (31)) show that many SM lines are subject to significant fluctuations and it is difficult to assign a line shape to a single molecule in these real scan simulations (RSS) while in the COA each molecule has a well defined spectral line shape (also shown in Fig.12). This is because during measurements performed over a finite time, some neglected TLSs actually jump while some relative-

ly fast TLSs do not have enough time for a number of jumps which can be counted as infinite. TLSs which are not taken into account properly by the COA are approximately those with the relaxation rate between $0.1 / t_m$ and $10 / t_m$.

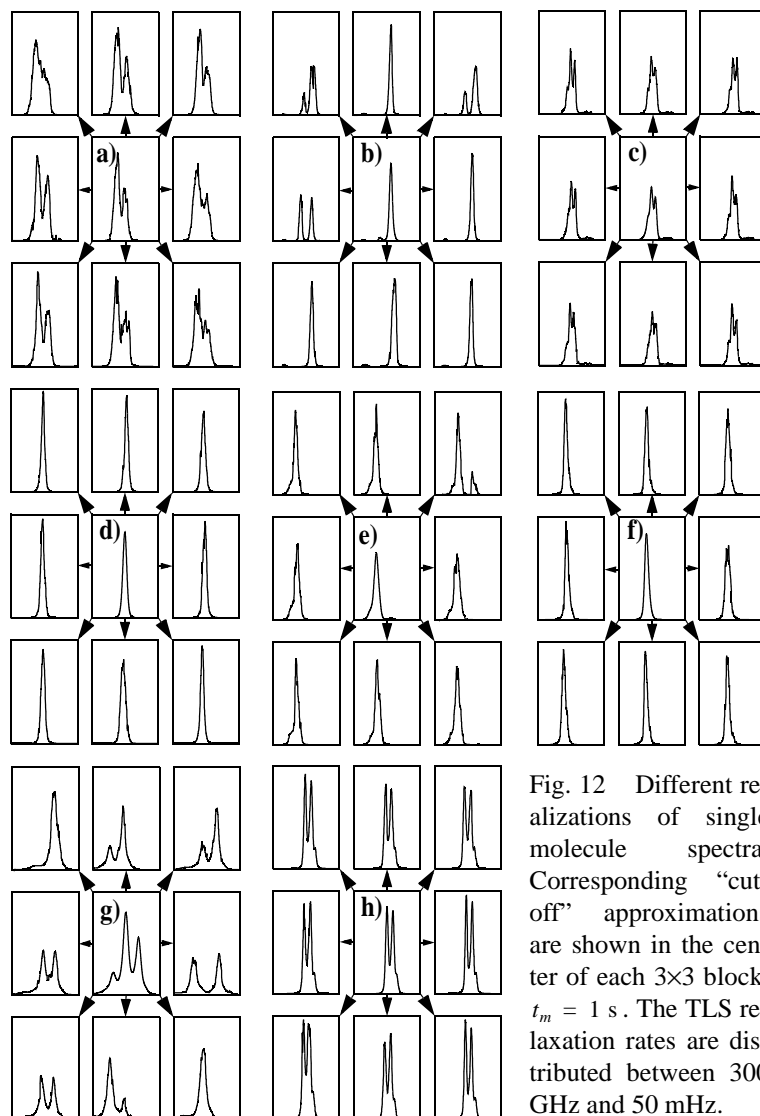


Fig. 12 Different realizations of single molecule spectra. Corresponding “cut-off” approximations are shown in the center of each 3×3 block. $t_m = 1$ s. The TLS relaxation rates are distributed between 300 GHz and 50 mHz.

Theory of the ITFC spectroscopy

The principles of ITFC spectroscopy were explained in the overview. Emission from the electronically excited state provides the signal and Eq. (22) can be written as

$$S_{ITFC}(\omega', \delta_t) \sim \left\langle \int_{-\infty}^{\infty} \rho_{22}(t) \rho_{22}^{\delta_t}(t + \theta) dt \right\rangle, \quad (33)$$

where $\theta = \omega' r^{-1}$. $\langle \rangle$ in Eq. (33) means an average over all possible realizations of the stochastic function $\vartheta(t)$. If $\delta_t \neq 0$, then $\rho_{12}^{\delta_t}(0) = \rho_{22}^{\delta_t}(0) = 0$. If $\delta_t = 0$, we should take into account that when emitting a photon at time t , the SM jumps to the ground state and hence $\rho_{12}^{\delta_t}(t) = \rho_{22}^{\delta_t}(t) = 0$. A general expression for $\rho_{22}^{\delta_t}(t + \theta)$ follows from Eq. (29)

$$\rho_{22}^{\delta_t}(t + \theta) = 2\Omega^2 \operatorname{Re} \left(\int_0^{\chi} e^{-2\gamma\tau'} \int_0^{\chi - \tau'} e^{-\gamma\tau''} \exp \left(i \int_{-\tau' - \tau''}^{-\tau'} (\omega(t + \theta + u) - \vartheta(t + \theta + u + \delta_t)) du \right) d\tau'' d\tau' \right), \quad (34)$$

where $\chi = t + \theta$ if $\delta_t \neq 0$ and otherwise $\chi = \theta$.

Each of the scans starts far from the resonance and takes a time much longer than T_1 . This means that $\rho_{22}(t)$ is different from zero only when $\gamma t \gg 1$ and hence, because of $\exp(-2\gamma t')$ and $\exp(-\gamma t'')$ factors in the integrated function in Eq. (29), the upper limits of the integrals over dt' , dt'' can be set to infinity. If $\delta_t \neq 0$, this can be done also in Eq. (34) for integrals over $d\tau'$ and $d\tau''$. If $\delta_t = 0$, the approximation is valid only if $\gamma\theta \gg 1$. When $\gamma\theta < 1$, a dip of width $\omega_d' < r/\gamma$ in the frequency domain corresponds to the well-known photon antibunching effect (see Introduction). For simplicity, this effect is not considered here and all limits are assumed to be ∞ .

From Eqs. (29) and (34) it follows that

$$\int_{-\infty}^{\infty} \langle \rho_{22}(t) \rho_{22}^{\delta_t}(t + \theta) \rangle dt = 2\Omega^4 (\operatorname{Re}(A^-) + \operatorname{Re}(A^+)), \quad (35)$$

where substituting $\omega = rt$, A^{\pm} reads:

$$A^{\pm} = \int_{-\infty}^{\infty} \int_0^{\infty} \int_0^{\infty} \int_0^{\infty} e^{-2\gamma(t' + \tau')} e^{-\gamma(t'' + \tau'')} e^{i r t (t' \pm \tau')} e^{i \lambda^{\pm} r} \left\langle \exp \left(-i \int_{-t' - \tau''}^{-t'} \vartheta(t + u) du \mp i \int_{-\tau' - \tau''}^{-\tau'} \vartheta(t + \theta + u + \delta_t) du \right) \right\rangle dV \quad (36)$$

here $\lambda^{\pm} = -t't'' \mp \tau'\tau'' \pm \theta\tau'' - (t'^2 \pm \tau''^2) / 2$ and dV stands for $dt'' dt' d\tau' d\tau'' dt$. Since $\vartheta(t')$ is a function whose average is independent of a time shift t , integration over dt gives a δ -function $\delta(r(t'' \pm \tau''))$. Because $t'', \tau'' > 0$, $A^+ = 0$. Further, since t', τ' are on the order of $\gamma^{-1} \ll \theta + \delta_t$, the average over all possible trajectories in Eq. (36) depends very

little on the time shifts t' and τ' . If this dependence is neglected, the integration over dt'' , dt' , and $d\tau'$ is straightforward and leads to the following expressions for $S_{ITFC}(\omega', \delta_t)$:

$$S_{ITFC}(\omega', \delta_t) \sim \frac{\Omega^4}{4\pi r \gamma^2} \operatorname{Re} \left(\int_0^\infty e^{-i\omega' \tau''} \frac{e^{-2\gamma \tau''}}{1 + (T_1 r \tau'')^2} \left\langle \exp \left(-i \int_0^{\tau''} \vartheta(u) du + i \int_{\theta + \delta_t + \tau''}^{\theta + \delta_t + 2\tau''} \vartheta(u) du \right) \right\rangle d\tau'' \right) \quad (37)$$

or

$$S_{ITFC}(\omega', \delta_t) \sim \operatorname{Re} \left(\int_0^\infty \frac{e^{-i\omega' \tau}}{1 + (T_1 r \tau)^2} P(\tau, t_w) d\tau \right), \quad (38)$$

where $t_w = \theta + \delta_t = \omega' r^{-1} + \delta_t$, $2\gamma = 1/T_1$, and $P(\tau, t_w)$ is the three-pulse photon echo amplitude [56] measured in the ‘‘gedanken’’ experiment shown in Fig. 10. If $T_1^2 r \ll 1$ (slow scan) and $\delta_t \gg \omega' r^{-1}$ (unless $\delta_t = 0$, $\delta_t \geq \omega_0 r^{-1} \gg \omega' r^{-1}$), $S_{ITFC}(\omega', \delta_t)$ is simply a Fourier transform of $P(\tau, \delta_t)$.

Starting with a paper by Klauder and Anderson [56], averages like that in Eq. (23) have been calculated many times for ensembles of two-level atoms (spins) interacting with an ensemble of TLSs [81, 82, 70]. A significant difference between an ensemble and a SM is that we do not need to average over distributions of the TLS parameters E , Δ , and K (the TLS energy, the change of the SM transition frequency caused by the TLS jump, and the TLS relaxation rate respectively) because the SM interacts only with a specific environment. For each molecule $\vartheta(t) = \frac{1}{2} \sum_m \Delta_m \xi_m(t)$, where $\xi_m(t)$ are stochastic functions equal to 1 or -1. The index m refers to the m -th TLS. Using a quantity

$$F_m(\tau) = \left(\frac{\Delta_m}{2} \right)^2 \frac{|\sin(Y_m \tau)|^2}{|Y_m|^2} \operatorname{sech} \left(\frac{E_m}{2k_B T} \right)^2 e^{-K_m \tau}, \quad (39)$$

where T is the temperature, k_B is Boltzmann’s constant, and $Y^2 = (\Delta/2)^2 - K^2/4 + i(\Delta/2)K \tanh[E/(2k_B T)]$, the average can be written in the following form [70]:

$$\left\langle \exp \left(-i \int_0^\tau \vartheta(t') dt' + i \int_{t_w + \tau}^{t_w + 2\tau} \vartheta(t') dt' \right) \right\rangle = \prod_m \left\{ 1 - 2K_m \int_0^\tau F_m(\tau') d\tau' - (1 - e^{-K_m t_w}) F_m(\tau) \right\}. \quad (40)$$

Using an exponential form for $F_m(\tau)$

$$F_m(\tau) = B_m \{ \exp[(-2\text{Im}(Y_m) - K_m)\tau] + \exp[(2\text{Im}(Y_m) - K_m)\tau] \} - B_m \{ \exp[(-2i\text{Re}(Y_m) - K_m)\tau] + \exp[(2i\text{Re}(Y_m) - K_m)\tau] \} , \quad (41)$$

where $B = \Delta^2 |Y|^{-2} \text{sech}[E / (2kT)]^2 / 4$. The integral can be easily evaluated

$$\int_0^\tau F_m(\tau') d\tau' = B_m \left\{ \frac{1 - \exp[(-2\text{Im}(Y_m) - K_m)\tau]}{2\text{Im}(Y_m) + K_m} + \frac{\exp[(2\text{Im}(Y_m) - K_m)\tau] - 1}{2\text{Im}(Y_m) - K_m} \right\} + B_m \left\{ \frac{\exp[(2i\text{Re}(Y_m) - K_m)\tau] - 1}{K_m - 2i\text{Re}(Y_m)} + \frac{\exp[(-2i\text{Re}(Y_m) - K_m)\tau] - 1}{2i\text{Re}(Y_m) + K_m} \right\} \quad (42)$$

If TLSs have a broad distribution for K and Δ , then for each single molecule there will be very few TLS having $K \approx \Delta$. When most of the TLSs are either slow ($K^{-1}\Delta \gg 1$) or fast ($K\Delta^{-1} \gg 1$), equations can be simplified.

For slow TLSs:

$$Y \approx \frac{1}{2}\Delta + iK(p - \frac{1}{2}) \quad \text{and} \quad B \approx (p - p^2) = p\tilde{p} , \quad (43)$$

$$F(\tau) \approx p\tilde{p} \{ \exp[-2pK\tau] + \exp[-2K\tilde{p}\tau] - \exp[(-i\Delta - K)\tau] - \exp[(i\Delta - K)\tau] \} , \quad (44)$$

$$1 - 2K \int_0^\tau F(\tau') d\tau' \approx p \exp[-2\tilde{p}K\tau] + \tilde{p} \exp[-2pK\tau] , \quad (45)$$

where p is the probability of a TLS to be in the upper state and $\tilde{p} = 1 - p$ is the probability of a TLS to be in the lower state (in a thermodynamical equilibrium $\tanh[E / (2kT)] = (2p - 1)$, $\text{sech}[E / (2kT)]^2 = 4\tilde{p}p$). The observed line shapes are not Lorentzian and can only be approximately characterized by a linewidth. This linewidth can, for example, be equal to the FWHM or to the width of a Lorentzian which approximates experimental SM lines according to least squares criteria. The second definition is most often used by experimentalists. When the spectra are noisy, the FWHM is difficult to find.

Each slow TLSs contributes a value of $\delta\Gamma \approx K$ to the linewidth. Slow TLSs also shift and split the SM line. Very often there are very few slow TLSs which are nevertheless fast in comparison with the SM relaxation rate T_1^{-1} , because such TLSs should have a large

value of Δ . If TLSs are slow and $K \ll T_1^{-1}$ then further simplifications are possible leading to

$$\begin{aligned} \left\langle \exp \left[i \int_{t_w + \tau}^{t_w + 2\tau} \vartheta(t') dt' - i \int_0^{\tau} \vartheta(t') dt' \right] \right\rangle &= \\ &= \prod_m (1 - 2A_m(t_w) + A_m(t_w) \cdot \{ \exp(i\Delta_m \tau) + \text{c.c.} \}) \quad , \end{aligned} \quad (46)$$

where $A_m(t_w) = (1 - e^{-K_m t_w}) p_m \tilde{p}_m$ and c.c. stands for a complex conjugate. This expression is easily understood. Each TLS causes a splitting of the SM line into a triplet with a central Lorentzian peak of an amplitude $1 - 2A_m(t_w)$ at zero frequency and two smaller peaks of equal amplitude $A_m(t_w)$ with frequencies shifted to $\pm\Delta_m$. As a result of the product in Equation (46) all possible combinations of the shifts will appear.

For fast TLSs:

$$Y_m \approx i \frac{K_m}{2} \left(1 + i \frac{\Delta_m}{K_m} (2p - 1) - 2 \frac{\Delta_m^2}{K_m^2} p_m \tilde{p}_m \right) \quad \text{and} \quad B_m \approx \frac{\Delta_m^2}{K_m^2} p_m \tilde{p}_m \quad (47)$$

Since $B \ll 1$, the term $F_m(\tau)$ can be neglected. For the same reason the only non-negligible term in (42) is the one coming from $B \{ \exp[(2\text{Im}(Y) - K)\tau] - 1 \} / \{ 2\text{Im}(Y) - K \}$. It follows that

$$\left\langle \exp \left[i \int_{t_w + \tau}^{t_w + 2\tau} \vartheta(t') dt' - i \int_0^{\tau} \vartheta(t') dt' \right] \right\rangle = \exp[-2\Gamma_f \tau] \quad , \quad (48)$$

where

$$\Gamma_f = \sum_m p_m \tilde{p}_m \Delta_m^2 / K_m \quad . \quad (49)$$

Thus additional time independent broadening is the main effect of fast TLSs on the SM linewidth. In this case the ITFC does not produce any additional information in comparison with ordinary spectroscopy. The HWHM value obtained by doing ITFC is equal to the FWHM (usually labeled Γ_0) obtained from conventional slow scan spectra.

$$\Gamma_0 = 2\gamma + \frac{2\Delta^2}{K} \exp\left(-\frac{E}{k_B T}\right) \quad (50)$$

An ultimate goal for SMS could be to find parameters of all TLSs interacting with each molecule. A brief look at Eqs. (46, 48) reveals that even though ensemble averaging is removed a lot of information is hidden under the envelope of a SM spectrum if, for example, the splittings $\pm\Delta_m$ are much smaller than the natural linewidth $1 / T_1$.

Recovery of distributions of TLS parameters

For the following analysis we assume that $\omega' \ll \delta_i r$. In this case Eq. (38) can be solved easily for $P(\tau, \delta_i)$

$$P(\tau, \delta_i) \equiv \left\langle \exp \left[i \int_{\delta_i + \tau}^{\delta_i + 2\tau} \vartheta(t') dt' - i \int_0^{\tau} \vartheta(t') dt' \right] \right\rangle$$

$$= [1 + (T_1 r \tau)^2] e^{\tau/T_1} \int_{-\infty}^{\infty} e^{i\omega'\tau} S_{ITFC}(\omega', \delta_i) d\omega' , \quad \tau \geq 0 \quad (51)$$

Thus, in principle, the function $P(\tau, \delta_i)$ can be found if the ITFC spectrum and T_1 are known. Then, applying Eqs. (41, 42) and an appropriate fitting procedure, the parameters K , Δ and p can be determined. The problem however is not so simple when noise is present in the measured data. Though, again in principle, with the ITFC technique the noise can be reduced to the required level without any loss in the time resolution. Now we consider a few examples of ITFC when exact decomposition of $P(\tau, \delta_i)$ into components is not possible.

Small number of TLSs. This is probably the most common case when a single molecule is trapped in a crystal or when TLSs have been created artificially. The ITFC line consists of several overlapping Lorentzian peaks.

We applied the ITFC technique to study time dependence of the SM linewidths in the Shpol'skii system DPOT-tetradecane which was studied using TPE technique. Light emitted at a wavelength of approximately 888 nm by the single mode laser was focused onto a spot approximately 3 μm in diameter. The power of the laser beam was equal to 140 mW.

The data points in Fig. 13 represent the linewidths averaged over about 10 molecules, whose resonance frequencies are in the 3.7 GHz total scan range, as a function of the time resolution. To get this average, the ACF can be calculated for the whole 3.7 GHz trace in Fig. 11 at once. On a logarithmic time scale, the observed linewidth dependence appears as a step function. It indicates that in contrast to glasses, the distribution of TLSs in the DPOT-tetradecane system is remarkably different from the one assumed in the standard TLS model. A precise analytical form of the observed time evolution of the linewidth is not available but some semi empirical results are known from the literature.

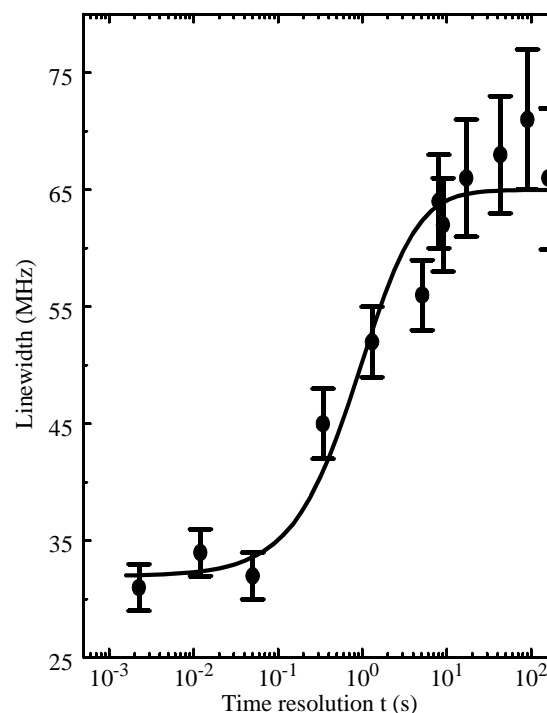


Fig. 13 Time dependence of the linewidth (half width at half maximum of S_{ITFC}) in TPE spectra. Each data point represents the average linewidth of 10 SMs. The solid line is a least squares fit with the trial function $\Gamma_0 + A(1 - (1 + ft)^{-2})$ with $\Gamma_0 = 31$ MHz, $A = 33$ MHz and $f = 0.5$ Hz

Light induced SD has also been observed in spectral hole burning experiments on dye doped polymethylmethacrylate. These observations were explained by interaction of the probe molecules with water molecules embedded in the polymer and flipping between two states under IR illumination. For those TLSs, a narrow distribution of the flip rates was assumed, and an approximate relation $\Gamma = \Gamma_0 + A(1 - (1 + ft)^{-2})$ describing the line broadening was deduced [83]. In this equation, A describes the interaction between a probe molecule and TLSs, and f approximately equals the TLSs flip rate. A similarity between hole-burning and ITFC discussed in relation to Fig. 10 allows us to apply the same empirical fit function. A fit to this equation is shown in Fig. 13. The fit yields a TLS flip rate of 0.5 Hz. This number should be considered as a rough estimate. Fig. 13 shows that there is no SD on the time scales $10^{-3} - 10^{-2}$ s and 10–200 s, where the linewidth remains almost constant (31 MHz and 65 MHz respectively). These values are still broadened by 3–5 MHz because of a small remaining saturation of the optical transition [12]. Thus, the linewidth is 26 – 28 MHz on a short time scale, in agreement with OPE data. OPE spectra

do not show spectral dynamics in the time range 10^{-3} – 10^2 s. This confirms that the difference between the SM linewidths in OPE and TPE spectra is caused by SD induced by the strong illumination at 888 nm. The dependence of the SD on the IR power was not studied in this work. First, the emission intensity under TPE depends on the square of the IR power and it was difficult to vary the power in a broad range. Second, the observed SD varies significantly from molecule to molecule.

One should keep in mind that despite of high time resolution, it may take a long time to obtain a good signal-to-noise ratio. Frequency jumps of 0.1 –10 GHz occurring on the time scale of 10^3 – 10^4 s made measurements of the same SM over the time range needed to obtain all the data points presented in Fig. 13 impossible. Such jumps have been observed under both OPE and TPE and have already been reported for other Shpol'skii systems [84]. Because of these dynamics and conventional photo bleaching, the molecular ensemble under study usually changes after one or two hours, even if the spectral range and the laser beam position are preserved. For this reason, only the average linewidth of 10 molecules is shown in Fig. 13. It must be emphasized that this averaging is not related to the ITFC method itself, which allows the study of SMs provided that they are photo stable.

Single molecules interacting with a set of TLSs having parameters distributed according to the standard TLS model. In this section an analysis of a SM in an amorphous matrix is based on the standard TLS model which assumes broad and flat distributions of TLS parameters. The main problem here caused by the very large number of TLSs (several hundred) coupled with each single molecule. Most of these TLSs have a small value of Δ and produce a quasi continuum of possible SM resonance frequencies. In principle, one still can apply Eq. (51) but the accuracy required for the ITFC function probably can not be obtained in a realistic experiment.

As follows from Eq. (46), the δ -peaks in the ITFC whose shift is equal to the sum of shifts related to each TLS and whose amplitude is equal to products of amplitudes of the single TLS related contributions. Thus δ -peak amplitudes are calculated as if every individual shift has a probability (amplitude). A general structure of the line shape can be found by making use of the Central Limit Theorem (CLT). It can be shown (see Appendix on page 94) that the probability distribution function for Δ reads

$$P(\Delta) \sim \Delta^{-2}. \quad (52)$$

Though a cutoff Δ_{min} can be introduced for small Δ [72], such a distribution function does not have a finite mean $\int_{\nu_{min}}^{\infty} P(\Delta)\Delta d\Delta$ and variance $\int_{\nu_{min}}^{\infty} P(\Delta)\Delta^2 d\Delta$ because the integrals diverge on the upper limit and the CLT can only be applied if TLSs with a large Δ , that is TLSs which are closest to the single molecule, are excluded. Such TLSs often can be identified when an ITFC line consists of more than one peak. When a line with two or more distinct peaks or shoulders is observed, the complete information about the TLS causing such a shape can be extracted from the ITFC spectra. Additionally, each distinct peak can be approximated by a Gaussian. The width of each Gauss-

ian is a slow function of the measuring time, and can be approximated by a logarithmic dependence. An example is shown in Fig. 14 where the line is a superposition of three Gaussians. The flip time of the TLS producing such a triplet is 1.3 ms. The amplitude of the side peaks evolves according to Eq. (46). The width of the each component decreases approximately logarithmically on a time between 1000 s and 0.1 ms. At a time $t_w = 10^{-5}$ s the time dependence significantly accelerates. This time coincides with the flipping time of another TLS whose two states are almost equally populated but whose Δ value is too small and the TLS simply contributes to the central peak width. In contrast, the COA predicts sudden disappearance of the side peaks at 1.3 ms time resolution and sudden reduction in the central peak linewidth at 10^{-5} s time resolution.

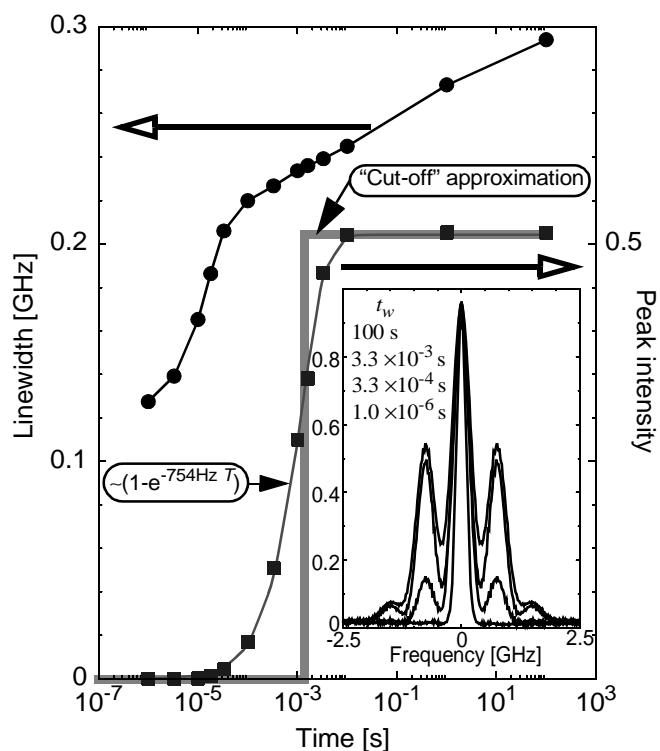


Fig. 14 Central peak linewidth and side peak intensity of the ITFC signal calculated for a single molecule in a polymer. The TLS energies and relaxations rates are distributed according to the standard TLS model. The inset shows the ITFC for different time resolutions. The noise level corresponds to 10^6 detected photo counts. A step function (thick grey line) shows the side peak time evolutions as described according to the cut-off approximation.

Experimental data are shown in Fig. 15. Two single molecules were studied with a time resolution between 100 s and 60 ms. A logarithmic decrease of the two linewidths is clearly observed. Interestingly, the extrapolation of the two curves to the life time limited resolution produces the life time limited linewidth. Of course in reality the linewidth evolution does not necessarily follow the same law over the whole time range and this result is probably a simple coincidence.

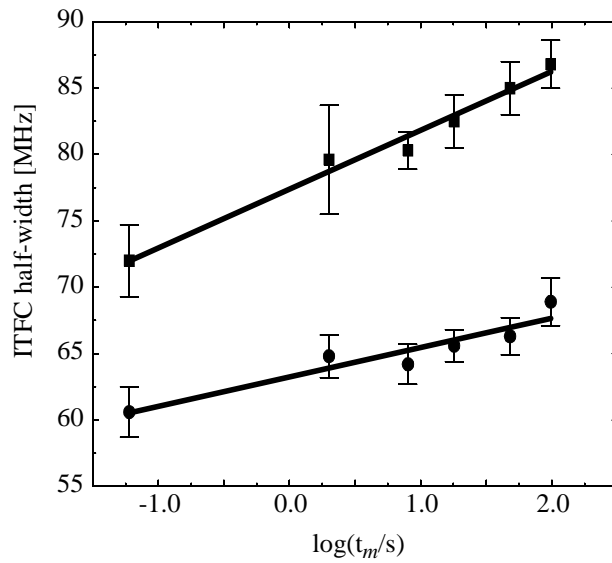


Fig. 15 ITFC for two single terrylene molecules embedded in polyethylene measured at 1.42 K. Within the errors of the measurements both curves approach 40 MHz linewidth when $t_m \rightarrow T_1$ that is ~ 4 ns.

IV. Nonequilibrium Phonons and ac-Stark Effect

Light induced spectral diffusion discussed in the previous chapter is not the only effect caused by the powerful laser illumination used for two-photon excitation. The relaxation of the CH-vibration produces a significant amount of so-called nonequilibrium phonons (NQPs). NQPs are acoustic phonons whose distribution function can not be characterized by a temperature. The presence of NQPs can be detected using high sensitivity of SM lines to changes of molecule's environment. But this is not simple. Direct interaction between probe molecules and the strong electromagnetic field may also effect the spectral lines. Because both effects are simultaneously present they should be analyzed together. Such an analysis is the main topic of this chapter.

Before discussing experimental results, a short theoretical introduction is appropriate. This introduction (in the part related to phonons) will be formulated in a way suitable for the description both equilibrium and nonequilibrium thermodynamic conditions.

The direct interaction of acoustic phonons with the electronic states of the chromophore is usually weak because acoustic modes of a crystal lattice are delocalized over a large volume and have small amplitudes at the chromophore's location. The chromophore interacts also with localized (pseudo localized) phonons whose region of existence is restricted to the probe molecule and its nearest surroundings. Such modes have a relatively strong coupling to the electronic degrees of freedom of the chromophore. If the frequency of such a mode is situated within the acoustic band, the mode is also coupled to the acoustic phonons.

A pseudo local phonon at a sufficiently low temperature such that only the two lowest states of the local vibration are significantly populated ($E \gg kT$) is an example of a TLS. The acoustic phonons play the role of thermal reservoir for the subsystem consisting of the pseudolocal phonon and the electronic states of the chromophore. The change of the molecular electronic transition frequency upon a TLS excitation by acoustic phonons is Δ . A sudden jump model [85, 86] implies that the transition frequency $\vartheta(t)$ follows a kind of telegraph function and jumps between two values ω_0 and $\omega_0 + \Delta$. The population rate of

the upper TLS state is k_u and the lifetime of that state is τ . If, in addition, the correlation time τ_c of this function, which is equal to $\tau/(k_u\tau + 1)$, is shorter than the measuring time, the line shape function $I(\omega - \omega_0)$ can be approximated in a spectral range $|\omega - \omega_0| \ll \tau_c^{-1}$ by a Lorentzian. Expressed in a different way, this condition says that the line is Lorentzian if $\Delta\tau_c \ll 1$. If $E \gg k_B T$ the line shape is always very close to a Lorentzian (see section *Non-Lorentzian Line Shapes*). Linear response theory predicts the following expressions for linewidth and line frequency [71]:

$$\Gamma = \gamma + \left[2\tau\Delta \cdot \frac{\Delta/2\pi}{1 + \tau^2\Delta^2} \right] \cdot k_u\tau = \Gamma_0 + \beta_\Gamma \cdot k_u\tau, \quad (53)$$

$$\nu = \nu_0 + \left[\frac{\Delta/2\pi}{1 + \tau^2\Delta^2} \right] \cdot k_u\tau = \nu_0 + \beta_\nu \cdot k_u\tau, \quad (54)$$

where γ and ν_0 are the linewidth and resonance frequency at $T = 0$ K. Here ν and Γ are in units of Hz, whereas Δ is an angular frequency in $\text{rad}\cdot\text{s}^{-1}$. β_Γ and β_ν are the corresponding expressions in square brackets. In thermal equilibrium, detailed balance requires that $k_u\tau = \exp\{-E/(k_B T)\}$. Introducing this expression into Eqs. (53, 54) yields

$$\Gamma(T) = \gamma + \beta_\Gamma \cdot \exp\{-E/(k_B T)\}, \quad (55)$$

$$\nu(T) = \nu_0 + \beta_\nu \cdot \exp\{-E/(k_B T)\}. \quad (56)$$

These equations have been shown to be very useful for the description of the temperature-dependent line broadening and line shift of optical transitions at temperatures below 10 K [17, 87, 88]. If $\tau^2\Delta^2 \ll 1$, Eq. (55) is equivalent to Eq. (50). Because a temperature can not be assigned to a NQP distribution function, the interaction between NQPs and local phonons can not be described by Eqs. (55, 56) and Eqs. (53, 54) should be used instead.

Experimental data may also show nonlinear effects caused by the very high electric fields required for two-photon excitation. The nonlinear ac-Stark effect is the most significant. In a classical interpretation, the ac-Stark shift is caused by the interaction between the dipole moment $\alpha \cdot F \cdot \cos(\omega t)$ induced by the laser electric field (α is the polarizability of an electronic state and F the electric field amplitude) and the inducing electric field. The resulting average energy shift

$$\delta E = -\frac{\alpha}{2} \cdot F^2 \cdot \langle \cos(\omega t)^2 \rangle = -\frac{\alpha}{4} \cdot F^2 \quad (57)$$

is different in the ground and excited electronic states because the corresponding polarizabilities are different. This leads to a change in the transition frequency proportional to the laser intensity. The lines are usually red shifted because the polarizability is usually larger in the excited state.

Experimental results are shown in Figs. 16 a and 16 b where one-photon excitation spectra (OPE) are compared to the two-photon excitation spectra (TPE) under conditions of approximately equal line shifts. Although data in Figs. 16 a and 16 b do not show the same molecules and the comparison is not direct, these molecules are quite representative and we focus now on the ratio $|\delta\Gamma/\delta\nu|$. In the OPE data in Fig. 16 b the linewidth increases by 110 MHz and the frequency shifts by -195 MHz upon a temperature change from 1.8 K to 5.15 K. This corresponds to $|\delta\Gamma/\delta\nu|_{OPE} \approx 0.5$. This broadening and shift could be explained by a single TLS mechanism described by Eqs. (55, 56). In the TPE spectra (Fig. 16 a), a shift of -160 MHz and a line broadening of 50 MHz is observed upon a laser power increase from 125 to 400 mW. Optical satu-

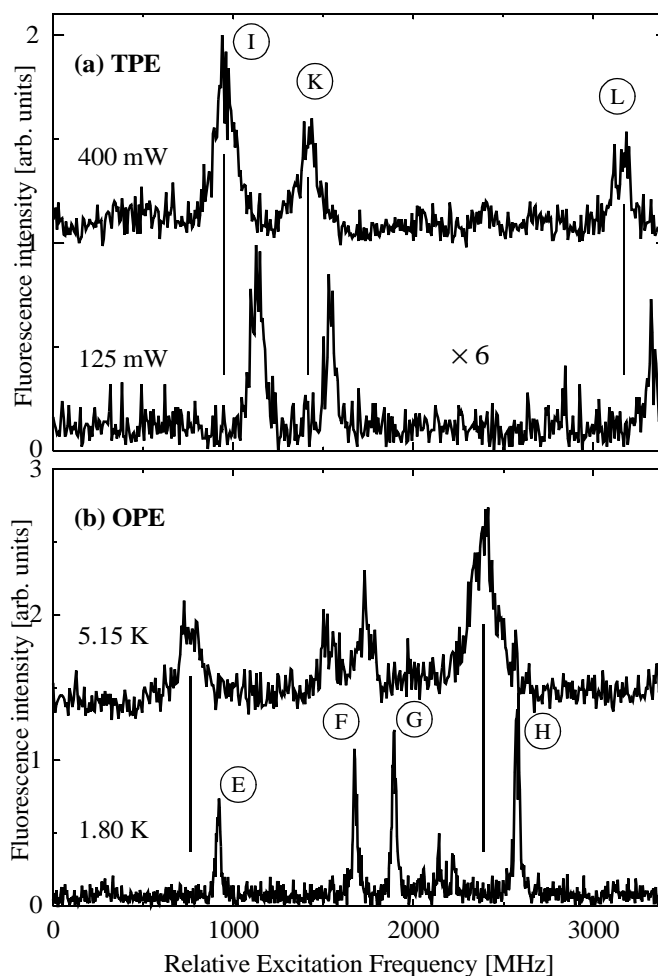


Fig. 16 Comparison of OPE and TPE spectra of DPOT in TD. (a) TPE data at a laser wavelength of 888.3 nm — the two-photon excitation spectrum of three molecules at 1.8 K. The excitation power is 125 mW (lower trace) and 400 mW (upper trace, shifted for clarity). The line shift associated with this power increase is about -160 MHz; the corresponding line broadening is about 50 MHz. (b) OPE data at a laser wavelength of 444.2 nm at 1.8 K (lower trace) and 5.15 K (upper trace, shifted for clarity). The line shift associated with this temperature increase is between -175 MHz (molecule E) and -215 MHz (molecule H), the corresponding line broadenings are about 110 MHz.

ration accounts for not less than 35 MHz of broadening [12] and we find that $|\delta\Gamma/\delta\nu|_{TPE}$ is about 5 times smaller than $|\delta\Gamma/\delta\nu|_{OPE}$.

An increase of the temperature in the middle of the laser spot during TPE experiments (if we take $|\delta\Gamma/\delta\nu| = 0.5$ for thermal phonons effect) can account only for a shift of $(50 \text{ MHz} - 35 \text{ MHz})/0.5 \approx 30 \text{ MHz}$. It is difficult to estimate the contribution to the shift from the ac-Stark effect because ac-polarizabilities are not known for DPOT and the exact laser intensity at the molecule location is hard to measure. Based on dc-polarizabilities (which can be significantly larger or smaller than ac-polarizabilities) and assuming that the molecule was in the center of a focal spot of 2 μm diameter (which is slightly larger than the diffraction limited value) the estimate gives 50 MHz red shift between the data taken at 125 and 400 mW laser power. The remaining shift of about $160 \text{ MHz} - 30 \text{ MHz} - 50 \text{ MHz} = 80 \text{ MHz}$ indicates that an additional line shift mechanism is activated in the TPE experiment or that the ac-Stark contribution is approximately 3 times larger. The latter can not be ruled out on the basis of available data and the observed shifts might be attributed without contradiction solely to an ac-Stark effect.

An alternative explanation involves NQP. We note that the important parameter $\delta\Gamma/\delta\nu = \beta_r/\beta_v = 2\Delta\tau$ is smaller for local vibrations with a larger energy because $\tau \sim E^{-2}$ [89]. Thus such phonons could cause a large shift while contributing very little to the broadening. Of course for excitation of these phonons a higher temperature is required. In thermal equilibrium at high temperatures a very large broadening because of low energy local phonons would make lines almost invisible. But the situation is quite different if NQP are taken into account. Because NQPs are produced by a down conversion from a high energy vibration there are much more higher energy phonons than predicted by the Boltzmann distribution. The excess of the NQP concentration is further enhanced by the fact that the elastic scattering cross-section of acoustic phonons is proportional to ω^4 . Thus the mean free path for NQPs is much smaller than for low-frequency equilibrium phonons and the latter escape from the hot laser spot much faster. Rough estimates show that NQPs can contribute 100MHz to the shift while contributing only 10MHz to the broadening and thus are thought to be responsible for the extra shift in the TPE spectra. Additional theoretical and experimental studies are needed to identify the main contributions to the shifts.

Details

Temperature effects

Within the model of a single local mode the zero-phonon line (ZPL) consists, in addition to the conventional Lorentzian, of a dispersive component and a side band (see Section V). The relative amplitude of the dispersive component was estimated to be smaller than 2% and is thus below the noise level of the present data. The latter holds also for the sideband. Therefore simple Lorentzians were fitted to the experimental SM spectra to determine linewidths and frequencies for all temperatures. The differences $\delta\Gamma(T)$ and $\delta\nu(T)$ were then fitted to Eqs. (55) and (56). An example is shown in Fig. 17. In this case no sig-

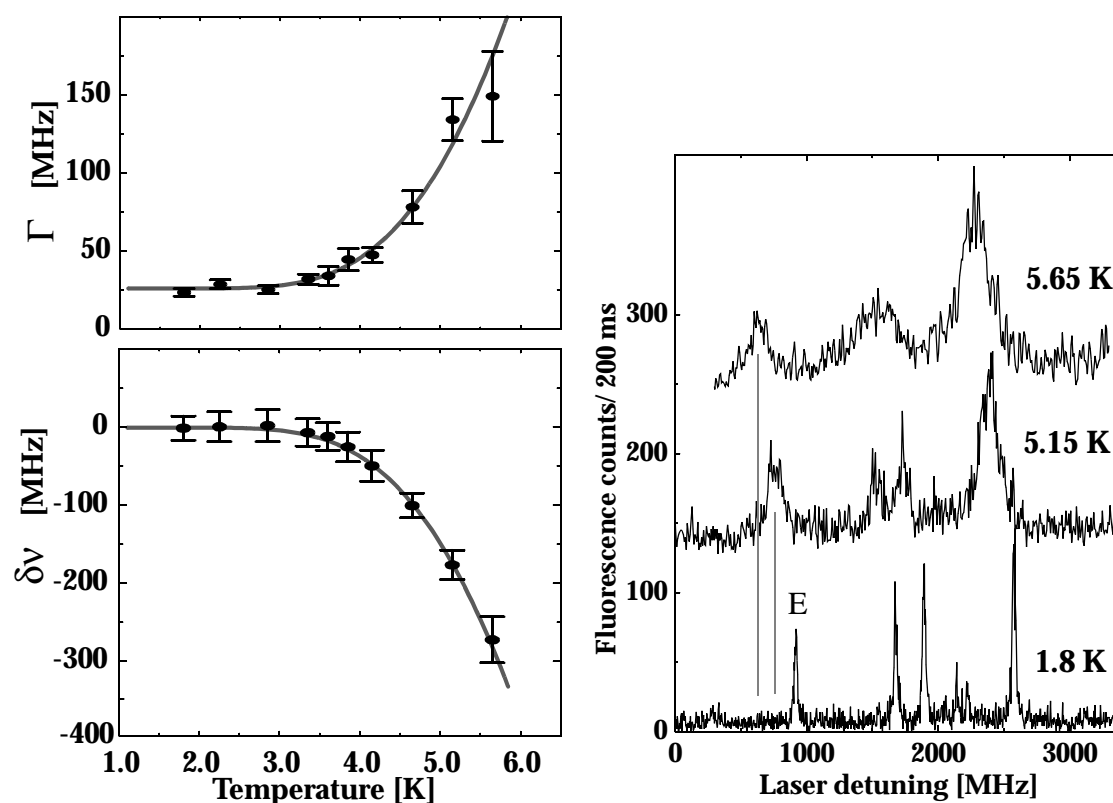


Fig. 17 Four single molecules measured at three temperatures and systematically studied temperature dependencies for one of them (molecule E).

nificant deviations from the exponential law is observed. For all four molecules shown in Fig. 17 the parameter of interest $\delta\Gamma/\delta\nu \approx 0.5$.

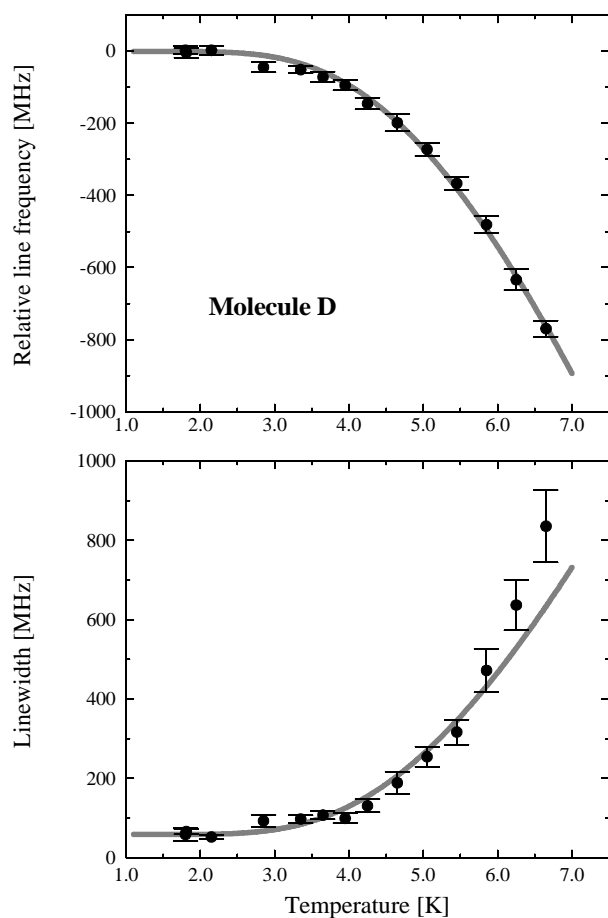


Fig. 18 Temperature dependence of the resonance frequency and the linewidth of molecule D. The solid lines are least squares fits with Eqs. (55) and (56), respectively. The local phonon parameters are given in Table

For all nine molecules for which the line shape as a function of temperature was measured there was no significant temperature dependence of the line frequencies and linewidths below 3 K. Therefore we set Γ_0 and ν_0 equal to the average of the values between 1.8 K and 2.5 K. The parameters are listed in Table 1. Good agreement with the activation laws was obtained at lower temperatures but at temperatures above 6 K there are significant deviations. For molecule D the linewidths and line shifts are shown in Fig. 18 together with the fits. The disagreement is clear. These deviations are more pronounced for the broadening than for the shift partially because the errors are smaller for the frequencies and when the two curves are fitted together the weighted

least squares fit gives a higher priority to the frequency shift data. Bulk phonons may be also the reason for the deviations because they lead to a broadening that grows faster than the shift with increasing temperature [91].

The activation energies of the 9 molecules in Table 1 are between 14 cm^{-1} and 19 cm^{-1} and the lifetimes within 1 -3 ps. Similar results were observed for octatetraene in n-hexane [92]. The width-to-shift ratios are in the range of $0.4 < |\delta\Gamma/\delta\nu| < 1$.

TABLE 1. Linewidth, activation energies, and related parameters of single DPOT molecules in TD obtained from the temperature dependent one-photon excitation spectra. The ensemble values determined from the SFS investigations are also presented.

| Molecule | Γ_0 [MHz] | E/hc [cm ⁻¹] | β_Γ [GHz] | β_ν [GHz] | $ \beta_\Gamma / \beta_\nu $ | $\Delta/2\pi$ [GHz] | τ [ps] |
|---------------------------|---------------------|-------------------------------|-------------------------|----------------------|------------------------------|------------------------|----------------|
| A | 27.5 | 17.2 | 11.8 | -31.4 | 0.38 | -32.5 | 0.9 |
| B | 18.0 | 17.9 | 24.1 | -25.3 | 0.96 | -31.0 | 2.5 |
| C | 35.0 | 17.3 | 15.7 | -24.4 | 0.64 | -26.9 | 1.9 |
| D | 58.5 | 14.6 | 13.5 | -18.0 | 0.76 | -20.5 | 2.9 |
| E | 25.7 | 18.9 | 18.6 | -34.8 | 0.54 | -37.3 | 1.1 |
| F | 22.2 | 17.0 | 9.4 | -20.2 | 0.48 | -21.3 | 1.8 |
| G | 26.6 | 15.9 | 7.0 | -15.8 | 0.44 | -16.6 | 2.1 |
| H | 29.2 | 16.7 | 11.0 | -21.1 | 0.56 | -22.5 | 1.8 |
| J | 32.0 | 18.9 | 13.6 | -34.2 | 0.40 | -35.5 | 0.9 |
| average | 30.5 | 17.2 | 14 | -25 | 0.57 | -27 | 1.7 |
| SFS (same sample) | 25.0 | 20.7 | 16.8 | -38 | 0.44 | -40 | 0.9 |
| SFS (different sample) | 26.0 | 19.7 | 15.0 | -42 | 0.36 | -43 | 0.7 |

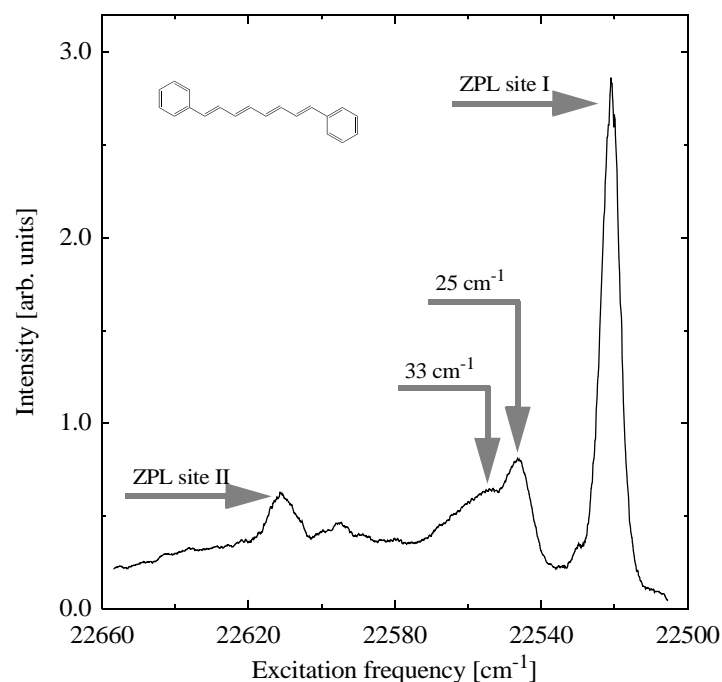


Fig. 19 Two-photon excitation spectrum of the $S_1 \leftarrow S_0$ transition of DPOT in TD at 1.8 K. The 0-0 zero-phonon line (ZPL) at 22521 cm^{-1} (444.0 nm) corresponds to a site of broken molecular symmetry (site I). The line around 22625 cm^{-1} is the ZPL of a site of unbroken symmetry (site II). Note that the molecular frequency scale is used which corresponds to twice the laser frequency in the case of two-photon excitation.

To relate the fitted activation energies to local phonon modes, the TPE spectrum of DPOT in TD at 1.8 K is shown in Fig. 19. The 0-0 ZPL at $22,521 \text{ cm}^{-1}$ is assigned to a chromophore located at the non-centrosymmetric site I. This line was also observed under OP excitation [93]. The line at around $22,625 \text{ cm}^{-1}$ (442.1 nm) is the ZPL of DPOT located at the centrosymmetric site II and is absent in OP excitation spectra. Here we study exclusively spectra assigned to site I. Two peaks at 25 cm^{-1} and 33 cm^{-1} are clearly resolved in the phonon band of

the ZPL of site I. Both frequencies are larger than the local mode frequencies obtained from the activation laws. We argue that local vibrations crucial for the broadening and shift need not necessarily be strongly active modes in allowed electronic transitions. In a hole-burning study of phthalocyanine doped TD, Rebane et al.[94] reported that the phonon frequency obtained from the sideband was about twice the activation frequency determined from the temperature dependent line broadening. It was concluded that the local mode detected in the side band was totally symmetric while the mode of the activation process was non-totally symmetric. Using the same argument, we conclude that the local modes responsible for the activation behavior of the linewidths and shifts are of low symmetry.

When dealing with single molecules, there is always a question about the degree of statistical representativeness of observed properties (see section *Principles of Data Analysis*). In order to compare SM with ensemble data we investigated the statistical fine structure (see Eq. (3) in *Molecules Interact with Light*) of OPE spectra [96]. From the

autocorrelation function of the spectra we determined the ensemble linewidth for each temperature and from the cross-correlation function calculated from spectra at different temperatures we determined the temperature dependent frequency shifts of the ensemble. The results obtained from two different samples are also given in Table 1. A reasonable agreement between the SM and the SFS data is observed. We thus conclude that the molecules A - J form a representative set.

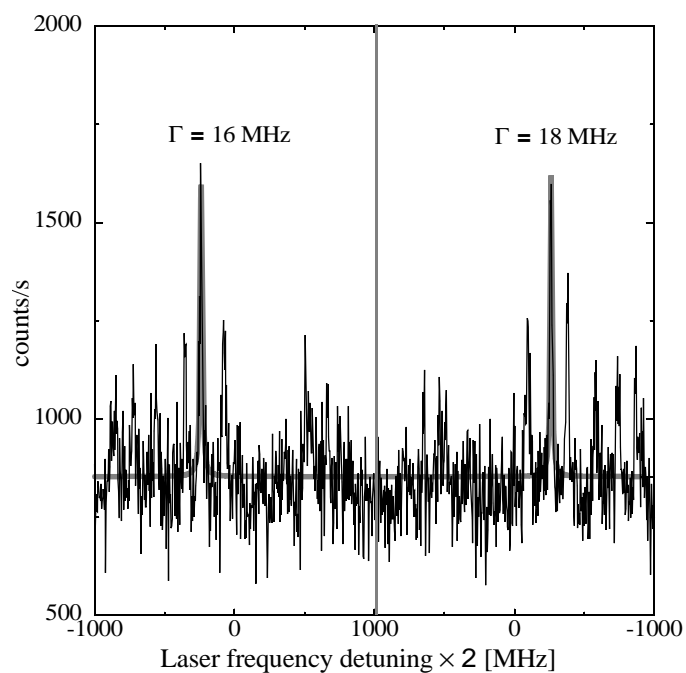


Fig. 20 An example of a single molecule line having the width of 17(2) MHz. The spectrum was measured twice to show its reproducibility.

of a single molecule line with a linewidth close to the lifetime limited value is shown in Fig. 20. We speculate that the origin of the additional broadening is spectral diffusion from saturated TLS dynamics.

When the same system was investigated using TPE technique, a light-induced frequency shift of the 0-0 line was observed. The observation can be explained in terms of light-induced thermal effects, ac Stark shifts, and/or effects caused by non-equilibrium phonons. All these contributions are related to the very high laser powers (on the order of 10 MW/cm^2) needed for TPE and are analyzed in the next two subsections.

The measured linewidths are now compared with the lifetime limited value. The lifetime was determined from the decay of the $S_1 \rightarrow S_0$ fluorescence of DPOT in TD at 1.8 K. The measurements yielded 11.0(5) ns corresponding to a homogeneous linewidth of 14.5 MHz. This value, although measured for the bulk, is considered as a lower bound for the linewidth of the individual chromophores. Only very few of the measured linewidths are close to the limiting value of 14.5 MHz, most of the measurements exceed this value typically by 5-20 MHz. An example

High laser power effects

To avoid a systematic error because of the laser frequency instability, measurements as a function of the laser power were taken in a random order (Fig.21). For all molecules, the frequency shift could be satisfactorily fit to a linear function of the power. The average shift coefficient for the investigated molecules was 600 MHz/W. In contrast to the line frequencies, the line widths were almost insensitive to the laser power though they were 2-3 times larger than under one-photon excitation. This difference is caused by LISD discussed in Section III. A small broadening was observed at powers above 250 mW, which can be explained by optical

saturation because of the triplet bottleneck. To exclude saturation broadening, only line-widths measured at powers below 250 mW have been taken into account. In this region, the broadening was at least 5 times smaller than the line shift (see Table 2).

The average value of $\delta\Gamma/\delta\nu \approx 0.1$ is supported by the TPE-SFS analysis. From the auto- and cross-correlation functions of the SFS data we observed that upon an increase of the laser power from 70 to 340 mW the lines shift to lower frequencies by approximately 44 MHz and broaden by less than 9 MHz. An upper limit of 0.2 results for the width-to-shift ratio which is further an upper limit because power-broadening is not taken into account. The increase in width and shift is much smaller for the SFS than for the SM technique because an average is taken over the spatially inhomogeneous laser field in the illuminated spot by the SFS. The average laser field is considerably smaller than the field

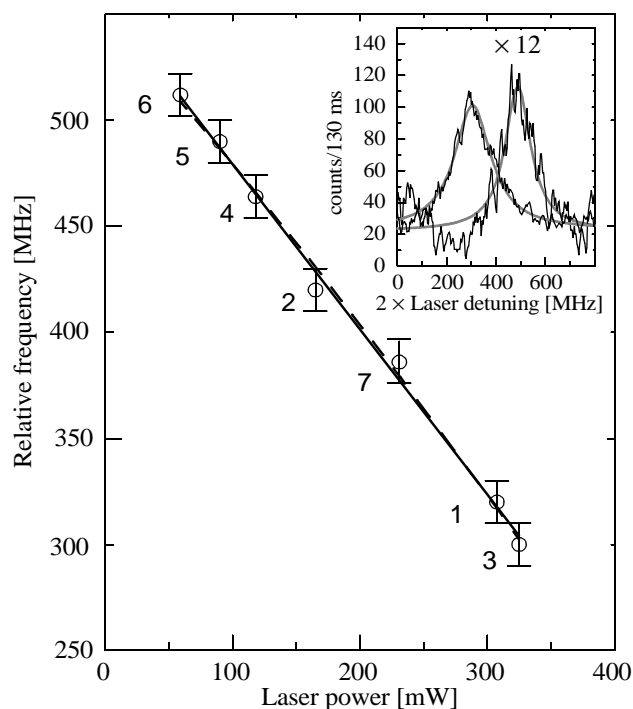


Fig. 21 Line shift power dependence observed for a SM (molecule 1 in the Table). The circles are the experimental data. The numbers near the data points show the order in which they were measured. The solid line is a linear fit. The inset shows the SM line measured at 320 mW (left) and 90 mW (right) with Lorentzian fits.

at the center of the spot relevant for the SM detection. Concluding, the SFS data confirm that in TPE spectra the width-to-shift ratio is ~ 0.1 .

Temperature increase. The temperature increase of the matrix under TPE can now be estimated using the data of OPE. Assuming that the broadening of 15 MHz, owing to a power increase from 125 to 400 mW, results solely from the warming of the matrix, a temperature increase from 1.8 to 3.5 K is calculated when using the average parameters of Table I.

At temperatures below 4 K the phonon mean free path is expected to be larger than the size of the micro crystallite of approximately $10 \times 20 \times 20 \mu\text{m}$. At the crystallite surfaces the heat transport is governed by the resistance of the heat transfer to the reservoir (Kapitza resistance). This resistance leads to a temperature increase within the micro crystallite. Owing to the

Kapitza resistance, the temperature in a solid near an interface with liquid He, T_i , and the He bath temperature T_b are related by the equation $T_i^4 - T_b^4 = \chi q$, where q is the heat flux through the surface, and χ is a coefficient. Acoustic impedance theory provides an estimate, which usually exceeds the experimental values by an order of magnitude, of $\chi \ll 6.2 \times 10^{-7} [W^{-1} g^{-1} cm] \omega_D^3 M \approx 60 \text{ cm}^{-2} W^{-1}$, where ω_D is the Debye frequency of the solid ($\sim 80 \text{ cm}^{-1}$ for TD), and M is its molar mass (198 g/mol). In the steady state case, the heat flux is proportional to the laser power P , that is $q = \zeta P$. An estimate for ζ reads

TABLE 2. Power dependence of the line frequency and the linewidth for 11 SMs. The excitation power was changed within the range 60 ÷ 400 mW. Γ_0 is the low power limit of the linewidth. In SMS it is difficult to avoid a selection when only the strongest SM lines are measured. One has to be careful when extrapolating SM data to the ensemble average.

| Mol. No | Shift [MHz/W] | Γ_0 [MHz] (linear fit) | Broadening [MHz/W] |
|---------|----------------|-------------------------------|--------------------|
| 1 | -800 ± 25 | 120 ± 40 | 150 ± 160 |
| 2 | -600 ± 120 | $60 \pm 30^*$ | - * |
| 3 | -900 ± 300 | $80 \pm 30^*$ | - * |
| 4 | -520 ± 80 | 50 ± 20 | 30 ± 50 |
| 5 | -600 ± 45 | 55 ± 15 | 60 ± 60 |
| 6 | -630 ± 90 | 63 ± 6 | 30 ± 40 |
| 7 | -500 ± 80 | 60 ± 18 | 60 ± 60 |
| 8 | -600 ± 60 | 36 ± 18 | 160 ± 100 |
| 9 | -580 ± 80 | 55 ± 25 | 70 ± 120 |
| 10 | -600 ± 50 | $100 \pm 50^*$ | - * |
| 11 | -680 ± 80 | $140 \pm 40^*$ | - * |

* The linewidth fluctuations from scan to scan (probably due to small frequency jumps when taking spectra) have not allowed us to estimate the line broadening and Γ_0 . The mean value of Γ and its standard deviation (measured at low power) is given instead of Γ_0 .

$\zeta \approx \varepsilon d / d^2 = \varepsilon / d$, where d is the crystal size and ε is the absorption coefficient of the crystal. Based on the micro crystal size $d \approx 1.4 \times 10^{-3}$ cm and $\varepsilon = 0.017$ cm⁻¹ the result is $\zeta \approx 12$ cm⁻². The film boiling was observed at $P \approx 500$ mW or at a heat flux of $\zeta \times 0.5 W = 6$ Wcm⁻². This is in reasonable agreement with the critical flux of around 10 Wcm⁻² at $T_b = 1.9$ K reported in the literature [97]. At very low temperature, the thermal conductivity is proportional to the specific heat, i.e. to T^3 . In this case, $T^4 - T_\infty^4 \approx \varepsilon P T_\infty^3 / k_\infty$ yields the steady state temperature T in the excited volume, where $T_\infty \approx T_i$ is the temperature far from the laser spot and k_∞ is the thermal conductivity at $T = T_\infty$. Hence $T^4 - T_b^4 \approx (\varepsilon T_\infty^3 / k_\infty + \chi \zeta) P \equiv \Lambda P$, where an estimate for Λ based on the impedance theory reads $\Lambda \approx 750$ cm⁻⁴W⁻¹. To obtain the temperature increase from 2.6 K to 3.4 K when $T_\infty = 1.7$ K and the laser power increases from 125 mW to 400 mW one should assume $\Lambda = 80$ cm⁻⁴W⁻¹. Which is in a reasonable agreement with the above estimate.

Ac-Stark effect. In DPOT the strong transition dipole moments are aligned parallel to the long axis of the molecule [98]. Therefore only the component of the polarizability tensor parallel to the long axis is considered. We thus write for the molecule in the solid

$$\delta v_{Stark} = -\frac{1}{2hc\varepsilon_0} R^2 L^2 \cos^2 \beta \delta \alpha I, \quad (58)$$

where c is the speed of light, ε_0 is the permittivity of vacuum, and $\cos \beta$ is the direction cosine of the field polarization relative to the molecular axis. I is the laser intensity at the location of the molecule in the absence of the dielectric matrix (in units of Wm⁻²). In Eq. (58) we have also considered electric field corrections: $\mathfrak{R} = 2/(1 + \sqrt{\varepsilon})$ accounts for the reflection of the incident field on the sample surface and $L = (1 + \varepsilon)/3$ is the Lorentz field correction, where ε is the relative dielectric constant. The dynamic polarizabilities of the ground and excited state are:

$$\alpha_g(\nu) = 2 \sum_i \frac{|\langle g | \hat{\mu} | i \rangle|^2}{E_i} \cdot \frac{1}{1 - [h\nu / E_i]^2} \quad (59)$$

and

$$\alpha_e(\nu) = 2 \sum_i \frac{|\langle e | \hat{\mu} | i \rangle|^2}{E_i - E_e} \cdot \frac{1}{1 - [h\nu / (E_i - E_e)]^2}, \quad (60)$$

where the sums run over all states i with energy E_i and wave function $|i\rangle$. $\hat{\mu}$ is the electric dipole moment operator. For resonant TPE $2h\nu = E_e$.

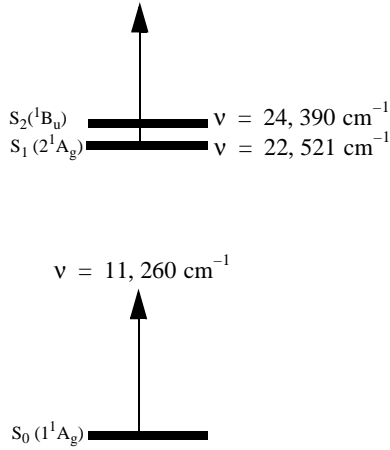


Fig. 22 Electronic energy levels of DPOT in TD. The laser frequency is shown by the arrows. Note a small difference between S_2 and S_1 states.

Unfortunately, there are not sufficient data available about the excited state energies and transition dipole moments of DPOT for a reliable calculation of the dynamic polarizabilities. For an estimate we consider the dc-polarizabilities parallel to the long molecular axis

$$\alpha_g^{\text{dc}} = 10^{-38} \text{ C V}^{-1} \text{ m}^2 \quad [99] \quad \text{and}$$

$$\alpha_e^{\text{dc}} = 1.65 \times 10^{-38} \text{ C V}^{-1} \text{ m}^2 \quad [100] \quad \text{yielding}$$

$$\delta\alpha_e^{\text{dc}} = 0.65 \times 10^{-38} \text{ C V}^{-1} \text{ m}^2.$$

Taking into account the laser spot size of $2\mu\text{m}$ diameter, the angle β of approximately 60° [95, 96], and the dielectric constant $\epsilon = 2.1$, we get $\delta\nu/\delta P \approx -180 \text{ MHz W}^{-1}$. This value is significantly smaller than the observed value of $\delta\nu/\delta P \approx -(500 \div 1000) \text{ MHz W}^{-1}$. From Eqs. (59, 60)

it follows that the ac-values are larger than the dc-values in general so that one might expect that $\delta\alpha_e^{\text{dc}} > \delta\alpha_e^{\text{ac}}$. However, a substantial contribution to the sum is from the second electronically excited state $|i\rangle = |S_2\rangle$ at $24,390 \text{ cm}^{-1}$ (see Fig. 22). This state contributes with a negative sign to the sum in Eq. (60) so that the dc-value could also be larger than the ac-value. Furthermore, the $|S_1\rangle$ and $|S_2\rangle$ states are close to each other, so that the matrix distortion of the molecule induces a strong interaction between these states. This makes the calculation of the dc-polarizabilities of the two states complicated [100]. We conclude from the data at disposal that the observed shifts might be attributed, without contradiction, solely to an ac-Stark effect.

The phonon bottleneck model. One part of the irradiated laser power is absorbed by the host molecules and dissipated into the lattice. This effect was directly observed by the onset of film boiling of the He at a laser power of 500 mW. The question thus arises whether

the absorption and release of energy leads to highly non-equilibrium conditions and to a significant warming of the laser spot.

At temperatures as low as a few Kelvins the relaxation and thermalization of the absorbed energy is a complicated process. The molecular vibrational energy is released to lattice vibrations at non-thermal energies which give rise to pumping phonon modes that otherwise would have negligible probability of population by thermal activation. The elastic and inelastic scattering probabilities and the mean free paths of the phonons depend on their frequencies [90]. Thus the heat transport takes place ballistically and diffusively through the micro crystallites (typically of 10-30 μm size).

A more detailed scenario of relaxation and associated phonon mediated processes is schematically shown in Fig. 23. The IR irradiation is weakly absorbed by the third overtone of the C-H stretching mode at $10,730\text{ cm}^{-1}$ of the matrix molecules. The absorption coefficient can be estimated from the absorption spectrum which was recorded at room temperature and is presented in the inset of Fig. 23. At 888 nm the absorptivity is 0.008 cm^{-1} corresponding to an absorption coefficient of $\epsilon = 0.017\text{ cm}^{-1}$. Accordingly, the excitation rate of the matrix molecules is about 3 kHz at a laser intensity of 12 MW/cm^2 at the center of the laser-light focus. The vibrational energy is released by an unspecified relaxation path including internal molecular and lattice vibrations. Because

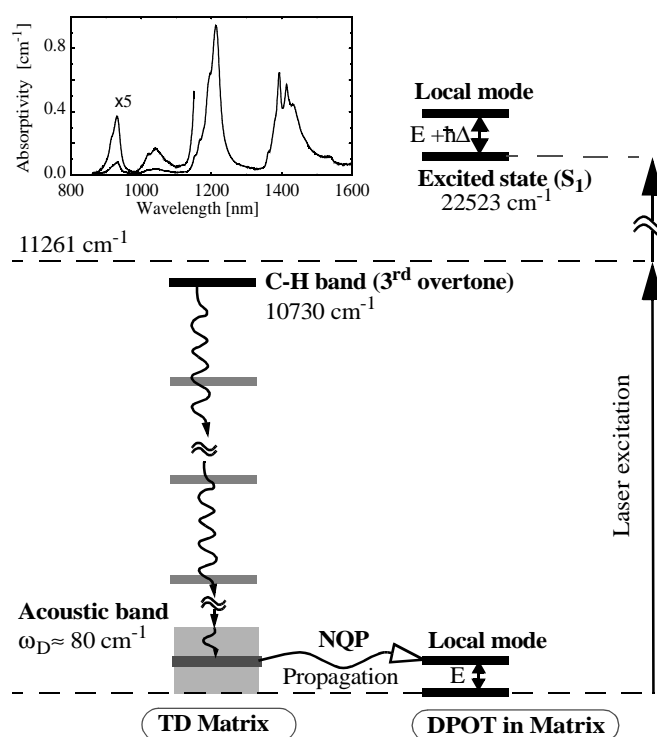


Fig. 23 Schematic representation of the processes taking place upon intense laser irradiation at 888 nm of the DPOT/TD system. In the matrix, the third overtone of the C-H vibration is excited. NQP are generated by vibrational relaxation. The NQP propagate and interact with the chromophore's local mode. The chromophore is optically cycled between the ground and S_1 excited state by two-photon laser excitation. The inset shows the absorption spectrum of TD at room temperature. The absorptivity at 888 nm is 0.008 cm^{-1} , corresponding to an absorption coefficient of $\epsilon = 0.017\text{ cm}^{-1}$.

multi-phonon transitions presumably play a dominant role in the relaxation, the pumping

of acoustic phonons takes place primarily at higher phonon frequencies below the Debye frequency ω_D , giving rise to non-equilibrium phonons (NQP) [90].

Since the IR energy is absorbed by the host molecules, high energy molecular vibrations and NQPs are generated everywhere in the laser spot and may interfere with chromophores and TLSs before thermalization. In the previous chapter, it was shown that the broadening in TPE spectra increases with the frequency-scan time which is a signature of spectral diffusion. Because the linewidths, recorded in the limit of fast scans in TP spectra, are equal to the ones of OPE spectra, a significant matrix heating can be ruled out up to a power of 140 mW, at which the ITFC study was carried out. Thus the remarkable conclusion follows that the LISD observed for slow TPE scans, has to be assigned to TLSs triggered by NQPs but not by thermalized phonons.

Because of the random distribution of the TLSs, the spectral diffusion changes from molecule to molecule. In fact, 2-3 times fewer SMs were detected in TPE than in OPE spectra (see Fig. 24). This can be explained by spectral diffusion so strong that up to 30%

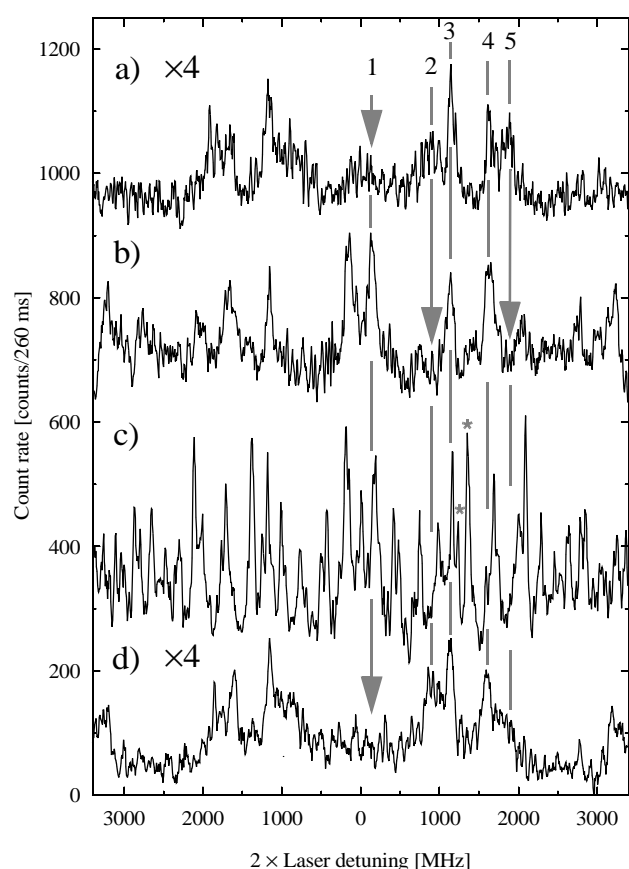


Fig. 24 Excitation spectra of single molecules measured under different conditions. **(a)** TPE with 350 mW power at the fundamental laser wavelength (≈ 888.4 nm); **(b)** OPE with 500 nW at second harmonic laser frequency ($\lambda \approx 444.2$ nm) when the sample was simultaneously illuminated with 350 mW at the fundamental laser wavelength; **(c)** OPE (500 nW); **(d)** TPE (350 mW) a reproducibility check of scan **(a)**. Spectra **(a)**, **(b)**, and **(c)** are shifted on the vertical scale for clarity. The spectra were measured in the order **(a)**, **(b)**, **(c)**, **(d)**. Comparison of **(a)** and **(d)** shows that there was no laser frequency drift (see SM lines 3 and 4). The TPE spectra **(a)** and **(d)** have the vertical scale expanded by a factor of 4. The contribution from TPE itself to the spectrum **(b)** is less than 25%. The number of SMs seen in the OPE spectrum **(c)** is approximately twice the number in the spectra **(a)**, **(b)**, and **(d)**. The 0-0 line of molecules 3 and 4 can be observed under both OPE **(b)** and TPE **(a)**, **(d)**. Taking into account the light induced shift, molecule 3 most likely originates from one of the two molecules labeled by asterisks in pure OPE spectrum **(c)**. The vertical lines give a view guide for convenience.

of all DPOT molecules were no longer detectable. From the thermal broadening measured

with OPE it follows that there is no dramatic difference in sensitivity of different single molecules to a temperature increase. Thus we conclude that there is a significant variation in the sensitivity of single molecules to the excitation of high energy vibrational modes (NQPs).

Because a large amount of energy is released in a small volume, the laser spot represents a system far from equilibrium. We thus speculate whether NQPs, which trigger the TLSs, may also pump higher frequency local modes. Our discussion is based on the following scaling laws valid for the Debye model [101]: $\tau_{dec} \propto \omega^{-5}$ for the phonon decay-time, $\tau_{scat} \propto \omega^{-4}$ for the elastic phonon scattering time, $l \approx s\tau_{scat} \propto \omega^{-4}$ for the mean-free scattering path, $D = l^2/\tau_{scat} \propto \omega^{-4}$, $L \approx \sqrt{D\tau_{dec}} \propto \omega^{-9/2}$ for the diffusion length (the distance from the origin which phonons propagate before they decay into phonons of different frequency), and $V_{dif} \propto L^3 \propto \omega^{-27/2}$ for the diffusion volume, where s denotes the sound velocity. The large exponents indicate that the behavior of the system may change completely if the phonon frequency is altered. Above a critical phonon frequency ω_c the diffusion length is expected to be smaller than the spot size. Thus for frequencies $\omega > \omega_c$ the propagating phonons do not escape from the excitation volume before decay and the pumping and relaxation mechanisms can be assumed to be homogeneous in space. Below ω_c the diffusion length and the mean free path become much larger than the spot size. A fast escape from the laser spot takes place bounded solely by the micro crystallite surfaces. Therefore, the critical frequency ω_c acts as a *bottleneck* in the occupancy of phonon states in the laser spot.

The photons with frequency of 10^4 cm^{-1} are absorbed at a rate of 3 kHz per matrix molecule. This corresponds to a absorbed power of $\dot{Q} \approx 3 \cdot \hbar \times 10^7 \text{ cm}^{-1} \text{ s}^{-1}$ per molecule. The absorbed energy is quickly released into lattice vibrations which propagate through the crystal lattice. To estimate the NQP population we make the following assumptions.

- i) All phonon modes with $\omega_c < \omega < \omega_D$ are equally pumped.
- ii) Phonons decay spontaneously into two phonons of equal frequency. Thus for $2\omega_c \geq \omega_D$ only one generation of phonons has to be considered.

The estimates, calculated below, do not significantly change, when these assumptions are modified, for instance when the pumping of phonons is restricted to frequencies close to ω_D and the first relaxation generation is considered in detail (see Appendix).

From the balance between pumping and decay the phonon occupancy obeys the scaling law $n_{NQP} \propto \tau_{dec} \propto \omega^{-5}$. Below ω_c the probability of the NQPs to remain in the laser spot scales as $V_{dif}^{-1} \propto \omega^{27/2}$. Therefore the occupancy of phonons in the laser spot is assumed to follow the scaling law $n_{NQP} \propto \omega^{11/2}$, where the phonon density of states and the conservation of energy is taken into account. From the heat capacity measurements of TD we estimate the Debye frequency $\omega_D/(2\pi c) \approx 80 \text{ cm}^{-1}$ and for the critical frequency we are motivated by the peaks in the phonon band in Fig. 2 to chose $\omega_c/(2\pi c) \approx 35 \text{ cm}^{-1}$. This value is slightly below $\omega_D/2$, nevertheless, we consider only one generation of the phonon relaxation.

We next estimate the phonon lifetime from the expression [102]

$$\tau_{dec} = \frac{\rho s_L^5}{h\phi^2\pi^3} \left(1 + 2\left(\frac{s_L}{s_T}\right)^3\right) v^{-5}, \quad (61)$$

where s_L and s_T are the longitudinal and transverse sound velocities. ρ is the mass density and ϕ is the anharmonicity parameter. With $s_L = 2900 \text{ m s}^{-1}$, $s_L/s_T \approx 2$, $v = 40 \text{ cm}^{-1} \cdot 3 \cdot 10^{10} \text{ cm s}^{-1} = 1.2 \text{ THz}$ and $\rho = 0.762 \text{ g cm}^{-3}$, we obtain $\tau_{dec} \approx 10 \div 200 \text{ ns}$. We are now able to write $n_{NQP}(\omega) = N\omega^{-5}$. The normalization constant N can be obtained by equating the total pumping and the energy release integrated over all modes

$$\dot{Q} = \int_{\omega_c}^{\omega_D} n_{NQP}(\omega) \tau_{dec}(\omega) \rho_\omega \hbar \omega d\omega, \quad (62)$$

where $\rho_\omega = 9N_M\omega_D^{-3}\omega^2$ denotes the density of phonon states, here considered for one molecule, $N_M = 1$. We obtain $n_{NQP}(\omega_c) = 0.001 \div 0.01$. These estimates are presumably lower limits because of the above assumptions concerning the pumping and single generation. We thus take $n_{NQP}(\omega_c) = 0.01$ as our estimate. This value is large if compared with the corresponding values at thermal conditions. A temperature of $T \approx 11 \text{ K}$ is required for $n_{NQP}(\omega_c) = 0.01$ by thermal activation which demonstrates that NQPs may give rise to strong effects. The phonon occupation $n_{NQP}(\omega_c) = 0.01$ is small if compared with the limit required to establish a hot spot¹ in the sense of Levinson [101, 103, 104].

1. A hot spot is a region where NQPs are self locked because of a very small mean-free scattering path caused by inter-phonon collisions. The hot spot can be generated when the phonon-occupation numbers are larger than one.

Therefore a hot spot is unlikely to be generated. Nevertheless, phonon coalescence is likely to take place at $\omega > \omega_c$ which further increases the NQP density in this frequency regime.

We estimate the frequency shift due to the non-equilibrium conditions by adopting the principle of equipartition of energy between resonant states. For a local mode with frequency $\omega_{LP} \approx \omega_c$, the detailed balance is $k_u \tau = n_{NQP}(\omega_c) \approx 0.01$. Using the average β_v of Table I, we obtain from Eq. (54) $\delta v \approx -250$ MHz. With regard to the uncertainties in the derivation, the estimated shift is in reasonable agreement with the observed values of 160-320 MHz at 400 mW.

The broadening induced by NQPs is estimated from the scaling law $\tau \propto \omega_{LP}^{-2}$ [89], which shows that the motional narrowing becomes more effective with increasing local mode frequency. At $\omega_{LP} \approx \omega_c$ we calculate a width-to-shift ratio of $|\delta\Gamma/\delta v| \approx 0.1$, compatible with the data of TPE. Although we are not able to provide accurate estimates, we conclude that the observed line widths and shifts can, again without contradiction, be explained solely by NQPs.

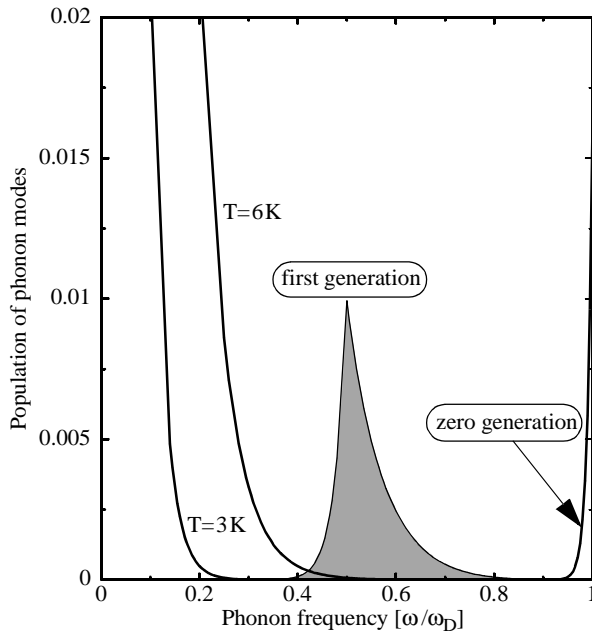


Fig. 25 Populations of phonon modes of zero generation (right side) and first generation (center) inside the laser pumped volume. The first generation modes are calculated according to $n_{NQP} \propto \omega^{-4}(\omega_D - \omega)^2$ if $\omega > 0.5 \cdot \omega_D$ and $n_{NQP} \propto \omega^{11/2}$ if $\omega < 0.5 \cdot \omega_D$. See Appendix for more details. Populations of phonons modes in the thermal equilibrium at $T = 3$ K and $T = 6$ K are shown for comparison.

The bottleneck model predicts the relative population of phonon modes shown in Fig. 25. The essential feature of this prediction is a peak in the phonon density at $\omega \approx \omega_c$. To justify the choice of $\omega_c \approx 35$ cm^{-1} we should estimate the phonon diffusion length at ω_c . To make this estimate the mean-free path is needed, a quantity difficult to determine because it depends on lattice imperfections and umklapp processes [105, 106, 107].

There are no data available for TD; we thus consider other organic solids.

Interestingly, very low values for the heat conductivity are found while the

sound velocities show a regular behavior which indicates that there are small mean-free

paths in these solids. For instance for naphthalene at the relevant temperature of $T \approx \hbar \omega_c / (3k_B) \approx 17$ K [105], the heat conductivity is $\kappa = \frac{1}{3} C s l \approx 5 \text{ Wm}^{-1} \text{K}^{-1} \text{s}^{-1}$ [108] and the heat capacity per unit volume is $C = 4.5 \times 10^4 \text{ J m}^{-3} \text{K}^{-1}$ [109]. With the sound velocity of $s \approx 2900 \text{ m s}^{-1}$ [110], we calculate a mean free path of $l \approx 0.1 \mu\text{m}$. Taking this value for the mean-free path l of TD at ω_c we estimate a scattering time of $\tau_{scat} = 30$ ps. This result obtained on the basis of the data for naphthalene are consistent with values determined for anthracene [111] and polyethylene [112, 113, 114]. The scattering time τ_{scat} is much smaller than the corresponding phonon lifetime τ_{dec} of 10-100 ns. Thus the equipartition of energies between NQPs and local modes considered above is justified. With the estimated mean free path, the diffusion length is $L = \sqrt{l s \tau_{dec}} \approx 1 \div 5 \mu\text{m}$ which is of the order of the spot size. This result supports the choice of $\omega_c / (2\pi c) = 35 \text{ cm}^{-1}$ as the critical frequency.

Appendix A

The absorbed energy is quickly released into acoustic zero generation phonons with $\omega_{zg} \approx \omega_D$. Every such phonon decays into two phonons with frequencies ω and ω' . The probability to decay in particular modes is proportional to $\omega_{zg} \omega \omega'$ [101]. The population rate of a particular mode with frequency ω is equal to

$$\mathfrak{R} = \mathfrak{N} \omega (\omega_D - \omega), \quad (63)$$

where \mathfrak{N} is the normalization constant and the energy conservation is taken into account.

One should consider also the momentum conservation $\vec{k}_\omega + \vec{k}_{\omega'} = \vec{k}_{\omega_D}$. For that we need a specific for every material dispersion law. \mathfrak{N} can be determined from the expression

$$\dot{Q} = \int_{\omega_D/2}^{\omega_D} \mathfrak{R} \hbar \omega_D \omega d\omega = \mathfrak{N} \int_0^{\omega_D} \hbar \omega_D \omega^2 (\omega_D - \omega) d\omega, \quad (64)$$

where $\rho_\omega = 9 N_M \omega_D^{-3} \omega^2$ denotes the density of phonon states, here considered for one molecule, $N_M = 1$ (remember that \dot{Q} is the energy release per molecule).

$$\aleph = \dot{Q}\omega_D^2 / \left(9\hbar \int_{\omega_D/2}^{\omega_D} \omega^3 (\omega_D - \omega)^3 d\omega \right) \quad (65)$$

The integral can be easily evaluated

$$\begin{aligned} \int_{\omega_D/2}^{\omega_D} \omega^3 (\omega_D - \omega)^3 d\omega &= \int_{\omega_D/2}^{\omega_D} (\omega_D^3 \omega^4 - 3\omega_D^2 \omega^5 + 3\omega_D \omega^6 - \omega^7) d\omega \\ &= \left(\frac{\omega_D^3 \omega^5}{5} - \frac{3\omega_D^2 \omega^6}{6} + \frac{3\omega_D \omega^7}{7} - \frac{\omega^8}{8} \right) \Bigg|_{\omega_D/2}^{\omega_D} = \frac{\omega_D^7}{280} \end{aligned} \quad (66)$$

Assuming that the second generation of phonons will have frequency smaller than ω_c and escape from the laser spot we consider only first generation and estimate the phonon occupancy by $n_{NQP} = \aleph \tau_{dec}$. If $\omega_{ph} > \omega_c$, phonons do not escape from the excited volume. And we obtain for NQP with $\omega > \omega_c$

$$n_{NQP}(\omega) = \frac{280\dot{Q}}{9\hbar\omega_D} \cdot \frac{\omega(\omega_D - \omega)^3}{\omega_D^4} \tau_{dec}. \quad (67)$$

If $\omega_{ph} < \omega_c$, n_{NQP} given by Eq. (67) should be multiplied the extra factor $(\omega / \omega_c)^{27/2}$ which takes into account the increase of the diffusional volume. Thus,

$$n_{NQP}(\omega) = \frac{280\dot{Q}}{9\hbar\omega_D} \cdot \frac{\omega(\omega_D - \omega)^3}{\omega_D^4} \tau_{dec} \cdot \left(\frac{\omega}{\omega_c} \right)^{27/2}. \quad (68)$$

This gives a scaling

$$n_{NQP}(\omega) \propto (\omega_D - \omega)^3 \cdot \omega^{19/2}. \quad (69)$$

At $\omega = 0.5\omega_D$ and with all the numbers at hand

$$n_{NQP} = \frac{280\dot{Q}}{9\hbar\omega_D} \cdot \frac{\tau_{dec}}{16} = \frac{280 \cdot 3 \times 10^7 \text{ cm}^{-1} \text{ s}^{-1}}{9 \cdot 80 \text{ cm}^{-1}} \cdot \frac{(10^{-8} \div 10^{-7}) \text{ s}}{16} = 0.007 \div 0.07 \quad (70)$$

This result justifies the estimate $n_{NQP} \approx 0.01$ at $\omega \approx 0.5 \cdot \omega_D$.

V. Non-Lorentzian Line Shapes

A text book representation of the resonance line shape by a Lorentzian with three parameters — width, amplitude, and center frequency — has been revised using single terrylene molecules in a naphthalene crystal; a very stable system where the line shape function can be measured very precisely. In solids, the line shape function is obscured by a variety of inhomogeneities and scattering. Inhomogeneities that arise in solids can only be partially eliminated by spectral hole burning or photon echo techniques [31, 115]. Single-molecule spectroscopy automatically eliminates all inhomogeneities and simplifies the analysis. The absence of inhomogeneity and the extremely high signal to background ratio (up to 700:1 in this case) made it possible to study the core region of the

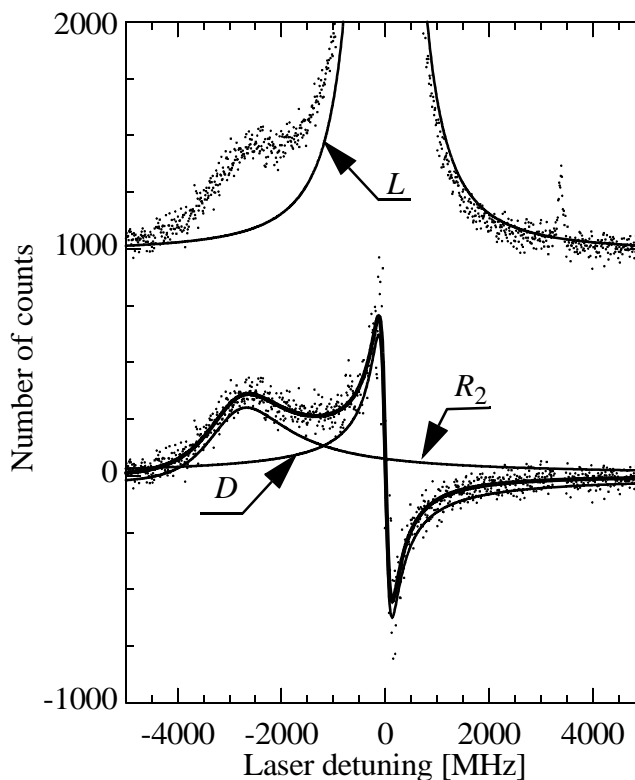


Fig. 26 The upper part shows a zoom into the low count region (the line peak reaches 42000 counts) of a single-molecule fluorescence excitation spectrum recorded at 2.1 K with an excitation power of 1.2 μ W. The weak and narrow line to the right of the main line corresponds to another molecule. Below, the deviation of the measured line shape from the Lorentzian (L) shows the dispersive-like behavior. The larger deviation on the left side is caused by a weak and broad satellite line $R_2(\omega)$. The function $R(\omega)$ was fitted to the data. L is the purely Lorentzian part of the fit function and the unlabeled thick line is the difference between the fit and the Lorentzian part. For the sake of clarity, this difference was decomposed into the dispersive component D and the satellite line $R_2(\omega)$

line as well as its wings. The measured spectrum is displayed in Fig. 26. A broad and weak shoulder to the left of the main line and a dispersive contribution in the core region are clearly visible.

A higher excitation power has to be used to keep the shot noise in the low count region small and hence saturation effects should be considered. But in linear response theory (like that which has led to Eqs. (2-56)) it is difficult to take saturation effects into account

properly. A more general approach where the saturation effects can be easily included is based on a master equation derived from a microscopic Hamiltonian using Redfield relaxation theory [116]. The master equation has been derived by de Bree and Wiersma for systems of our kind [117]. Although the equations are complex, they can be solved and a simplified solution for the line shape function consists of a sum of two contributions $R_1(\omega)$ and $R_2(\omega)$ which read [118]

$$R_1(\omega) = \left(1 - \left[(\Gamma_0 - \gamma) \Gamma_{3434}^{-1} - \Phi \frac{\Gamma_{34}}{\Delta} \right] \right) \frac{\Gamma_0 + \Phi(\omega - \omega_0)}{\Gamma^2 + (\omega - \omega_0 - \delta_\omega)^2} \quad (71)$$

and

$$R_2(\omega) = \frac{\left[(\Gamma_0 - \gamma) - \Phi \frac{\Gamma_{3434}^2}{\Delta} \right] - \Phi(\omega - \Delta - \omega_0)}{\Gamma_{3434}^2 + (\omega - \Delta - \omega_0)^2}, \quad (72)$$

where

$$\Gamma_0 = \gamma + \Gamma_\tau \left(1 - \frac{|\Gamma_{3412}|^2}{\Delta^2 + \Gamma_{3434}^2} \right) \cdot \exp\left(-\frac{E}{k_B T}\right), \quad (73)$$

$$\delta_\omega = \frac{\Delta |\Gamma_{3412}|^2}{\Delta^2 + \Gamma_{3434}^2} \cdot \exp\left(-\frac{E}{k_B T}\right), \quad (74)$$

and

$$\Phi = \left(\frac{2\Delta \cdot \text{Re}[\Gamma_{3412}]}{\Gamma_{3434}^2 + \Delta^2} - \frac{2\Delta \Gamma_{3434} |\Gamma_{3412}|^2}{(\Delta^2 + \Gamma_{3434}^2)^2} \right) \cdot \exp\left(-\frac{E}{k_B T}\right). \quad (75)$$

Γ is the parameter which takes into account the saturation effect. At low laser power $\Gamma = \Gamma_0$. The coefficient Γ_{3434} determines the coherence decay rate which can be interpreted as a loss of coherence owing to stochastic phase diffusion caused by statistical fluctuations of the transition frequency. Γ_{3412} is the coherence transfer term which does not have an obvious classical analogy. The reason for using such indices will become clear in the next section where a detailed theory is presented.

For low laser intensity a similar set of equations can be derived using the sudden jump model if the equations are solved with the condition $\Delta \geq k_d$ (k_d is the decay rate of the ex-

cited state of a single TLS interacting with a probe molecule). But while the sudden jump model has only three parameters, E , Δ , and k_d , a more rigorous theory of relaxations has five parameters E , Δ , Γ_{3434} , and Γ_{3412} (Γ_{3412} is a complex number).

The energy E enters in both theories through a Boltzmann coefficient $\exp(-E/(k_B T))$ and can be determined from a temperature dependence of the line shape (see Fig. 27). An interesting question is how these two theories are related, especially keeping in mind that the sudden jump model is an intuitively very appealing approach rather than a rigorous theory. If the line shape function is approximated by a Lorentzian, then its parameters (if measured at two temperatures) can be used to determine the three parameters of the model and thus phenomenologically the sudden jump model and the relaxation theory are equally

applicable. If the side band and the amplitude of the dispersive contribution are also taken into account then all five coefficients can be determined. Of course the validity of a three-parameter model would imply that there are at least two relations between apparently independent parameters. Thus a precise measurement of the single-molecule line shape will either display limitations of the sudden jump approach or will reveal new physics which restricts the number of independent coefficients. Theoretical consideration shows that the line shapes predicted with the two approaches are different if the vibrational-phonon coupling depends on the electronic wave functions, but the difference, however, can only be inferred if the amplitude of the dispersive contribution is measured in addition to the line width and frequency. Since the master equation approach is not limited to low laser powers, it was used to show that under strong laser excitation the line behaves in a fashion intermediate to the homogeneously and inhomogeneously broadened lines.

The actual data were fitted with Eqs. (71-75) with an accuracy defined by the quantum noise of the measured signal. Because of laser drift, the temperature frequency shift δ_ω

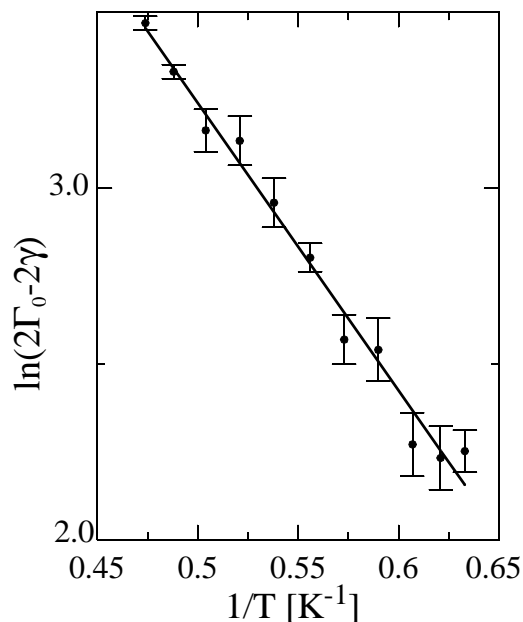


Fig. 27 A temperature dependence of the main peak linewidth Γ . The life-time limited linewidth $2\gamma/(2\pi) = 43$ MHz. The slope is $8.2(4)$ K and the intercept $7.3(2)$.

was always included when fitting the data. The temperature dependence of the line shape was measured too. At a lower temperature, intensity shifts from the shoulder to the main line and the dispersive contribution and linewidth decrease. Unfortunately, the precision of the estimate of the vibrational energy E and the uncontrolled laser drift limit the accuracy of the determination of the complex parameter Γ_{3412} , and the question of whether the sudden jump model can adequately describe the line shape is still open but definitely deserves further investigation.

Details

When the shape of a resonance line of a single molecule interacting with a single pseudo localized vibration (PLV) is measured with high accuracy, these measurements clearly show that the line shape is more complicated than a simple Lorentzian having essentially only two parameters, the width (FWHM) and the central frequency.

The data are analyzed in terms of the reduced density matrix $\rho_S \equiv \text{Tr}_B\{\rho\}$, which describes a small system interacting with an unobservable bath. The partial trace is taken over the bath states and ρ is a density matrix of the whole system which may include, for example, a probe molecule and the matrix in which the molecule is imbedded. The evolution of ρ_S is described by a master equation (ME) [75], which in the absence of the external fields reads

$$\dot{\rho}_{smn} = \sum_{ij} \Gamma_{ijmn} \rho_{Sij}. \quad (76)$$

The coefficients Γ_{ijmn} are time independent in the secular approximation [75]. Additional terms must be included to take into account an interaction between the molecule and classical fields. The spectral line intensity is then proportional to the steady-state response of the system to an electromagnetic field of a constant amplitude and frequency. The master equation and its steady-state solutions have been briefly discussed in the Overview but are considered in full detail in this section, including saturation effects at high laser power.

A different approach, the sudden jump model (SJM), is widely used for calculations of line shapes [66 - 72, 76 - 80, 119, 120] at low laser intensities. The SJM is a way to circumvent the complicated ME. The line shape function is expressed as

$$R(\omega) \propto \text{Re} \left[\int_0^{\infty} e^{-i\omega t} \left\langle e^{i \int_0^t \omega(\tau) d\tau} \right\rangle dt \right], \quad (77)$$

where $\langle \rangle$ denotes an average over all realizations of the time dependent stochastic transition frequency $\omega(\tau)$, whose choice is motivated by physical intuition and mathematical convenience [85].

In its simplest version (corresponding to a two-level single molecule interacting with a PLV) the SJM has only three parameters — the energy of the pseudo-local vibration ε , the single molecule transition frequency change upon excitation of that vibration ϑ , and the life time of the PLV τ . For the same model system, the more involved theory based on the ME has four parameters, one of which is a complex number [118]. The energy of the PLV ε (or more precisely E , the PLV energy modified by the interaction with the electronic states) enters both theories through a Boltzmann factor $B = \exp(-E/k_B T)$ and can be determined from the temperature dependence of the line shape. An interesting question is how these two theories are related. If the line shape function can be described by only two parameters then there must be at least two relations between four apparently independent real constants in the master equation. Thus a precise measurement of the single-molecule line shape should either display limitations of the SJM or reveal new physics restricting the number of independent coefficients in the master equation. These qualitative arguments are analyzed in the next section along with the detailed description of the two approaches.

The sudden jump model and the master equation

In general, at low laser power the absorption spectrum of a quantum-mechanical system is proportional to a Fourier integral of the correlation function of the transition dipole moment operator in the Heisenberg representation $\hat{\mu}(t)$ as given below

$$R(\omega) \propto \text{Re} \left[\int_0^{\infty} \text{Tr} \{ \rho \hat{\mu}_0 \hat{\mu}(\tau) \} e^{-i\omega\tau} d\tau \right], \quad (78)$$

where $\hat{\mu}_0 = \hat{\mu}(0)$. Original arguments justifying Eq. (78) and their more rigorous version can be found in the literature [85, 121 - 123]. Thus the key quantity for the calculation of the spectral line shape is the correlation function

$$\phi(\tau) = \text{Tr}\{\rho\hat{\mu}_0\hat{\mu}(\tau)\}. \quad (79)$$

In this paper the system of interest has a Hamiltonian \hat{H} which is assumed to consist of the following parts.

$$\hat{H} = \hat{H}_e + \hat{H}_v + \hat{H}_{e-v} + \hat{H}_b + \hat{H}_{b-v}, \quad (80)$$

where the PLV Hamiltonian \hat{H}_v , the thermal bath Hamiltonian \hat{H}_b , and the bath-vibrational coupling \hat{H}_{b-v} are independent of electronic degrees of freedom. \hat{H}_e is the two-level molecular Hamiltonian and \hat{H}_{e-v} describes the interaction between the molecular states and the PLV. The system is shown schematically in Fig. 28. We also define a small system

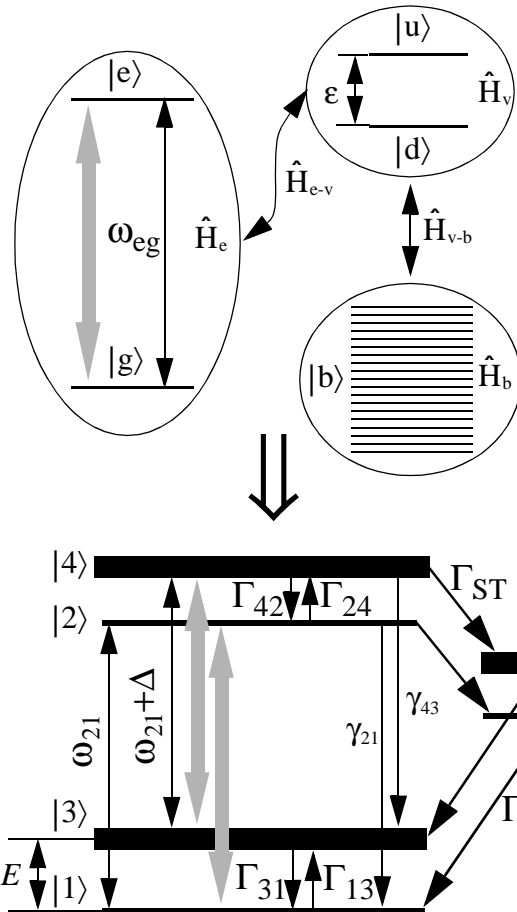


Fig. 28 The energy levels of the three unperturbed systems represented by the Hamiltonians \hat{H}_e , \hat{H}_v and \hat{H}_b are shown on the left side of the figure. The interaction Hamiltonians are also shown there. On the right side the two systems \hat{H}_e and \hat{H}_v are combined in a four level system (small system) in which the interaction \hat{H}_{e-v} is taken into account. The grey arrows connect levels with a non zero transition dipole moment. The acoustic-phonon system \hat{H}_b serves as a thermalized reservoir. The interaction between the small system and the acoustic phonons is assumed to be small and can be treated using a perturbation approach (up to the second order). This leads to a master equation for a reduced density matrix of the small system. A different approach is based on a classical trajectory assigned to the optical transition frequency. The triplet states $|5\rangle$ and $|6\rangle$ are also shown. Coefficients Γ_{ij} are denoted by Γ_{ij} for brevity.

Hamiltonian $\hat{H}_{ss} = \hat{H}_e + \hat{H}_v + \hat{H}_{e-v}$. As basis vectors we use direct products of the Eigenstates $|m\rangle$ of \hat{H}_{ss} , where $m = \{1, 2, 3, 4\}$, and the Eigenstates of \hat{H}_b which are the

phonon modes $|b\rangle \equiv |\xi\rangle \equiv |v\rangle$. We consider only two states of the PLV because at low temperatures ($k_B T \ll E$) the PLV can be considered as a two-level system (TLS). The main idea of the SJM is to assign a classical “trajectory” to the dipole moment, that is, to replace $\hat{\mu}(t)$ by a random function of time which behaves according to classical probability laws. In this case the ensemble averaging $\text{Tr}\{\rho\hat{\mu}_0\hat{\mu}(\tau)\}$ can be replaced by an averaging of $\langle\mu_0\mu(\tau)\rangle$ over all possible “trajectories” where a classical stochastic function $\mu(\tau) \equiv \mu_0 \exp[i\int_0^\tau \omega(\tau)d\tau]$ is used. Such an approximation leads to Eq. (77). For stochastic Markovian trajectories, the correlation function can be expressed in the following way

$$\phi(\tau) = \rho_{S_{11}}(0) \cdot (Q_{dd} + Q_{du}) + \rho_{S_{33}}(0) \cdot (Q_{ud} + Q_{uu}) \quad . \quad (81)$$

where $\rho_{S_{11}}(0)$ and $\rho_{S_{33}}(0)$ are the probabilities that at time zero the PVL is in the state “down” and “up” respectively. Q_{dd} and Q_{du} are the correlation functions averaged over trajectories starting when the TLS is in its “down” state at time zero and ending in its “down” or “up” state at time τ respectively. $Q_{dd} + Q_{du}$ is obviously an average over all trajectories starting with the TLS state “down”. Q_{ud} , Q_{uu} , and $Q_{ud} + Q_{uu}$ have similar meanings but when the initial state is the state “up”. Thus the right side of Eq. (81) is the Boltzmann weighted average over the two classes of trajectories. The Q functions are the solutions of two coupled equations [77, 79]

$$\dot{Q}_{xd} = -k_u Q_{xd} + k_d Q_{xu}, \quad (82)$$

$$\dot{Q}_{xu} = k_u Q_{xd} - (k_d - i\mathcal{D})Q_{xu}, \quad (83)$$

with the initial conditions $\{Q_{dd}(0), Q_{du}(0)\} = \{1, 0\}$ and $\{Q_{ud}(0), Q_{uu}(0)\} = \{0, 1\}$.

Alternatively to this intuitive approach, one may evaluate the trace in Eq. (78)

$$\begin{aligned} \text{Tr}\{\rho\hat{\mu}_0\hat{\mu}(\tau)\} &= \text{Tr}\{\rho\hat{\mu}_0 e^{-i\hat{H}\tau/\hbar} \hat{\mu}_0 e^{i\hat{H}\tau/\hbar}\} = \text{Tr}\{e^{i\hat{H}\tau/\hbar} \rho\hat{\mu}_0 e^{-i\hat{H}\tau/\hbar} \hat{\mu}_0\} \\ &= \text{Tr}_S\{\text{Tr}_B\{e^{i\hat{H}\tau/\hbar} \rho\hat{\mu}_0 e^{-i\hat{H}\tau/\hbar}\} \hat{\mu}_0\} \end{aligned} \quad (84)$$

and see that $e^{i\hat{H}\tau/\hbar} \rho\hat{\mu}_0 e^{-i\hat{H}\tau/\hbar}$ obeys equations of motion formally analogous to those for ρ , namely, $-i\hbar\dot{\rho} = [\hat{H}, \rho]$, and thus the matrix elements of the operator $\hat{P}(\tau) \equiv \text{Tr}_B\{e^{i\hat{H}\tau/\hbar} \rho\hat{\mu}_0 e^{-i\hat{H}\tau/\hbar}\}$ obey the equations of motion for the corresponding matrix

elements of the reduced density matrix. The initial conditions $\hat{P}(0) \equiv \text{Tr}_B\{\rho(0)\hat{\mu}_0\} \equiv \rho_s(0)\hat{\mu}_c$ can be evaluated for the approximately diagonal form of the reduced density matrix of the small system in thermal equilibrium. In the optical domain, only the ground electronic state is significantly populated, which approximately holds at low laser powers, and the density matrix has zero off-diagonal elements. Thus

$$\rho_s(0) = \rho_{s_{11}}(0) \cdot |1\rangle\langle 1| + \rho_{s_{33}}(0) \cdot |3\rangle\langle 3| \quad .$$

The dipole moment operator at $t = 0$ acts only on the variables of the small system and reads

$$\hat{\mu}_0 = \mu|1\rangle\langle 2| + \mu^*|2\rangle\langle 1| + \mu|3\rangle\langle 4| + \mu^*|4\rangle\langle 3| \quad (85)$$

Hence $\hat{P}(0) = \rho_{s_{11}}(0) \cdot |1\rangle\langle 2| + \rho_{s_{33}}(0) \cdot |3\rangle\langle 4|$, where for brevity we assume that $\mu = 1$. The correlation function expressed by means of the matrix elements of \hat{P} reads

$$\phi(\tau) = \sum_m \langle m|P(\tau)\hat{\mu}_0|m\rangle = P_{12}(\tau) + P_{21}(\tau) + P_{34}(\tau) + P_{43}(\tau) \quad . \quad (86)$$

Taking into account that the homogeneous equations (76) for $P_{21}(\tau)$ and $P_{43}(\tau)$ are formally uncoupled from $P_{12}(\tau)$ and $P_{34}(\tau)$ and considering the initial conditions $P_{21}(\tau) = P_{43}(\tau) = 0$ we obtain $P_{43}(\tau) \equiv P_{21}(\tau) \equiv 0$. Thus the final result simplifies to

$$\phi(\tau) = P_{12}(\tau) + P_{21}(\tau) \quad , \quad (87)$$

where

$$\dot{P}_{mn} = \sum_{ij} \Gamma_{ijmn} P_{ij} \quad (88)$$

The coefficients Γ_{ijmn} are the coefficients of the ME and the initial conditions are $\{P_{12}(0), P_{34}(0)\} = \{\rho_{s_{11}}(0), \rho_{s_{33}}(0)\}$.

The method of obtaining the master equation and can be found in text books [75] or elsewhere in the literature [124, 125]. We take the interaction Hamiltonian to be of the form $\hat{H}_{b-v} = \hat{B} \cdot \hat{V}$ where the operator \hat{B} acts only on the phonon bath states and \hat{V} acts only on the small system states. In the secular approximation, the master equation reads

$$\dot{\rho}_{11} = \Omega \text{Im}[\rho_{12} e^{-i\omega t}] - \Gamma_{13} \rho_{11} + 2\gamma_0 \rho_{22} + \Gamma_{31} \rho_{33} + \Gamma_{TS}^d \rho_{55} \quad , \quad (89)$$

$$\dot{\rho}_{22} = -\Omega \text{Im}[\rho_{12} e^{-i\omega t}] - (\Gamma_{24} + 2\gamma_0 + \Gamma_{ST}^d) \rho_{22} + \Gamma_{42} \rho_{44}, \quad (90)$$

$$\dot{\rho}_{44} = -\Omega \text{Im}[\rho_{34} e^{-i\omega t}] + \Gamma_{24} \rho_{22} - (2\gamma_0 + \Gamma_{42} + \Gamma_{ST}^u) \rho_{44}, \quad (91)$$

$$\dot{\rho}_{55} = \Gamma_{ST}^d \rho_{22} - \Gamma_{TS}^d \rho_{55} - \Gamma_{56} \rho_{55} + \Gamma_{65} \rho_{66}, \quad (92)$$

$$\dot{\rho}_{66} = \Gamma_{ST}^u \rho_{44} - \Gamma_{TS}^u \rho_{66} + \Gamma_{56} \rho_{55} - \Gamma_{65} \rho_{66}, \quad (93)$$

$$\rho_{11} + \rho_{22} + \rho_{33} + \rho_{44} + \rho_{55} + \rho_{66} = 1, \quad (94)$$

$$\dot{\rho}_{12} = \frac{i}{2} \Omega e^{i\omega t} (\rho_{22} - \rho_{11}) - \left(\Gamma_{1212} + \gamma_0 + \frac{\Gamma_{ST}^d}{2} \right) \rho_{12} + \Gamma_{3412} \rho_{34}, \quad (95)$$

$$\dot{\rho}_{34} = \frac{i}{2} \Omega e^{i\omega t} (\rho_{44} - \rho_{33}) + \Gamma_{1234} \rho_{12} - \left(\Gamma_{3434} + \gamma_0 + \frac{\Gamma_{ST}^u}{2} - i\Delta \right) \rho_{34}, \quad (96)$$

where ω is the laser frequency and the coefficients Γ_{ijj} are denoted by Γ_{ij} . The subscript S of the reduced density matrix is omitted and in Eqs. (95, 96) the transition frequency $\omega_{21} = 0$ for brevity. The coupling to the electromagnetic field taken in the dipole approximation and connecting only different electronic states is described by the Rabi frequency Ω . By substituting $\rho_{12} = \tilde{\rho}_{12} \exp(i\omega t)$ and $\rho_{34} = \tilde{\rho}_{34} \exp(i\omega t)$ the time dependent exponential functions can be eliminated. Keeping in mind the treatment of optical saturation effects, two triplet states $|5\rangle$ and $|6\rangle$ (with the PLV state “down” and “up”, respectively) are included to take into account the triplet bottle-neck, which is important at high laser powers [126]. We assume that $\gamma_{21} = \gamma_{43} = 2\gamma_0$, $\gamma_{41} = \gamma_{23} = 0$ (see Fig. 28). Latter on the rates of triplet state depopulation $\Gamma_{TS}^d = \Gamma_{TS}^u = \Gamma_{TS}$ and intersystem crossing are considered to be independent of the PLV state, that is $\Gamma_{TS}^d = \Gamma_{TS}^u = \Gamma_{TS}$ and $\Gamma_{ST}^d = \Gamma_{ST}^u = \Gamma_{ST}$. A notation $2\gamma = 2\gamma_0 + \Gamma_{ST}$ will be used for a brevity. The important relaxation coefficients are [124]

$$\Gamma_{3412} = \frac{\pi}{\hbar} \sum_{v, \xi} \rho_{B_{\xi\xi}} \langle 1, v | \hat{H}_{b-v} | 3, \xi \rangle \langle 4, \xi | \hat{H}_{b-v} | 2, v \rangle \times [\delta(E_{\xi} + E_3 - E_v - E_1) + \delta(E_4 + E_{\xi} - E_2 - E_v)] \quad (97)$$

$$\begin{aligned} \Gamma_{3434} = & \frac{\pi}{\hbar} \sum_{\nu, \xi} \rho_{B_{\xi\xi}} |\langle 1, \nu | \hat{H}_{b-\nu} | 3, \xi \rangle|^2 \delta(E_\xi + E_3 - E_\nu - E_1) \\ & + \frac{\pi}{\hbar} \sum_{\nu, \xi} \rho_{B_{\xi\xi}} |\langle 2, \nu | \hat{H}_{b-\nu} | 4, \xi \rangle|^2 \delta(E_4 + E_\xi - E_2 - E_\nu) \end{aligned} \quad (98)$$

In Eq. (98) the adiabatic part is neglected. $\rho_{B_{\xi\xi}}$ stands for the bath phonon density matrix and the summation is performed over the bath phonon states. $|m, \nu\rangle$ and $|m, \xi\rangle$ are the tensor products $|m\rangle \otimes |\nu\rangle$ and $|m\rangle \otimes |\xi\rangle$ respectively. The coefficients $\Gamma_{3412}, \Gamma_{1234}$ are complex numbers. All other coefficients are real. We perform the following interchanges $1 \rightleftharpoons 3, 2 \rightleftharpoons 4, \nu \rightleftharpoons \xi$, replace $\rho_{B_{\nu\nu}}$ by $\rho_{B_{\xi\xi}} \exp[-(E_\xi - E_\nu) / (k_B T)]$, and assume that $\Delta \ll k_B T$ to obtain $\Gamma_{1234} = B\Gamma_{3412}^*$ and $\Gamma_{1212} = B\Gamma_{3434}$.

The applicability of the master equations is limited to weak and intermediate optical fields. In the case of strong fields these equations should be modified. Various approximations that have been discussed in the literature [128 - 131] concern a two-level atomic system interacting with a heat bath. In this paper we deal with a four-level system where all the levels are treated on equally. As in the case of two levels, the validity of Eqs. (89-96) is limited by the conditions $\Omega \ll \tau_{cor}^{-1}$ and $\Gamma \ll \tau_{cor}^{-1}$ for all Γ , where τ_{cor} is the correlation time of the phonon bath which is on the order of $1/\omega_D$, where ω_D is the Debye phonon frequency. An additional limitation is that the frequency difference Δ caused by the coupling between PLV and electronic states, should be larger than Ω . The opposite case corresponds to a PLV interacting with dressed electronic states [75]. All of these conditions are fulfilled in the numerical examples given below.

From Eqs. (88, 95, 96) it follows that

$$\dot{P}_{12} = -(\Gamma_{1212} + \gamma)P_{12} + \Gamma_{3412}P_{34} \quad (99)$$

and

$$\dot{P}_{34} = \Gamma_{1234}P_{12} - (\Gamma_{3434} + \gamma - i\Delta)P_{34} . \quad (100)$$

Substituting $P_{12} = \tilde{P}_{12}(t)\exp(-\gamma t)$ and $P_{34} = \tilde{P}_{34}(t)\exp(-\gamma t)$ into Eqs. (99, 100) lead to Eqs. (82, 83) if the equalities $\Gamma_{1212} = \Gamma_{1234} = k_u$, $\Gamma_{3412} = \Gamma_{3434} = k_d$, $\Delta = \vartheta$

hold and with the correspondences $Q_{xd} \leftrightarrow \tilde{P}_{12}$ and $Q_{xu} \leftrightarrow \tilde{P}_{34}$. These equalities are valid if (see Eqs. (97, 98))

$$\langle 1, v | \hat{H}_{b-v} | 3, \xi \rangle = \langle 2, v | \hat{H}_{b-v} | 4, \xi \rangle \quad . \quad (101)$$

The electron-vibrational coupling \hat{H}_{e-v} is weak and hence $|1\rangle \approx |g\rangle \otimes |d\rangle$, $|2\rangle \approx |e\rangle \otimes |d\rangle$, $|3\rangle \approx |g\rangle \otimes |u\rangle$, and $|4\rangle \approx |e\rangle \otimes |u\rangle$. With this approximation, Eq. (101) holds when the coupling between the PLV and phonon bath (\hat{H}_{b-v}) is independent of the electronic degrees of freedom. This conclusion (although obtained in a different way) agrees with other authors [124, 127].

Solution of the master equation

When the system is excited by a harmonic electromagnetic field, the excitation spectrum is proportional to the steady-state spontaneous emission and hence to the population of the electronically excited singlet states $n_e \equiv \rho_{22}(\infty) + \rho_{44}(\infty) \propto \tilde{\rho}_{12}(\infty) + \tilde{\rho}_{34}(\infty)$ (see Eqs. (120, 121)). The steady-state expression for n_e reads (see Appendix)

$$n_e = \frac{\frac{\Omega^2}{4\gamma} \left(\text{Re} \left(\frac{(1-B)\{\Gamma_{34}^* + \Gamma_{1234} + i(\omega - \Delta)\} + (\Gamma_{12}^* + \Gamma_{3412} + i\omega)B}{N} \right) + B \left(\frac{2\gamma}{\Gamma_{13}} + \frac{2\gamma}{\Gamma_{24}} \right) \frac{\Omega^2}{4\gamma} \mathfrak{S} \right)}{1 + \frac{\Omega^2(2 + \Theta)}{4\gamma} \left(\text{Re} \left(\frac{(1-B)\{\Gamma_{34}^* + \Gamma_{1234} + i(\omega - \Delta)\} + (\Gamma_{12}^* + \Gamma_{3412} + i\omega)B}{N} \right) + B \left(\frac{2\gamma}{\Gamma_{13}} + \frac{2\gamma}{\Gamma_{24}} \right) \left(\frac{\Omega^2}{4\gamma} \mathfrak{S} + \wp \right) \right)} \quad (102)$$

where $N = (\Gamma_{12}^* + i\omega)(\Gamma_{34}^* - i\Delta + i\omega) - \Gamma_{1234}\Gamma_{3412}$. For brevity $\Gamma_{34}^* = \Gamma_{34} + \gamma$, $\Gamma_{12}^* = \Gamma_{12} + \gamma$, $\wp = -\frac{\omega}{2 + \Theta} \text{Im} \left[\frac{1}{N} \right]$ and $\mathfrak{S} = \text{Re} \left[\frac{\Gamma_{12}^* + i\omega}{N} \right] \text{Re} \left[\frac{\Gamma_{34}^* + i(\omega - \Delta)}{N} \right] - \text{Re} \left[\frac{\Gamma_{3412}}{N} \right] \text{Re} \left[\frac{\Gamma_{1234}}{N} \right]$. Additional simplifying approximations are $2\gamma \ll \Gamma_{42}$, $\Gamma_{ST}, \Gamma_{TS} \ll \Gamma_{65}$ and $\Gamma_{24}/K_{42} \approx \Gamma_{13}/K_{31} = B \ll 1$, where $K_{31} = \Gamma_{31} + \Gamma_{13}$ and $K_{42} = \Gamma_{42} + \Gamma_{24}$. If $\Omega^2 \ll 4\gamma\Gamma_0/(2 + \Theta)$, Eq. (102) reads

$$n_e = \Omega^2(R_1 + R_2)/(4\gamma), \quad (103)$$

where

$$R_1(\omega) = \frac{A_1\Gamma_0 + \Phi(\omega - \delta_\omega)}{(\omega - \delta_\omega)^2 + \Gamma_0^2}, \quad (104)$$

$$R_2(\omega) = \frac{\Gamma_{3434}A_2 - \Phi(\omega - \Delta)}{(\omega - \Delta)^2 + \Gamma_{3434}^2}, \quad (105)$$

$$A_2 = 1 - A_1 = \frac{\Gamma_0 - \gamma}{\Gamma_{3434}} - \Phi \frac{\Gamma_{3434}}{\Delta}, \quad (106)$$

$$\Gamma_0 = \gamma + \left(\Gamma_{3434} - \frac{\Gamma_{3434}|\Gamma_{3412}|^2}{\Delta^2 + \Gamma_{3434}^2} \right) B, \quad (107)$$

$$\delta_\omega = \frac{\Delta|\Gamma_{3412}|^2}{\Delta^2 + \Gamma_{3434}^2} B, \quad (108)$$

and

$$\Phi = \left(\frac{2\Delta \text{Re}[\Gamma_{3412}]}{\Delta^2 + \Gamma_{3434}^2} - \frac{2\Delta\Gamma_{3434}|\Gamma_{3412}|^2}{(\Delta^2 + \Gamma_{3434}^2)^2} \right) B. \quad (109)$$

Equations (103-109) represent the low-power approximation. It is interesting that the exponential temperature dependence in Eqs. (107, 108), frequently observed in experiments [17, 88, 132- 136], holds irrespective of the validity of the equality (101). Thus from an observation of an activation type dependence of linewidths and line frequencies, no definitive conclusion can be made about the applicability of the SJM. Only when these data are considered together with the dispersive prefactor Φ can an influence of the electronic states on the PLV-phonon coupling be revealed.

At high laser power the line saturates and changes its shape. Two extreme cases can be distinguished. In the first case the single complex line, Eq. (103), is split in two parts corresponding to the transitions $1 \rightarrow 2$ and $3 \rightarrow 4$ which then are treated independently. In this case the combined line is the sum of two lines with different weights.

$$n_e = A_1 \frac{\Omega^2 \sigma_1(\omega)}{4\gamma + (2 + \Theta)\Omega^2 \sigma_1(\omega)} + A_2 \frac{\Omega^2 \sigma_2(\omega)}{4\gamma + (2 + \Theta)\Omega^2 \sigma_2(\omega)} \quad (110)$$

where $R_1 + R_2 = A_1 \sigma_1 + A_2 \sigma_2$, assuming that A_1 and A_2 are proportional to the relative integrated intensities of the two lines and are subject to the normalization $A_1 + A_2 = 1$. It

is not clear what is the best way to split the total line shape $R_1 + R_2$. The simplest way to do it is

$$A_1\sigma_1 = R_1 \quad (111)$$

and

$$A_2\sigma_2 = R_2. \quad (112)$$

We will briefly return to this issue when we discuss the numerical example presented in Fig. 30.

Another extreme can be obtained by assuming that the low power line shape is not a sum of two independent lines but is a single line with a complex frequency dependence. In this case

$$n_e = \frac{\Omega^2 \sigma(\omega)}{4\gamma + (2 + \Theta)\Omega^2 \sigma(\omega)}, \quad (113)$$

where $\mathfrak{r}(\omega) = R_1(\omega) + R_2(\omega)$. Equations (110) and (113) describe the behavior of inhomogeneously and homogeneously broadened spectral lines in strong electromagnetic fields [137].

The transition from Eq. (110) to Eq. (113) is governed (see Eq. (126)) by the value of $2\gamma\text{Im}[\tilde{\rho}_{34}](\Gamma_{13}^{-1} + \Gamma_{24}^{-1})$ and the whole spectrum of intermediate situations is possible. If this factor can be neglected, Eq. (113) is valid. In Fig. 29 the line shape at high saturation is shown for the experimentally determined PLV parameters [118]. The deviation between (113) and (102) indicates that the line shape still has a “memory” about its origin from two different transitions. The applicability of Eq. (110) is more difficult to define. The problem is that the complex line shape can not be unambiguously split in two lines. The way it is done in Eq. (104) and (105) leads to nonphysical negative cross-sections at large detunings. In a special case when the dispersive contribution is zero (that is when $\text{Re}[\Gamma_{3412}] = \Gamma_{3434}|\Gamma_{3412}|^2/(\Delta^2 + \Gamma_{3434}^2)$), both lines are simple Lorentzians and the splitting does not lead to non physical results. The line shapes predicted by Eqs. (102), (110), and (113) are compared in Fig. 30, where it is clear that the exact solution (B) is situated between the two extremes.

At moderate powers when $4\gamma \gg (2 + \Theta)\Omega^2\sigma_2(\omega)$ the line shape is equally well described by both equations as a sum of the saturated main line and unsaturated side band (see Appendix. C).

$$n_e \propto \left(\frac{A_1\Gamma_0 + \Phi(\omega - \delta_\omega)}{(\omega - \delta_\omega)^2 + \Gamma_0^2[1 + I/I_{sat}]} + \frac{\Gamma_{3434}A_2 - \Phi(\omega - \Delta)}{(\omega - \Delta)^2 + \Gamma_{3434}^2} \right) \quad (114)$$

Usually the scaling factor in Eq. (114) is of no interest and the effect of saturation is reduced to the broadening of the main line which now has a linewidth $\Gamma = \Gamma_0\sqrt{1 + I/I_{sat}}$.

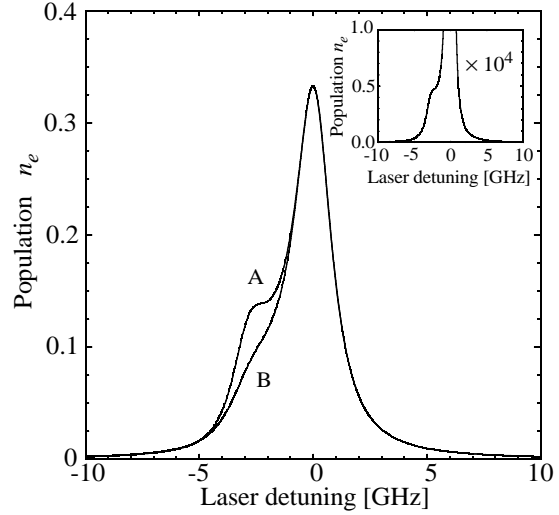


Fig. 29 (B) is the line shape function at high laser power calculated using the master equation formalism. The parameters of the model are $|\Gamma_{3434}|/(2\pi) = 0.918$ GHz, $|\Gamma_{3412}|/(2\pi) = 0.918$ GHz, $\text{Re}[\Gamma_{3412}]/(2\pi) = 0.918$ GHz, $\Delta/(2\pi) = 2.884$ GHz, $\gamma/(2\pi) = 0.0215$ GHz, $\Theta = 1$, and $\Omega/(2\gamma) = \sqrt{500}$. The inset shows the unsaturated line ($[\Omega/(2\gamma)]^2 = 0.1$) in the low count region. (A) is the line calculated assuming that the line shown in the inset is a single line with a complex shape (approximation of homogeneous broadening (Eq. (113))).

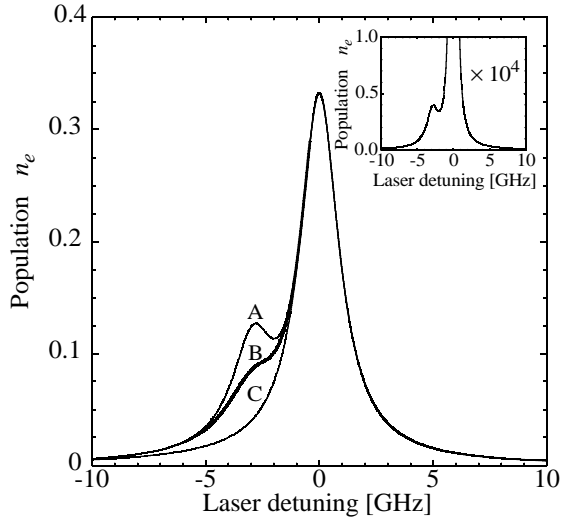


Fig. 30 The parameters are the same as in Fig. 29 but $\text{Re}[\Gamma_{3412}]/(2\pi) = 0.08$ GHz. This does not change anything but the amplitude of the dispersive contribution which is zero in this case. The inset shows the unsaturated line shape ($[\Omega/(2\gamma)]^2 = 0.1$) in the low count region. (A) and (C) are the lines calculated assuming approximations of homogeneous (Eq. (113)) and inhomogeneous Eq. ((110)) broadening, respectively.

The peak intensity of the main line is also a nonlinear function of laser intensity. This function can be written in the form $\mathfrak{R} = \mathfrak{R}_\infty / (1 + I_{sat}/I)$, where \mathfrak{R}_∞ is the peak count rate at $I \gg I_{sat}$. These relations which agree with the predictions of Eq. (4) can be checked more precisely if the laser intensity is excluded and the linewidth is expressed as a function of the count rate.

$$\frac{1}{\Gamma^2} = \frac{1}{\Gamma_0^2} - \frac{\mathfrak{R}}{\Gamma_0^2 \mathfrak{R}_\infty} \quad (115)$$

Experimental results are shown in Fig. 31. The straight line described by Eq. (115) is also shown for comparison.

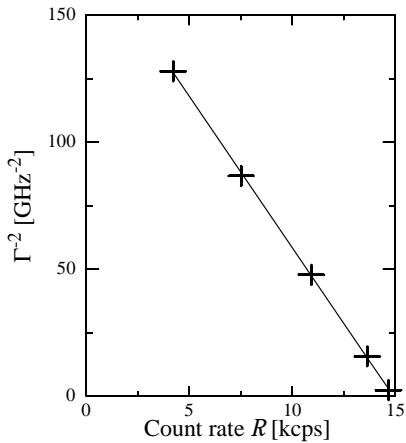


Fig. 31 The linewidth of the main line as a function of the peak count rate.

Conclusion

The electronic spectral line shape of a single molecule doped in a crystal has been studied in the framework of the master equation approach and the sudden jump model. In

the presence of a two-level system which interacts with the electronic transition (a pseudo local phonon at low temperatures is an example), the line shape consists of two Lorentzian distorted by the presence of dispersive components. Although both the master equation approach and the sudden jump model predict the presence of the dispersive components, the predictions of the two theories differ in the relative amplitudes of the dispersive contribution. If the phonon-vibrational coupling is independent of the electronic state, both predictions are identical.

It is shown that at low laser power if the dispersive component of the line is neglected, the sudden jump model can always describe the phenomenological temperature dependence of the linewidth and the line frequency.

At high laser power the line shape broadens and shows an interesting partial memory effect. The actual line can display a behavior intermediate to the behavior expected from a combination of two independent lines and from a single line with a complex line shape.

Appendix B

Solving seven linear equations is a conceptually trivial but lengthy exercise. In this Appendix we provide some details for those who would try to reproduce the solution.

First, Eq. (92, 93) can be easily solved for ρ_{55} and ρ_{66} .

$$\rho_{55} = \Theta \cdot \frac{\Gamma_{TS}\rho_{22} + \Gamma_{65}(\rho_{22} + \rho_{44})}{\Gamma_{TS} + \Gamma_{56} + \Gamma_{65}}, \quad (116)$$

$$\rho_{66} = \Theta \cdot \frac{\Gamma_{TS}\rho_{44} + \Gamma_{56}(\rho_{22} + \rho_{44})}{\Gamma_{TS} + \Gamma_{56} + \Gamma_{65}}, \quad (117)$$

and

$$\rho_{55} + \rho_{66} = \Theta(\rho_{22} + \rho_{44}), \quad (118)$$

where $\Theta = \Gamma_{ST}/\Gamma_{TS}$. The energy of the PLV does not change significantly when the molecule is in the triplet state and hence $\Gamma_{56}/\Gamma_{65} \approx B \ll 1$. If $\Gamma_{TS} \ll \Gamma_{56}$ from Eq. (116) it follows that

$$\rho_{55} = \frac{\Theta}{1+B}(\rho_{22} + \rho_{44}) \approx \Theta(\rho_{22} + \rho_{44}), \quad (119)$$

Useful relations can be obtained from Eqs. (90, 91).

$$\rho_{22} = -\Omega \frac{(\Gamma_{42} + 2\gamma)\text{Im}[\tilde{\rho}_{12}] + \Gamma_{42}\text{Im}[\tilde{\rho}_{34}]}{2\gamma(\Gamma_{42} + \Gamma_{24} + 2\gamma)} \quad (120)$$

and

$$\rho_{44} = -\Omega \frac{\Gamma_{24}\text{Im}[\tilde{\rho}_{12}] + (2\gamma + \Gamma_{24})\text{Im}[\tilde{\rho}_{34}]}{2\gamma(\Gamma_{42} + \Gamma_{24} + 2\gamma)}, \quad (121)$$

where a notation $2\gamma = 2\gamma_0 + \Gamma_{ST}$ is used for a brevity. Equations (95, 96) solved for $\tilde{\rho}_{12}$ and $\tilde{\rho}_{34}$ give the imaginary parts of $\tilde{\rho}_{12}$ and $\tilde{\rho}_{34}$

$$\frac{\Omega\text{Im}[\tilde{\rho}_{12}]}{2\gamma} = \frac{\Omega^2}{4\gamma} \text{Re}\left[\frac{\Gamma_{34}^* + i(\omega - \Delta)}{N}\right](\rho_{22} - \rho_{11}) + \frac{\Omega^2}{4\gamma} \text{Re}\left[\frac{\Gamma_{3412}}{N}\right](\rho_{44} - \rho_{33}) \quad (122)$$

$$\frac{\Omega\text{Im}[\tilde{\rho}_{34}]}{2\gamma} = \frac{\Omega^2}{4\gamma} \text{Re}\left[\frac{\Gamma_{1234}}{N}\right](\rho_{22} - \rho_{11}) + \frac{\Omega^2}{4\gamma} \text{Re}\left[\frac{\Gamma_{12}^* + i\omega}{N}\right](\rho_{44} - \rho_{33}), \quad (123)$$

where $\Gamma_{34}^* = \Gamma_{34} + \gamma_0$ and $\Gamma_{12}^* = \Gamma_{12} + \gamma_0$. From Eqs. (94, 118, 120, 121) the relation

$$\rho_{11} - \rho_{22} = 1 - (\rho_{33} - \rho_{44}) + (2 + \Theta) \left(\frac{\Omega\text{Im}[\tilde{\rho}_{12}]}{2\gamma} + \frac{\Omega\text{Im}[\tilde{\rho}_{34}]}{2\gamma} \right) \quad (124)$$

follows for the population differences. Using Eqs. (89, 94, 119, 120, 121), $\rho_{33} - \rho_{44}$ can also be expressed through $\text{Im}[\tilde{\rho}_{12}]$ and $\text{Im}[\tilde{\rho}_{34}]$ as

$$\rho_{33} - \rho_{44} = \frac{\Gamma_{13}}{K_{31}} + \Omega \frac{(K_{42} + K_{31})\text{Im}[\tilde{\rho}_{34}] - \Gamma_{24}\text{Im}[\tilde{\rho}_{12}]}{K_{31}(K_{42} + 2\gamma)} + \left(\frac{\Gamma_{13} + \Theta\Gamma_{13}}{K_{31}} + \frac{\Gamma_{24}}{K_{42} + 2\gamma} \right) \frac{\Omega\text{Im}[\tilde{\rho}_{12}] + \text{Im}[\tilde{\rho}_{34}]}{2\gamma}, \quad (125)$$

where $K_{31} = \Gamma_{31} + \Gamma_{13}$, $K_{42} = \Gamma_{42} + \Gamma_{24}$, and $(\Gamma_{ST}/K_{31}) \cdot \rho_{44}$ was neglected in the right hand side on the ground that $\Gamma_{ST}/K_{31} \ll 1$. Under the approximations $2\gamma \ll K_{42}$ and $\Gamma_{24}/K_{42} \approx \Gamma_{13}/K_{31} \approx B \ll 1$,

$$\rho_{33} - \rho_{44} = B \left\{ 1 + (2 + \Theta) \frac{\Omega\text{Im}[\tilde{\rho}_{12}]}{2\gamma} + \left(2 + \Theta + \frac{2\gamma}{\Gamma_{13}} + \frac{2\gamma}{\Gamma_{24}} \right) \frac{\Omega\text{Im}[\tilde{\rho}_{34}]}{2\gamma} \right\}. \quad (126)$$

The four Eqs. (122, 123, 124, 126) can be solved for $\text{Im}[\tilde{\rho}_{34}]$ and $\text{Im}[\tilde{\rho}_{12}]$ to obtain the population of the electronically excited states $n_e = \rho_{22} + \rho_{44} = -(\text{Im}[\tilde{\rho}_{12}] + \text{Im}[\tilde{\rho}_{34}])\Omega / (2\gamma)$ which is given by Eq. (102).

Through this appendix we assume that $(2 + \Theta)\Omega^2\sigma_2(\omega) \ll 4\gamma$. In such a case

$$\begin{aligned} n_e &= \frac{[R_1(\omega) + R_2(\omega)]\Omega^2}{4\gamma + (2 + \Theta)\Omega^2[R_1(\omega) + R_2(\omega)]} = \frac{R_1(\omega) + R_2(\omega)}{4\gamma + (2 + \Theta)\Omega^2 R_1(\omega)} \left(1 - \frac{(2 + \Theta)\Omega^2 R_2(\omega)}{4\gamma + (2 + \Theta)\Omega^2 R_1(\omega)} \right) \\ &= \frac{R_1(\omega)\Omega^2}{4\gamma + (2 + \Theta)\Omega^2 R_1(\omega)} + \frac{R_2(\omega)\Omega^2}{4\gamma + (2 + \Theta)\Omega^2 R_1(\omega)} \left[\frac{4\gamma}{4\gamma + (2 + \Theta)\Omega^2 R_1(\omega)} - \frac{(2 + \Theta)\Omega^2 R_2(\omega)}{4\gamma + (2 + \Theta)\Omega^2 R_1(\omega)} \right] \end{aligned} \quad (127)$$

The second term in square brackets in Eq. (127) can be neglected since $(2 + \Theta)\Omega^2 R_2(\omega) \ll 4\gamma$ and thus

$$n_e = \frac{R_1(\omega)\Omega^2}{4\gamma + (2 + \Theta)\Omega^2 R_1(\omega)} + \frac{4\gamma R_2(\omega)\Omega^2}{[4\gamma + (2 + \Theta)\Omega^2 R_1(\omega)]^2} \quad (128)$$

The second term in this equation can be replaced by $R_2\Omega^2/4\gamma$. Indeed

$$\frac{4\gamma R_2\Omega^2}{[4\gamma + (2 + \Theta)\Omega^2 R_1]^2} - \frac{R_2\Omega^2}{4\gamma} = \frac{\Omega^2 R_1}{4\gamma + (2 + \Theta)\Omega^2 R_1} \cdot \frac{(2 + \Theta)R_2\Omega^2}{4\gamma} \cdot \frac{8\gamma + (2 + \Theta)\Omega^2 R_1}{4\gamma + (2 + \Theta)\Omega^2 R_1} \quad (129)$$

and thus since $(2 + \Theta)\Omega^2 R_2 \ll 4\gamma$, the difference is much smaller than the first term for all ω . The final result reads

$$n_e \approx \frac{R_1(\omega)\Omega^2}{4\gamma + (2 + \Theta)\Omega^2 R_1(\omega)} + \frac{R_2(\omega)\Omega^2}{4\gamma} \quad (130)$$

The first term in Eq. (130) can be written in a simple form (we drop for a moment δ_ω which can be easily restored).

$$\begin{aligned} \Omega^2 \frac{\frac{A_1\Gamma_0 + \Phi\omega}{\omega^2 + \Gamma_0^2}}{4\gamma + (2 + \Theta)\Omega^2 \frac{A_1\Gamma_0 + \Phi\omega}{\omega^2 + \Gamma_0^2}} &= \frac{\Omega^2}{4\gamma} \frac{A_1\Gamma_0 + \Phi\omega}{\omega^2 + \frac{(2 + \Theta)\Omega^2}{4\gamma}\Phi\omega + \left[\Gamma_0^2 + \frac{(2 + \Theta)\Omega^2}{4\gamma}A_1\Gamma_0 \right]} \\ &= \frac{\Omega^2}{4\gamma} \frac{A_1\Gamma_0 + \Phi\omega}{\left(\omega + \frac{(2 + \Theta)\Omega^2}{8\gamma\Gamma_0}\Phi\Gamma_0 \right)^2 + \Gamma_0^2 \left[1 + \frac{(2 + \Theta)\Omega^2}{4\gamma\Gamma_0}A_1 - \frac{1}{4} \left\{ \frac{(2 + \Theta)\Omega^2}{4\gamma\Gamma_0}\Phi \right\}^2 \right]} \end{aligned} \quad (131)$$

With a definition $A_1(2 + \Theta)\Omega^2/(4\gamma\Gamma_0) \equiv (2 + \Theta')\Omega^2/(4\gamma\Gamma_0) = I/I'_{sat}$, at moderate powers when $\Phi I/(2I'_{sat}) \ll 1$

$$n_e \approx \frac{I/I'_{sat}}{(2 + \Theta')} \Gamma_0 \cdot \left(\frac{A_1 \Gamma_0 + \Phi \omega}{\omega^2 + \Gamma_0^2 [1 + I/I'_{sat}]} + \frac{\Gamma_{34} A_2 - \Phi(\omega - \Delta)}{(\omega - \Delta)^2 + \Gamma_{34}^2} \right) \quad (132)$$

At these moderate powers Eq. (110) reads

$$n_e \approx \frac{I/I_{sat}}{(2 + \Theta)} \Gamma_0 \cdot \left(\frac{A_1 \Gamma_0 + \Phi \omega}{\omega^2 + \Gamma_0^2 [1 + I/I_{sat}]} + \frac{\Gamma_{34} A_2 - \Phi(\omega - \Delta)}{(\omega - \Delta)^2 + \Gamma_{34}^2} \right), \quad (133)$$

with a slightly different definition $I/I_{sat} \equiv (2 + \Theta)\Omega^2/(4\gamma\Gamma_0)$. At low temperatures $A_1 \approx 1$ and as a consequence $\Theta' \approx \Theta$ and $I/I'_{sat} \approx I/I_{sat}$ and thus Eqs.(132) and (133) become identical.

VI. Spectral Diffusion in Polyethylene and other Polymers

In this Chapter we consider in detail the effect of spectral diffusion (SD) in amorphous solids on the optical line shapes. The theoretical discussion is based on the TLS model briefly described in the section *Model for Molecule's Environment*.

The average of probe molecule linewidths in a host matrix depends on the measurement time t_m and the temperature T . For amorphous solids this dependence can be written as

$$\langle \Gamma \rangle = \langle \Gamma_\tau \rangle + a\rho_{tls}\langle \Lambda_{ij} \rangle T \cdot \ln [G(T) \cdot t_m]. \quad (134)$$

With all the assumptions made in the standard TLS model outlined in *Model for Molecule's Environment*, the $G(T)$ is a function which only weakly depends on T . $\langle \Gamma_\tau \rangle$ is the average lifetime-limited contribution, a is a proportionality factor, ρ_{tls} is the average concentration of TLSs, and $\langle \Lambda_{ij} \rangle$ is the ensemble average of the TLS—SM coupling strength, which reads

$$\Lambda_{ij} = \alpha \xi_{ij} D_j \propto \vec{p}_i \cdot \vec{D}_j, \quad (135)$$

where \vec{D}_j is the dipole moment difference between the two states of TLS, \vec{p}_i is the permanent dipole moment difference for the chromophore, ξ_{ij} is the orientation parameter, and α is the coupling parameter, which is assumed constant in the standard application of line shape theory to impurity spectra in solids in the presence of SD [72]. The frequency excursion for SM i caused by a flip of TLS j situated at a distance r_{ij} from the molecule is

$$\nu_{ij} = \Lambda_{ij} / r_{ij}^3. \quad (136)$$

Molecules and TLSs can be coupled by electric and strain dipole fields, both of which can be modeled by Eqs. (135, 136).

On the single-molecule level, the TLS model predicts a distribution of linewidths for a given t_m and T [72, 138, 139]. Single-molecule spectroscopy provides access to distribu-

tions of parameters rather than ensemble averages, so the TLS model can be tested more critically than with ensemble techniques.

In our experiments, linewidths of single terrylene molecules embedded in polyethylene (PE) were measured at 13 different temperatures covering the temperature range between 30 mK and 1800 mK. Though PE has regions with crystal-like structure [140], it can be made mostly amorphous by fast cooling at the glass transition temperature. The mean values of the linewidth distributions were proportional to the temperature in agreement with Eq. (134), but when the shapes of the measured histograms were compared to the simulated ones, a significant disagreement appeared. First, at the lowest temperature, where spectral diffusion was negligible, the linewidth distribution did not collapse to a single value indicating thus the

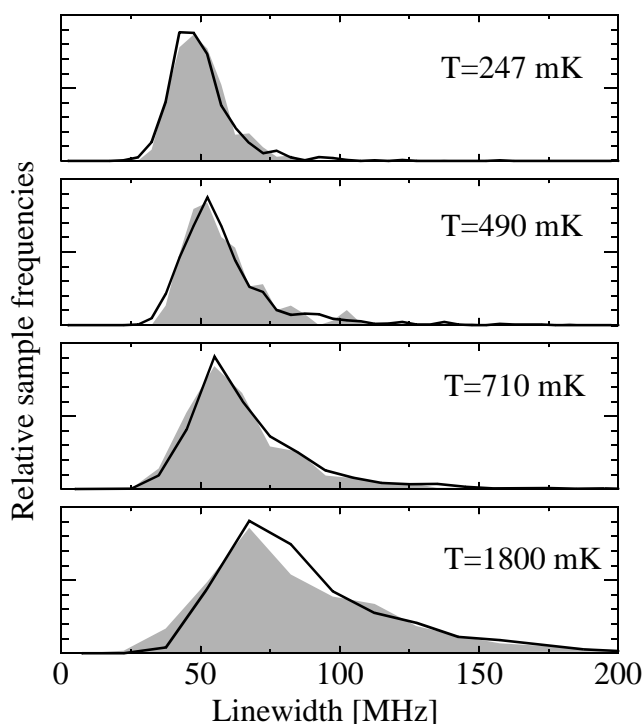


Fig. 32 Histograms of linewidth distributions (scaled to equal peak values) of single terrylene molecules doped in polyethylene measured at four different temperatures. The shaded histograms are the experimental results. The numbers of molecules in the experimental distributions are 421, 300, 359, and 205 counting from the lowest to the highest temperature. The solid lines show histograms of 1200 lines simulated with TLS model modified by adding a distribution of the lifetime limited linewidths and a distribution of coupling constants. Both distributions were assumed Gaussian with relative standard deviations of approximately 20%. The agreement between experimental results and simulations is better than 50% (confidence level) at all temperatures.

presence of a distribution of lifetimes of the electronically excited state. As temperatures increased and hence the mean contribution from spectral diffusion increased (in agreement with Eq. (134)) making the distribution of lifetimes less significant, the agreement between the simulations where an equal lifetime of the excited state was assigned to each molecule and the experiment improved but only to a confidence level of 1% at 1480 mK (with 584 molecules measured). With a distribution of lifetimes, the confidence level increased slightly to 5%. Only when a distribution of the coupling constant α was added to the model an agreement with a comfortable confidence level of 50% was achieved. The

experimental results and the Monte Carlo simulations are shown in Fig. 32. The ratios of the standard deviations of the distributions to the mean values for α and Γ_τ are approximately 20%. This might indicate that the physical origins of the two distributions are related. Indeed, the transition dipole moment distribution (responsible for a distribution of lifetimes) and the induced permanent dipole moment distribution (responsible for an α distribution) are both caused by perturbations to the wave functions from the neighboring host molecules. Details are given in the chapter *Distribution of Radiative Lifetimes*.

Fluctuations of the TLS density ρ_{tls} could also cause a broader measured linewidth distribution because in our experiments only the product $\alpha\rho_{tls}$ is essential. This is a problem not only of single molecule spectroscopy but of all optical experiments performed so far and based on optical measurements one can not separate ρ_{tls} and α . The reader should not mix these fluctuations of ρ_{tls} with the Poissonian fluctuations arising from the randomness in the spatial locations of TLSs. The Poissonian fluctuations are automatically taken into account in the Monte Carlo simulations. Variations of α and ρ_{tls} are both related to some kind of nanoscopic inhomogeneities. The origin of TLSs comes from a presence of voids in the sample [74] and thus a change in TLS density can be viewed as a change in polymer density which takes place on a scale of few nanometers. In principle, fluctuations of the polymer density on a scale much larger than the distances between probe molecules and TLSs contributing to the broadening (~ 10 nm) can be present in the sample as well. Although the polymer was effectively annealed above its glass transition temperature one can not completely rule out inhomogeneities on the scale of a few microns although these inhomogeneities do not play a major role at least for the radiative lifetime distribution (see *Distribution of Radiative Lifetimes*). Variations of α are caused by variations of solvent shell structure rather than macroscopic polymer density.

A much stronger environmental effect can be observed in other polymers. An example is shown in Fig. 33. A histogram of 486 linewidths of single terrylene molecules embed-

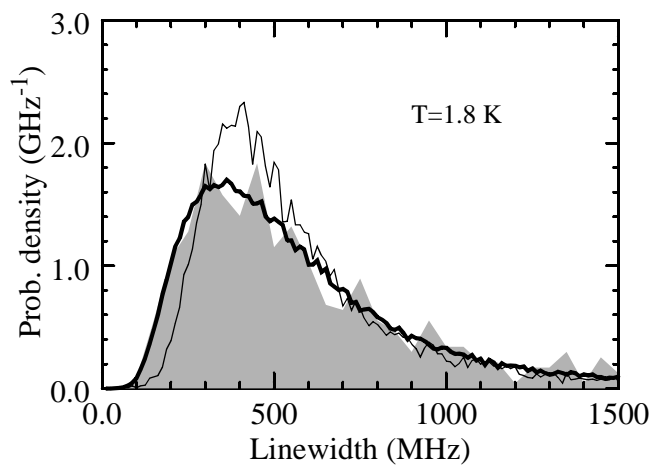


Fig. 33 Distribution of single molecule linewidth of terrylene in PVB. Also shown are two simulated distributions with the mean value of the coupling constant $\langle \alpha \rangle = 154 \text{ GHz nm}^3$. The thin line corresponds to the fit with a narrow α distribution. The thick line corresponds to the presence $\sim 50\%$ standard deviation in the α distribution.

ded in polyvinylbutyral (PVB) shows a distribution which is ten times broader and has a maximum shifted by 300 MHz in comparison with the highest temperature distribution in Fig. 32.

Details

In comparison with other systems, polyethylene doped with terrylene was investigated most carefully. The temperatures, the number of terrylene molecules measured, the average linewidths, and the standard deviations of the linewidth distributions are summarized in Table 3. Some of the measurements were performed in the thin-film sample and some were performed in the sandwich sample, as indicated. Complicated broadening effects assumed to arise from surface phonons [141], as well as lifetime changes caused by changes in the vacuum electromagnetic mode structure near surfaces [142] are known to take place in thin samples, which could complicate interpretation of the linewidth distributions. To prepare the thin doped layer, a bulk sample was produced by means of diffusion, by heating a small amount of terrylene together with some PE at 180 °C under vacuum for several hours. A small amount of the hot mixture was then

TABLE 3. Temperature dependence of the average linewidth. Data are measured with two samples.

| T [mK] | N | $\langle\Gamma_0\rangle$ [MHz] | σ [MHz] |
|------------------|-----|-----------------------------------|-------------------|
| Sandwich sample | | | |
| 30 | 380 | 42.8(6) | 12(1) |
| 43 | 32 | 42.6(23) | 13(2) |
| 50 | 407 | 43.5(5) | 10(1) |
| 950 | 65 | 73.4(41) | 32(4) |
| 1200 | 157 | 87.3(20) | 36(3) |
| 1480 | 584 | 92.5(13) | 34(1) |
| 1640 | 93 | 103(4) | 39(4) |
| 1830 | 75 | 102(3) | 33(4) |
| Thin-film sample | | | |
| 247 | 421 | 51.0(5) | 12(1) |
| 490 | 300 | 58.4(11) | 17(1) |
| 710 | 359 | 63.7(12) | 21(1) |
| 1060 | 123 | 76.5(22) | 30(2) |
| 1800 | 436 | 96.4(28) | 57(3) |

squeezed under high pressure between two polished stainless steel flats (also heated to 180 °C) to produce a thin film and cooled by dropping the film together with the stainless steel flats into a bath of liquid nitrogen. For the layered sample, a piece of the doped film was then melted between two undoped PE films, so that no SM was within $\sim 10\ \mu\text{m}$ from the sample surface. The films were pressed together by applying a slight pressure and then quickly cooled in a bath of liquid nitrogen. The terrylene concentration in the doped film was $\sim 10^{-6}$ molar. The measured temperature interval was narrower for the thin-film sample

than for the sandwich sample. The data were collected using single-molecule microscopy [143], which has an advantage that many molecules from different areas of the sample are observable in parallel under identical experimental conditions. A solid mirror objective formed from two homocentric suprasil components has been specially developed to work in liquid He [144]. The optical properties of this objective do not change as severely in superfluid He, because the full light path is in the suprasil. Time constraints and technical difficulties prevented measurements in the thin-film sample at lower temperature.

$\langle \Gamma_0 \rangle$ is plotted against the temperature in Fig. 34. The solid lines are linear least-squares fits to the data collected with the thin-film sample (circles) and the sandwich (diamonds). Fits to $\langle \Gamma_0 \rangle = \tilde{a} + \tilde{b}T^{1.3}$ curves (dashed lines) are also shown for comparison. A “super-linear” behavior $\langle \Gamma_0 \rangle = \tilde{a} + \tilde{b}T^{1+\zeta}$, with $\zeta \approx 0.3$ was observed in several experiments [145, 146]. With the “standard” distribution functions of the TLS parameters (see *Model for Molecule’s Environment*) and making some other approximations concerning “TLS-phonon” coupling, a simple theoretical analysis predicts a linear temperature dependence. Motivated by this result a modification for Eq. (14) was suggested

[147] to get an agreement with the superlinear temperature dependence. A more accurate consideration [148, 149, 150] reveals that even within the standard distribution function a superlinearity with $\zeta \approx 0.1 \div 0.3$ appears which however depends on the details of the TLS-phonon interaction. Thus for those authors a linear dependence would require a modification of the distribution function. At temperatures above 1 K a broadening caused by an activation of pseudo local phonons may become significant. This can also lead to an apparent superlinearity in the temperature dependence. Unfortunately, there is a shortage of

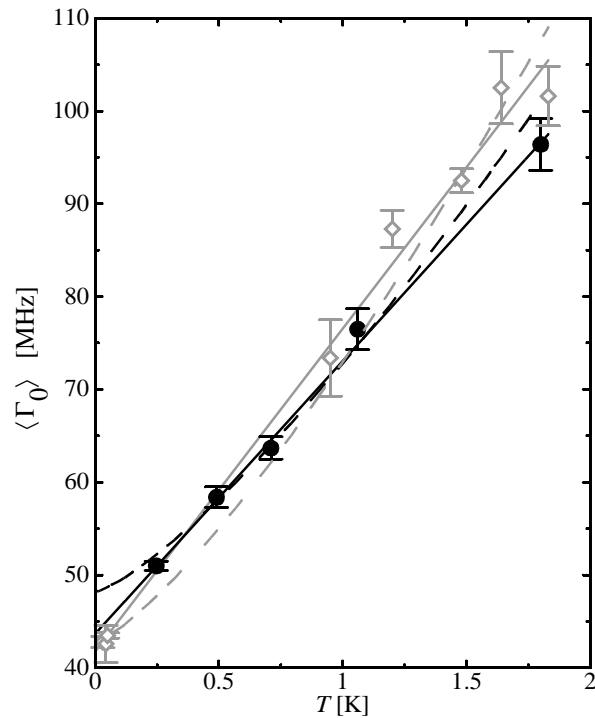


Fig. 34 The average linewidth as a function of temperature. The diamonds and the circles were measured with the sandwich and the thin-film sample, respectively. The solid lines are linear least-squares fits to the data, and the dashed lines are fits to a $T^{1.3}$ dependence.

reliable experimental data below 1 K and it is not clear to which extent a correction of the distribution function is necessarily. We will not pay too much attention to this subject but for a completeness we have analyzed our experimental data assuming $\zeta = 0$ and $\zeta = 0.3$. The fit parameters and the confidence intervals for least-squares fits to the data are presented in Table 4 for both a linear and a $T^{1.3}$ temperature dependence. Based on the

TABLE 4. Fit parameters and values for $\langle \Gamma_0 \rangle = a + bT$ trial function for the temperature dependence of the mean linewidth.

| a [MHz] | b [MHz/K] | P |
|------------------|----------------|-----|
| Sandwich sample | | |
| 41.7(3) | 35.2(8) | 37% |
| Thin-film sample | | |
| 44.0(10) | 30.0(22) | 75% |

TABLE 4 a. Fit parameters and values for $\langle \Gamma_0 \rangle = \tilde{a} + \tilde{b}T^{1.3}$ used as a trial function. Generally the confidence interval is larger for the linear fit.

| \tilde{a} [MHz] | \tilde{b} [MHz/K ^{1.3}] | P |
|----------------------|--|-----|
| Sandwich sample | | |
| 42.8(3) | 30.5(7) | 1% |
| Thin-film sample | | |
| 48.2(6) | 24.6(16) | 55% |

confidence intervals, the linear relationship fits the data better than the $T^{1.3}$ temperature dependence for both samples. If all of the data is combined into one data set and fit simultaneously, the linear fit still fits reasonably well (25% confidence level), while the $T^{1.3}$ dependence fits very badly with an infinitesimal confidence levels. This is because the three lowest-temperature data points fall several standard deviations away from the $T^{1.3}$ fit. The slope of the linear fit is smaller and the intercept is larger for the data collected with the thin-film sample. The differences in slope and intercept are statistically significant and indicates that the SD is smaller in the sandwich-sample. The differences in the two data sets are examined further in where the linewidth distributions are fit to the TLS model.

Fitting the linewidth distributions.

So far the data has been presented in terms of ensemble averages, which could have been measured with an ensemble technique like hole burning, for example. In this section, the power of single-molecule spectroscopy for measuring the distributions of parameters is revealed, and the linewidth distributions are studied by comparing them to distributions simulated with the TLS model. Since the temperature dependence of the average linewidth

was linear, a constant density of states for the TLS energy splittings was used without the phenomenological adjustments that are sometimes applied to produce a $T^{1.3}$ temperature dependence [72, 145]. We did, however, modify the model to include distributions for the lifetime-limited linewidth and the coupling strength.

In contrast to other hosts like polyvinylbutyral, for which the average SM linewidth is an order of magnitude larger than Γ_τ for terrylene molecules in PE the average linewidth at 1.8 K is only about a factor of two larger than Γ_τ . For this reason, lifetime variations play a significant role in the linewidth distribution and have to be included in the model — especially at lowest temperature where the distribution is narrowest but does not collapse to a single value as one would expect if all molecules had the same Γ_τ values.

To fit the data reasonably well at higher temperature, it was also necessary to include a distribution of coupling strengths α in the simulations. For simulating linewidth distributions one usually assumes a specific TLS density and uses α as a fit parameter, but the amount of line broadening is only sensitive to the product $\alpha\rho_{tls}$. For the simulations presented below, $\rho_{tls} = 0.014 \text{ nm}^{-3}$ for TLSs with a maximum energy splitting $E_{max} \approx 13 \text{ K}$ and a maximum flipping time of $\sim 3000 \text{ s}$.

For the simulations, it has been assumed that α and Γ_τ both have Gaussian distributions. Since broadening from spectral diffusion is stronger at higher temperatures, the 1.48 K data were used to find the α distribution. The 30 mK data were used to find the Γ_τ distribution, since at such low temperatures the broadening of the linewidth distribution from spectral diffusion is minimal.

The parameters for the α and Γ_τ distributions were found by guessing initial values, simulating distributions, and then minimizing χ^2 in a goodness-of-fit comparison (see *Appendix E* for details). After the suitable parameters had been found, the distributions of linewidths were simulated for the intermediate temperatures and χ^2 was

TABLE 5. The mean and the standard deviation for the α and Γ_τ distributions found by comparing the data to simulated linewidth distributions for the sandwich and the thin-film samples. The error intervals correspond to 95% confidence intervals.

| α [GHz nm ³] | σ_α [GHz nm ³] | $\langle\Gamma_\tau\rangle$ [MHz] | σ_{Γ_τ} [MHz] |
|------------------------------------|---|--------------------------------------|---------------------------------|
| Sandwich sample | | | |
| 11(2) | 2 | 38.8 ± 1.6 | 7.6 ± 1.1 |
| Thin-film sample | | | |
| 7.5(25) | 2.5 | 42.3 ± 1.7 | 6.7 ± 1.7 |

calculated with no fit parameters. The parameters that were found to best fit the data are shown in Table 5.

The linewidth distributions for $T = 30$ mK and 1480 mK measured in the sandwich sample are shown in Fig. 35 together with the simulations. The simulated linewidth distribution for 30 mK is very close to the Gaussian Γ_τ distribution used as input to the simulation. The low-temperature data can actually be fit better when one assumes a Gaussian distribution of lifetimes rather than a Gaussian Γ_τ distribution, but the Γ_τ distribution found from the T_1 distribution for such a fit does not have a first moment. Since we are comparing linewidth distributions, we chose to use a Gaussian Γ_τ distribution instead and we do not encounter this problem when com-

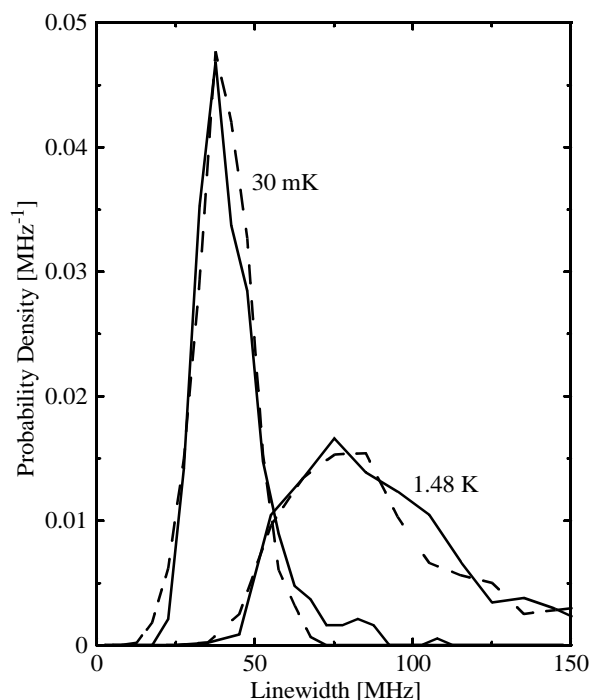


Fig. 35 The distributions of linewidths for T equals 30 and 1480 mK, with distributions simulated following the procedure explained in the text. The solid lines are the experimental data and the dashed lines are the simulations.

paring the data and the simulations. Because of the long tail toward large linewidths, the standard deviation of the sample population (presented in the fourth column of Table 3 is 40% larger than the standard deviation one finds from a Gaussian fit.

The standard deviation of the distribution measured at 30 mK found with a weighted Gaussian fit is 8.7 MHz. The distribution of Γ_τ that fits the data best has a standard deviation of 7.6 MHz, thus the spectral diffusion contribution is 1.1 MHz. The major contribution to σ_{Γ_τ} is from the lifetime, it also includes a small noise contribution since the measured distribution is slightly broadened by the signal noise while the simulated spectra are noise free. Each line was measured several times to determine the fluctuations of the linewidth caused by the noise. With a reasonable approximation these fluctuations could be described by a Gaussian distribution function. The standard deviation varied from molecule to molecule in a range of $(1 \div 5)$ MHz and was inversely proportional to the line am-

plitude. Correcting for this random noise, the standard deviation of the lifetime-limited linewidth distribution is 6.8 MHz.

The confidence levels for the agreement between the data and the simulations produced by fitting the sandwich-sample data are shown in the third column of Table 6.

The measurements performed with the thin-film sample can not be fit with the same lifetime and α distributions as the layered sample measurements. The disagreement in most pronounced at 250 mK. The simu-

TABLE 6. Temperature dependence of the average linewidth. Data are measured with two samples.

| T [mK] | N | Confidence interval when $\alpha = 11 \text{ GHz nm}^3$ | Confidence interval when $\alpha = 7.5 \text{ GHz nm}^3$ |
|------------------|-----|---|--|
| Sandwich sample | | | |
| 30 | 380 | 55% | |
| 50 | 407 | 45% | |
| 1480 | 584 | 45% | |
| Thin-film sample | | | |
| 247 | 421 | 0.1% | 55% |
| 490 | 300 | 4% | 65% |
| 710 | 359 | 50% | 75% |
| 1800 | 205 | 1% | 65% |

lated distributions and distributions measured in the thin-film sample for temperatures of 250 mK and 710 mK are presented in Fig. 36. The shaded distributions are the experimental data, and the dotted lines are distributions simulated using the parameters found to fit the data measured in the layered sample. The peak linewidth for the 250 mK data is broader for the measured distribution than for the simulations, and a significant difference is visible in the linewidth distributions. This could either be caused by a larger coupling strength or a shorter lifetime. Since the slope of the temperature dependence is proportional to the average coupling strength (see Eq. (135)), the disagreement must be caused by a shorter lifetime in the thin-film sample, because the slope is smaller for the thin-film sample than for the sandwich sample (see Fig. 34). The mean and standard deviations of the Γ_τ distributions found by fitting the data are presented in Table 5. The errors correspond to approximately two standard deviations, and were found by varying the given parameter until the confidence interval for the agreement between the simulation and the data dropped below 5%. The Γ_τ distribution that best fits the linewidth distribution at 250 mK in the thin film sample (the solid curve shown in Fig. 35) had a 10% larger average value than the best fit to the 30 mK distribution in the sandwich sample (the solid curve shown

in Fig. 36 a). This difference is statistically significant (confidence interval $\sim 3\sigma$). Hence the lifetime in the thin-film sample is 10% shorter.

The data measured at 710 mK is shown in Fig. 36b with distributions simulated using the Γ_τ distributions found from fitting the sandwich and thin-film data at 30 mK and 250 mK, respectively. Both simulations fit the data well. The good agreement at 700 mK is partially accidental, since the linear temperature dependences cross for the two samples at $T \approx 0.5$ K. Hence, the narrower lifetime-limited linewidth in the sandwich sample partially compensates for the reduced spectral diffusion in the thin-film sample. At 1.8 K the disagreement becomes pronounced again because the curves begin to diverge and the precise form of the α distribution becomes important. The thin-film sample has less spectral diffusion arising from TLSs,

judging from the slope of the temperature dependence and the best-fit value for α in Table 5.

Neither of the surface effects once feared are present in the thin-film sample. The average coupling constant is $\sim 25\%$ smaller in the thin-film sample than in the layered sample as indicated by the slope of the temperature dependence and the average α values. So extra broadening from surface phonons [141] does not arise. There is also no perturbation of the average lifetime from the interface between the polyethylene and the liquid helium. This effect would produce a lengthening rather than a shortening of the lifetime [151].

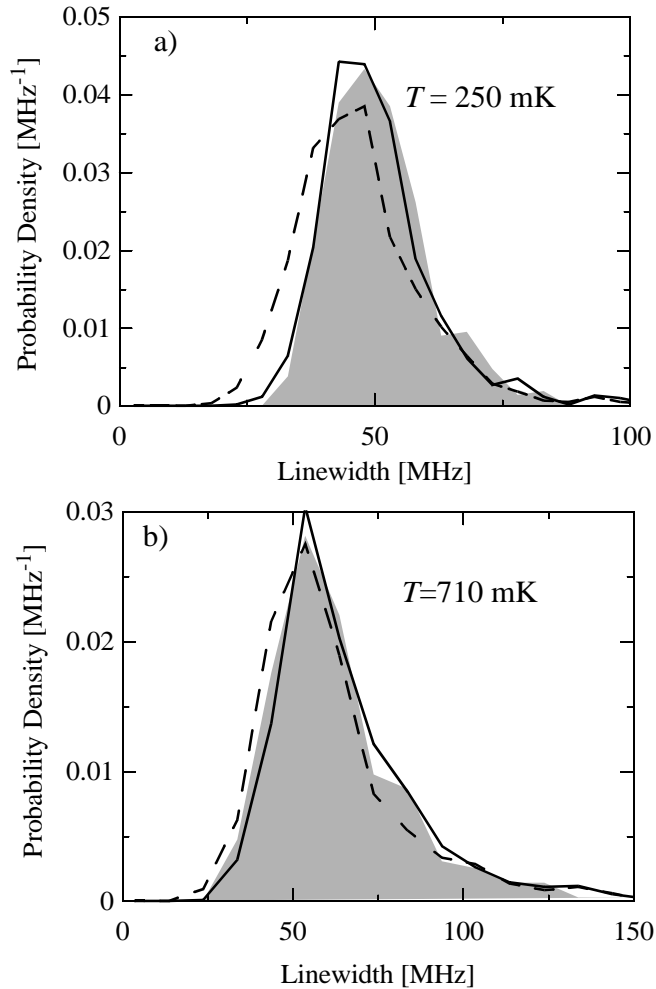


Fig. 36 Comparison of simulated and measured linewidth distributions at 250 mK, (part a) and 710 mK, (part b). The shaded distributions are the measured data. The dashed and solid lines are simulated distributions for average lifetime-limited linewidths of 38.8 and 42.3 MHz, respectively.

The shorter lifetime in the thin-film sample probably results from a higher refractive index since the thin film was produced by squeezing the sample under high pressure. The same thin film was used to make the layered sample, but it was effectively annealed when the layers were melted together. The radiative lifetime of a probe molecule in a solvent relative to its free-space lifetime is

$$\langle \gamma \rangle = \gamma_{vac} \frac{\epsilon^{1/2}(\epsilon + 2)^2}{9} \quad (137)$$

The $\epsilon^{1/2}$ factor arises from a change in the speed of light in the medium. By linearizing Eq. (137) around $\epsilon = 2.3$ one finds that a reduction of the lifetime of 10% corresponds to an increase of the refractive index by $\sim 3\%$. This is not a large increase considering that the density of crystalline polyethylene is 18% higher than for amorphous PE at room temperature [152].

It might at first seem counterintuitive that for a sample in which the probe molecules have a larger local-field factor, the coupling constant does not increase as well. The coupling constant in fact goes down, but this is not contradictory. The higher local field factor is caused by a higher host density so there are fewer voids in the solvent structure. Assuming that TLSs are located in positions adjacent to these voids [153], a lower void concentration means that the TLS density is also lower, which results in less spectral diffusion as evident in Eq. (134). This is consistent with spectral hole burning measurements that showed a decrease in the hole width and spectral diffusion with applied pressure [154]. We find that the ratios of the standard deviations of the distributions to the mean values for α and γ for both samples are $\sim 20\%$.

In fact, α and Γ_τ might even be correlated as we suggested previously [155]. The data collected at 1480 and 1800 mK were also fitted with correlated distributions such that the slope of a plot of the normalized α values vs. the normalized Γ_τ values was equal to one. The data could be fit equally well, but with a larger mean value and a narrower distribution for α . For example, the coupling constant distribution that best fit the sandwich-sample data with the correlation had a mean of 11.8 GHz nm^3 and a standard deviation of $\sim 10\%$. With the statistical uncertainty of our data, we cannot say if the distributions are fit better with or without the correlation.

Appendix D

Consider a subensemble of probe molecules with equal value of $p \equiv p_i$. Each molecule of this type interacts with a set of TLS characterized by the set of ν values which enter into Eq. (136). With $\nu = p_i D \xi r^{-3}$ and disregarding the constant p_i the distribution function for ν reads

$$P_\nu(\nu) = \int \int P_{\xi D}(\xi, D) d\xi dD \int_0^{r_{max}} \delta(D \xi r^{-3} - \nu) P_r(r) dr \quad (138)$$

where $P_{\xi D}(\xi, D)$ is the probability distribution function for ξ and D , $P_r(r) = 3r^2/r_{max}^3$ is the probability distribution function for r , and δ stays for a δ -function. We introduce a new variable x to replace r according to $r = [D\xi/(x + \nu)]^{1/3}$ in the last integral of Eq. (138) and obtain

$$P_\nu(\nu) = \int_{D\xi > 0} \int P_{\xi D}(\xi, D) d\xi dD \int_{D\xi r_{max}^{-3} - \nu}^{\infty} \delta(x) 3 \frac{[D\xi/(x + \nu)]^{2/3}}{r_{max}^3} \frac{1}{3} (D\xi)^{1/3} \frac{1}{(x + \nu)^{4/3}} dx$$

$$- \int_{D\xi < 0} \int P_{\xi D}(\xi, D) d\xi dD \int_{-\infty}^{D\xi r_{max}^{-3} - \nu} \delta(x) 3 \frac{[D\xi/(x + \nu)]^{2/3}}{r_{max}^3} \frac{1}{3} (D\xi)^{1/3} \frac{1}{(x + \nu)^{4/3}} dx \quad (139)$$

The first integral is nonzero if $D\xi r_{max}^{-3} < \nu$ while for the second integral this condition reads $D\xi r_{max}^{-3} > \nu$. Integration in (139) over dx gives

$$P_\nu(\nu) = \frac{1}{\nu^2 r_{max}^3} \int_{0 < D\xi < \nu r_{max}^3} \int |\xi D| P_{\xi D}(\xi, D) d\xi dD \quad , \nu > 0 \quad (140)$$

and

$$P_\nu(\nu) = \frac{1}{\nu^2 r_{max}^3} \int_{0 > D\xi > \nu r_{max}^3} \int |\xi D| P_{\xi D}(\xi, D) d\xi dD \quad , \nu < 0 \quad (141)$$

For evaluation of SD, only the absolute value of ν is of interest

$$P_{|\nu|}(|\nu|) = \frac{1}{\nu^2 r_{max}^3} \int_{|D\xi| < |\nu| r_{max}^3} \int |\xi D| P_{\xi D}(\xi, D) d\xi dD \quad (142)$$

In a general case the region of integration is complex but it is very simple if $|\nu| > \max\{|D\xi|\}/r_{max}^3$. In this case

$$P_{|\nu|}(|\nu|) = \frac{\langle |\xi| |D| \rangle}{\nu^2 r_{max}^3} = \frac{\langle |\xi| \rangle \langle |D| \rangle}{\nu^2 r_{max}^3} . \quad (143)$$

The second equality is correct if D and ξ are not correlated that is $P_{\xi D}(\xi, D) = P_D(D) \cdot P_{\xi}(\xi)$. For electric dipole-dipole interaction $\langle |\xi| \rangle \approx 0.7$.

In some cases $P_{|\nu|}(|\nu|)$ can be calculated analytically.

Example 1

$$P_{\xi}(\xi) = \frac{1}{2} \cdot d\xi , \text{ where } -1 < \xi < 1 \quad (144)$$

(this corresponds to $\xi = \cos\theta$, where $0 < \theta < \pi$ and $P_{\theta}(\theta) = \frac{1}{2} \sin\theta$).

$$P_D(D) = D_{max}^{-1}, \text{ where } 0 < D < D_{max} . \quad (145)$$

For such distributions Eq. (142) for $|\nu| \leq D_{max}/r_{max}^3$ reads

$$\begin{aligned} P_{|\nu|}(|\nu|) &= \frac{\int_{|D\xi| < |\nu| r_{max}^3} |\xi| D |d\xi dD|}{2 D_{max} \nu^2 r_{max}^3} = \frac{\int_0^{|\nu| r_{max}^3} D \int_0^1 \xi d\xi dD + \int_{|\nu| r_{max}^3}^{D_{max}} D \int_0^{\frac{|\nu| r_{max}^3}{D}} \xi d\xi dD}{D_{max} \nu^2 r_{max}^3} \\ &= \frac{1}{D_{max} \nu^2 r_{max}^3} \left(\frac{\nu^2 r_{max}^6}{4} + \frac{\nu^2 r_{max}^6}{2} \ln \left[\frac{D_{max}}{|\nu| r_{max}^3} \right] \right) = \frac{r_{max}^3}{4 D_{max}} \left(1 + 2 \ln \left[\frac{D_{max}}{|\nu| r_{max}^3} \right] \right) \end{aligned} \quad (146)$$

and

$$P_{|\nu|}(|\nu|) = \frac{D_{max}}{4 \nu^2 r_{max}^3} \text{ if } |\nu| \geq D_{max}/r_{max}^3 . \quad (147)$$

Example 2

$$P_D(D) = \delta(D - D_0) \quad (148)$$

and $P_{\xi}(\xi)$ is described by Eq. (144). In this case for $|\nu| \leq D_0/r_{max}^3$

$$P_{|\nu|}(|\nu|) = \frac{D_0}{\nu^2 r_{max}^3} \int_0^{|\nu| D_0^{-1} r_{max}^3} \xi d\xi = \frac{r_{max}^3}{2D_0} \text{ if } |\nu| \leq D_0/r_{max}^3 \quad (149)$$

$$P_{|\nu|}(|\nu|) = \frac{D_0}{2\nu^2 r_{max}^3} \text{ if } |\nu| \geq D_0/r_{max}^3 \quad (150)$$

Appendix E

To obtain a quantitative measure for dissimilarity between two histograms one can calculate χ^2 parameter according to the definition

$$\chi^2 = \sum_{i=1}^{\Omega} \frac{[N_i - M(x_i)]^2}{\sigma_i^2}, \quad (151)$$

where N_i is the number of molecules having a value of x in the interval $x_i - \delta < x < x_i + \delta$, Ω is the total number of intervals in the histogram, a Gaussian distribution is assumed for the fluctuations of N_i around its mean value $M(x_i)$ predicted by a model, σ_i is the standard of this Gaussian distribution. If the measured molecules are taken at random, $\sigma_i^2 = N(x_i)^{1/2}$.

The larger is the value of χ^2 the smaller is the probability that a particular histogram can be observed given the model under consideration is correct.

Of course this probability depends on the number of adjustable parameters in the model. If the number of parameters is P , a normalized value χ_v^2 can be considered.

$$\chi_v^2 = \frac{\chi^2}{\Omega - (P + 1)}. \quad (152)$$

The distribution function for χ_v^2 is tabulated and can be found in text books. Two definitions are important for the data analysis.

A confidence level is defined as the probability to have the calculated or smaller value of χ_v^2 assuming that the deviation between N_i and $M(x_i)$ is caused by statistical fluctuations.

A confidence interval for a fit parameter is defined as the interval such that within this interval the confidence level is not smaller than a specified value (usually 5%).

VII. Distribution of Radiative Lifetimes

Although not always stated explicitly, the radiative lifetime has usually been assumed to be equal for like molecules. A text book statement that the influence of nearby molecules on a probe molecules averages out [20] made at a time when nobody would seriously think about measuring the lifetimes of individual molecules was taken for granted and the effect of the environment on the radiative lifetime was treated in a simplified manner using the Lorentz factor. Meanwhile, the sensitivity of the energy levels of chromophore molecules to the microscopic variations in the local environments that lead to inhomogeneous broadening has been general knowledge in solid state physics for decades and has even been used for information storage [31]. One may wonder if a similar effect can be observed for the lifetimes. Besides having fundamental interest, the presence of a lifetime distribution could have practical importance, for example, when the identification of single molecules is based on their lifetimes [156, 157] or when single molecules are used as nano probes in time-resolved experiments [158, 159].

Experimental access to the lifetimes of terrylene molecules embedded in polyethylene was gained by measuring single molecule linewidths at 30 mK. At this temperature spectral diffusion in polyethylene is negligible and only radiative and nonradiative decays contribute to the measured linewidths. Linewidth measurements for 380 single terrylene molecules (Fig. 37) clearly show a distribution with a relative standard deviation of approximately 20%. It was even possible to estimate radiative and nonradiative contributions to the measured linewidths separately. For a radiative lifetime distribution, the broad molecules have larger areas and a positive correlation would arise. A non-radiative lifetime distribution would cause a negative correlation. The correlation is obscured by a random orientation of the transition dipole moments of the terrylene molecules. Nevertheless an analysis of the linewidth — line area correlation clearly shows that the variations arise from approximately equal radiative and non radiative contributions and that the fluorescence quantum yield is approximately 70%. The time resolution with which the 380 lines were measured was limited to approximately 5 seconds. This is because the data were taken using a multi channel technique when several lines were recorded simultaneously with a sensitive video camera. ITFC spectra were also measured with a much higher time reso-

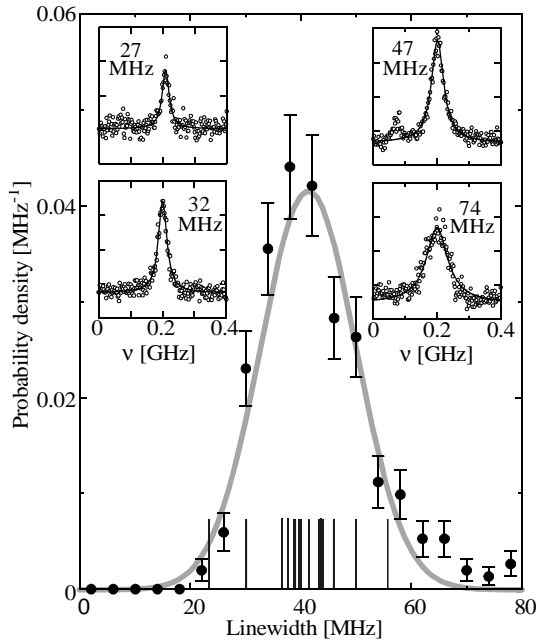


Fig. 37 The linewidth distribution for 380 SMs measured at 30 mK, with transition frequencies between 17446 cm^{-1} and 17455 cm^{-1} , which is on the red side of the inhomogeneous band. The solid line is a weighted fit to a Gaussian distribution. The standard deviation of the distribution is 8.7 MHz and the mean is 41.2(6) MHz. After subtraction of contributions from random errors, intensity inhomogeneities, and laser scan calibration errors, the remaining standard deviation of the distribution is 7.9 MHz. The events marked by vertical lines are 15 linewidths measured using the ITFC technique. Measurements at two different intensities were used to correct for power broadening. The mean and standard deviation for this distribution are 40.6(20) MHz, and 7.6(20) MHz respectively. The ITFC distribution only has 15 molecules because the method is a single-channel measurement technique. The insets show the spectra of four typical single molecules.

lution ($\sim 140 \text{ ms}$) to show that the distribution of linewidths was not caused by a light-induced spectral diffusion.

The distribution of the radiative linewidth γ can be caused by variations of the dielectric constant ϵ which result from variations of the partial mean of the polymer density D (the value averaged over a macroscopic space domain). In the following paragraph we show that such an explanation is in contradiction with the experimental results. The relationship between ϵ and γ [160] and between D and the partial mean of the transition frequency $\bar{\nu}$ [161, 162] are

$$\gamma \propto \epsilon^{1/2}(\epsilon + 2)^2 \quad (153)$$

and

$$\nu_{vac} - \bar{\nu} \propto D^2 \propto [(\epsilon - 1) / (\epsilon + 2)]^2. \quad (154)$$

From these equations it follows that $\sigma_{\gamma} / \langle \gamma \rangle = \frac{d\gamma}{d\epsilon} \cdot \sigma_{\epsilon} / \langle \gamma \rangle$ and $\sigma_{\bar{\nu}} / (\nu_{vac} - \langle \bar{\nu} \rangle) = \frac{dD}{d\epsilon} \cdot 2\sigma_{\epsilon} / \langle D \rangle$ and that the ratio of $\sigma_{\gamma} / \langle \gamma \rangle$ to $\sigma_{\bar{\nu}} / (\nu_{vac} - \langle \bar{\nu} \rangle)$ equals 0.6 (with $\langle \epsilon \rangle = 2.3$). Thus if the γ variations were caused by D fluctuations alone, γ would be a simple function of ν . Hence linewidth measurements over a narrow range of ν (as were done to obtain the distribution in Fig. 37) would only sample a narrow fraction of the linewidth distribution. The total solvent shift distribution may also include

a part uncorrelated with D . In this case, for each molecule $\nu = \bar{\nu} + \nu_{uncor}$, where we also assume that $\langle \nu \rangle = \langle \bar{\nu} \rangle$. If both $\bar{\nu}$ and ν_{uncor} have Gaussian distributions, molecules with the same ν should have the width of the $\bar{\nu}$ distribution at most half of the total inhomogeneous band width σ_ν . From the experiment $\sigma_\nu / (\nu_{vac} - \langle \nu \rangle) = 11\%$, hence $\sigma_{\bar{\nu}} / (\nu_{vac} - \langle \bar{\nu} \rangle) \leq 5.5\%$. At a given ν the relative width of the γ distribution ($\sigma_\gamma / \langle \gamma \rangle$) caused by variations of ϵ is at most $5.5\% \cdot 0.6 \approx 3\%$. This is much smaller than the experimentally observed relative standard deviation of the linewidth distribution ($\sim 20\%$) and thus a significant part of the linewidth distribution has a different origin.

Now we sketch a simple microscopical model which suggests that the distribution of radiative lifetimes in disordered media is a general effect caused by the interactions responsible for inhomogeneous broadening. In this model a host is made of noninteracting molecules. The coupling Hamiltonian \hat{w} between the chromophore and host molecules is reduced to a dipole-dipole interaction, a reasonable approximation for a nonpolar matrix.

$$\hat{w} = e^2 \sum_i \frac{3(\vec{r} \cdot \vec{n}_i)(\vec{\rho}_i \cdot \vec{n}_i) - (\vec{r} \cdot \vec{\rho}_i)}{|\vec{R}_i|^3}, \quad (155)$$

where \vec{R}_i is the radius-vector starting from the probe molecule and ending on i -th matrix molecule, $\vec{n}_i = \vec{R}_i / |\vec{R}_i|$, \vec{r} and $\vec{\rho}_i$ are the electron radius-vectors of the chromophore and i -th host molecule, respectively, and e is the elementary electric charge.

Such a model has been known already for half a century but has been applied almost exclusively to calculate solvent shifts. Here the model is expanded in two respects. First, the amorphous structure of the host is taken into account by considering randomly distributed voids — regions where a host molecule is missing. Second, within the same basic formalism of perturbation theory, the influence of the dipole-dipole interaction on the electronic wave functions and as a consequence on the transition dipole moment is evaluated.

Particularly interesting is a relation between the inhomogeneous band width (defined by the standard deviation of the frequency distribution σ_ν) and the standard deviation of the radiative linewidth distribution σ_γ . Details of the derivation are given in the next section. Here we present only the final result

$$\Xi = \frac{\sigma_{\gamma}/\langle\gamma\rangle}{\sigma_{\nu}/(\nu_{vac} - \langle\nu\rangle)} \approx \frac{2^{3/2}(\epsilon - 1)}{\epsilon + 2} \approx 0.9, \quad (156)$$

where $\nu_{vac} - \langle\nu\rangle$ is the mean value of the solvent shift, and $\langle\gamma\rangle$ is the mean value of the radiative linewidth. This relation emphasizes the fundamental unity of the two distributions. It can also be shown, that for every probe molecule the change in its radiative linewidth is not a simple function of its solvent shift and that even for molecules with equal ν there can be a broad distribution of γ (as it is in Fig. 37).

The reason why a lifetime distribution has not been observed previously is that such an effect is difficult to observe with ensemble techniques. Monte Carlo simulations of the decay of an ensemble of molecules with parameters found for terylene in polyethylene show (see Fig. 38) that the ratio of the deviations from a single-exponential fit to the signal is less than 1% when the measurements are performed over a time scale of four lifetimes.

At higher temperature, the distribution of lifetimes will be affected by the mobility of the host molecules and will depend on the ratio of the time scale of the molecular motion to that of the measurement time. Measurements of the lifetime variations on fast time scales might shed additional light onto local structures and dynamics with potential applications even to the study of single biomolecules under physiological conditions. The simple theory outlined above can also be applied to complex bio- and chemical systems where “exact” calculations are clearly beyond modern computing capabilities.

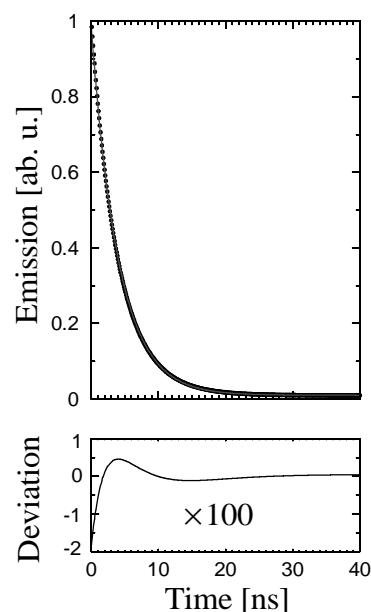


Fig. 38 Monte Carlo simulations of the non exponential decay fitted with a single exponent. The signal-to-background ratio is 100:1. $\langle\Gamma\rangle = 40$ MHz, $\sigma_{\Gamma_{nr}} = 5$ MHz, $\sigma_{\gamma} = 5$ MHz

Details

As it was done in all previous chapters, in this sections we give a more complete account about findings and theoretical concepts briefly described above. The experimental data presented in Fig. 37 and the results of the chapter *Spectral Diffusion in Polyethylene and other Polymers* clearly show that for terrylene molecules embedded in polyethylene there is a linewidth distribution and that the main part of this distribution is not related to the dephasing caused by the matrix dynamics. In other words the distribution is caused by the variations of the life-times of the electronically excited state. The life-time consists of two contributions — radiative and non radiative. The non radiative part can vary because the coupling strength between molecular electronic states and matrix depends on molecular local environments. The second part — the radiative lifetime is related to the oscillator strength of an optical transition. The question is which varies?

The oscillator strength is proportional to the integrated total cross section of an optical transition. This can be determined from absorption measurement but not from excitation spectra where the line amplitude depends on the excitation light intensity, detection efficiency, luminescence quantum yield, etc. Nevertheless an answer to the question can be obtained.

The equation (see Eq. (11) in the section *Molecules Interact with Light*)

$$\Re \propto \sigma_{scat} = \cos^2 \Theta \Upsilon \gamma^2 / [\Gamma_{tot} \cdot (k + \gamma)] \quad (157)$$

tells us that if the angle Θ and the parameter Υ are fixed, the observed line area $A = \Re \Gamma_{tot}$ becomes larger if the radiative linewidth γ becomes larger and smaller if the nonradiative linewidth k increases. This correlations (anti correlations) can be used for the analysis. To be able to combine data measured in different experiments we can normalize the line area of each molecule by the mean value of the line areas of all molecules measured under equal optical alignment. This takes into account not relevant variations in the laser intensity and collection efficiency which are dependent on alignments of the laser beam, the photo multiplier tube, and the collecting optics. Using line areas instead of peak rates for the correlation studies allow us also to disregard possible variations in the dephasing contribution to Γ_{dif} ($\Gamma_{tot} = k + \gamma + \Gamma_{dif}$). $\Re \Gamma_{tot}$ is independent of Γ_{dif} . The varia-

tions of Θ make the correlation less pronounced but can be included in the simulations. The assumption about a random orientation of the probe molecules in a polymer seems very reasonable. Possible variations of the generalized Frank-Condon factor Υ we assume to be small and more important not correlated with the variations of linewidth. Indeed, in the Frank-Condon approximation the radiative rate depends on the electronic transition dipole moment but not on Υ .

Eq. (157) with $\Upsilon = 1$ has been used for the Monte Carlo simulation shown in Fig. 39.

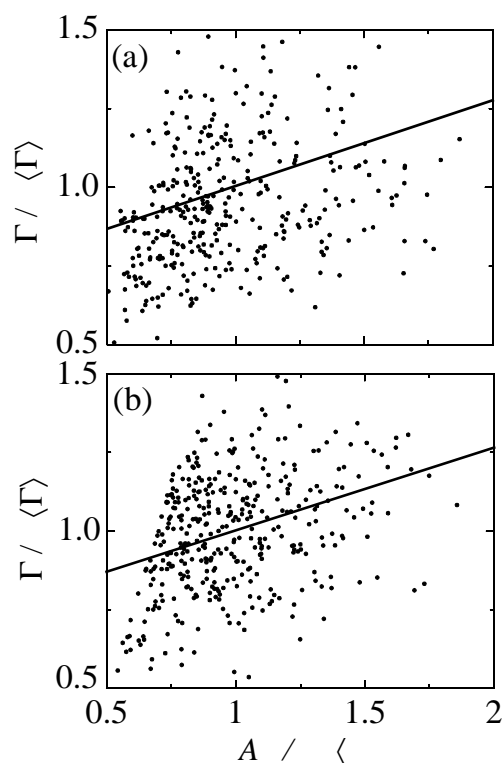


Fig. 39 If the radiative lifetime varies, the broad lines have larger areas and a positive correlation between linewidth and area would arise. A non-radiative lifetime distribution would cause a negative correlation. The correlation is obscured by a random orientation of the transition dipole moments of the terrylene molecules. Nevertheless an analysis of the linewidth — line area correlation clearly shows that the variations arise from approximately equal radiative and non radiative contributions and that the fluorescence quantum yield is approximately 70%. The figure shows (a) data measured at 30 mK, (b) simulation using a Monte Carlo method. The slope, the intercept, and the correlation coefficient are 0.28(4), 0.72(4), and 0.33(3) respectively.

Gaussian radiative and nonradiative linewidth distributions were assumed with the constraints $\sigma_\gamma^2 + \sigma_k^2 = \sigma_\Gamma^2$ and $\langle \gamma \rangle + \langle k \rangle = \langle \Gamma \rangle$, where k is the nonradiative linewidth. The fluorescence quantum yield η was fixed at 0.7, consistent with experimental data [163]. Molecules with $A/\langle A \rangle < 0.5$ do not appear in Fig. 39a because their spectra are too noisy to be fit reliably. To reproduce this in the simulation, the condition $A/\sqrt{\Gamma} > 2$ was used as a criterion for a molecule to be included, which is consistent with the upper bound of 7% for the error in the linewidth that was used for screening the data for Fig. 39a. This choice can be justified as follows. First, we write

$$\frac{A}{\sqrt{\Gamma}} \equiv \mathfrak{R} \sqrt{\Gamma} = \left(\frac{\delta_v}{\pi} \right)^{1/2} \frac{4\sigma_{sig}}{\sigma_\Gamma/\Gamma}. \quad (158)$$

The second equality is obtained from the estimate of the linewidth error σ_Γ [164] in the case when the experimental noise is determined by the background signal (as it was in the experiment)

$$\frac{\sigma_\Gamma}{\Gamma} = \frac{4\sigma_{sig}}{R} \sqrt{\frac{\delta_v}{\pi\Gamma}}, \quad (159)$$

where σ_{sig} is the standard deviation of the signal from the mean value, δ_v is the laser frequency step size, \mathfrak{R} is the line amplitude. In the experiment, the frequency step $\delta_v = 2$ MHz. The background signal and hence the noise was equal for all molecules. To relate the experimental σ_{sig} with simulations, we can consider the brightest molecules for which in the simulations $\mathfrak{R} \approx 1$. In the experiment such molecules had $\sigma_{sig}/\mathfrak{R} = 0.05$ and thus for the simulations we set $\sigma_{sig} = 0.05$. If the error in the linewidth is 7% then

$$\frac{A}{\sqrt{\Gamma}} = \left(\frac{2}{\pi} \right)^{1/2} \frac{4 \cdot 0.05}{0.07} \approx 2 \quad (160)$$

and the above stated criteria follows.

In a set of simulations, σ_γ/σ_k was varied until the correlation coefficient, the slope, and the intercept for a linear regression matched the features of the measured scatter plot. This yielded a value of $\sigma_\gamma/\sigma_k \approx 1$. Finally, we conclude that $\sigma_\gamma/\langle\gamma\rangle \approx 16\%$.

In the first part of this chapter it was shown that a variation of macro characteristic properties can not explain the observations. And a microscopic theory of interaction between electromagnetic radiation and a probe molecule embedded in a solid matrix is needed.

While the interaction of electromagnetic fields with a simple quantum system in a vacuum is understood with great detail [13], the situation is much more obscure when the atom or molecule is surrounded by many others. Difficulties arise because the structure of electromagnetic field in a dense media becomes very complicated. One way to approach the problem is to consider not the averaged macroscopic fields but so-called local fields, fields which take into account the effect of surroundings. Accept for the local field factor

and an obvious replacing the speed of light in vacuum by its value in a medium, the problem was treated in a manner analogous to that in vacuum.

Instead of a quasi classical concept of local fields, a consistent microscopic picture of local effects would be a major step forward. Single-molecule spectroscopy (SMS) is the perfect technique for making this step, since it provides access to the structure of the local environment. SMS can be used to gain some insight into the influence of local environment on radiative life times of a chromophore impurity molecule embedded in an amorphous solid.

The model which was already briefly described in the first part of this chapter is show in Fig.40. This combined system can be thought of as a “supermolecule,” whose wave function representing both the impurity and its local environment is localized mostly in the core region. The unperturbed transition dipole moment $-e\langle\phi_0|\vec{r}|\phi_1\rangle = \vec{\mu}$, where $|\phi_k\rangle$ are the unperturbed wave functions of the probe molecule and \vec{r} is the electron radius-vector, which is assumed to be parallel to z-axis. The unperturbed energies of the probe molecule are denoted by E_k ($E_0 = 0$).

The chromophore volume is defined by a radius R_{min} . This volume is not available for polymer molecules. The polymer is made up of non interacting monomer molecules with one ground $|\psi_g\rangle$ and three excited states $|\Psi_m\rangle$ ($m = 1, 2, 3$). The excited states have the same energy F and the same value of the transition dipole moments $\vec{d}_m^i = -e\langle\psi_g|\vec{\rho}_i|\Psi_m\rangle$. The direction of the three moments are ortogonal to each other and thus the monomer polarizability tensor is diagonal with equal eigen values. When densely packed, the monomers have a density n_s .

The interaction between the probe molecule and the monomers is taken to have the form of a dipole-dipole interaction Eq. (155). The perturbed wave functions read

$$|\widehat{\phi_0\Psi_g}\rangle = |\phi_0\Psi_g\rangle - \sum_i \sum_{k,m} |\phi_k\Psi_m^i\rangle \frac{\langle\phi_k\Psi_m^i|\hat{W}|\phi_0\Psi_g^i\rangle}{F + E_k} \quad (161)$$

and

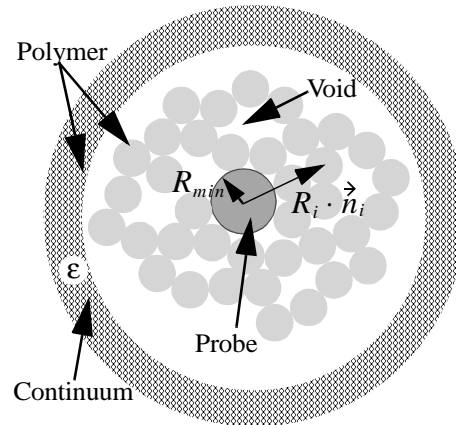


Fig. 40 A model for the probe molecule embedded in a polymer.

$$|\widehat{\varphi}_1 \widehat{\Psi}_g\rangle = |\varphi_1 \Psi_g\rangle - \sum_i \sum_{k,m} |\varphi_k \Psi_m^i\rangle \frac{\langle \varphi_k \Psi_m^i | \widehat{W} | \varphi_1 \Psi_g^i \rangle}{F + E_k - E_1}, \quad (162)$$

With these wave functions the perturbed transition energy and transition dipole moments can be evaluated. The transition dipole moment of the combined system (probe molecule + polymer) is

$$\vec{\mu}_{eff} = -e \langle \widehat{\varphi}_0 \widehat{\Psi}_g | \vec{r} + \vec{\rho}_i | \widehat{\varphi}_1 \widehat{\Psi}_g \rangle, \quad (163)$$

where $|\widehat{\varphi}_0 \widehat{\Psi}_g\rangle$ and $|\widehat{\varphi}_1 \widehat{\Psi}_g\rangle$ are the wave functions expressed by Eq. (161) whose substitution in Eq. (163) gives

$$\vec{\mu}_{eff} = \vec{\mu} - \sum_i \sum_m \frac{3(\vec{\mu} \cdot \vec{n}_i)(\vec{n}_i \cdot \vec{d}_m^i) - (\vec{\mu} \cdot \vec{d}_m^i) \vec{n}_i}{R_i^3} \vec{d}_m^i \left[\frac{1}{F - E_1} + \frac{1}{F + E_1} \right]. \quad (164)$$

Because three vectors \vec{d}_m^i ($m = \{1, 2, 3\}$) is a full basis vector systems, for any vector \vec{a} the equality $\sum_m (\vec{a} \cdot \vec{d}_m^i) \vec{d}_m^i = \vec{a} d^2$ holds. This equality helps to simplify Eq. (164) as follows

$$\vec{\mu}_{eff} = \vec{\mu} - \delta \vec{\mu} = \vec{\mu} - \sum_{i=1}^N \alpha \frac{3(\vec{\mu} \cdot \vec{n}_i) \vec{n}_i - \vec{\mu}}{R_i^3}, \quad (165)$$

where $\alpha = 2Fd^2/(F^2 - E_1^2)$, and θ_i is the angle between vectors $\vec{\mu}$ and \vec{n}_i .

The radiative linewidth is proportional to the square of $\vec{\mu}_{eff}$. Within an approximation $\mu^2 - 2(\vec{\mu}, \delta \vec{\mu}) + (\delta \mu)^2 \approx \mu^2 - 2(\vec{\mu}, \delta \vec{\mu})$ the expression for γ reads

$$\gamma \propto \gamma_{vac} - \gamma_{vac} \sum_{i=1}^N 2\alpha \frac{3 \cos^2 \theta_i - 1}{R_i^3}, \quad (166)$$

where $\gamma_{vac} \propto \mu^2$ is the radiative linewidth in vacuum.

If an external uniform field is applied to the sample, the field acting on the core region of the super molecule is equal to the field in the center of a spherical cavity in a dielectric media with a uniform polarization $P = \epsilon_0(\epsilon - 1)E_{int}$, where E_{int} is the macroscopic internal electric field (see *Molecules Interact with Light*). The part of solvent where $R_i \geq R_{max}$ can be treated in the dielectric continuum approximation. The field inside the cavity is

$$E_{loc} = E_{int} + \frac{P}{3\epsilon_0} = E_{int} \left(1 + \frac{\epsilon - 1}{3} \right) = \frac{\epsilon + 2}{3} E_{int} = L E_{int} \quad (167)$$

The local field correction L effects the interaction strength of the super molecule with all kinds of external electromagnetic fields and as a consequence it effects the spontaneous transition rate (depending on the square of the coupling constant with the field modes in a large cavity filled with the dielectric). Thus

$$\gamma = \left(\frac{\mathbf{v}}{\mathbf{v}_{vac}} \right)^3 \frac{\epsilon^{1/2} (\epsilon + 2)^2}{9} \left(1 - 2\alpha \sum_{i=1}^N \frac{3 \cos \theta_i^2 - 1}{R_i^3} \right) \cdot \gamma_{vac}, \quad (168)$$

where an extra factor $\epsilon^{1/2}$ takes into account that the speed of light in a dielectric is different from that in vacuum and the factor $(\mathbf{v}/\mathbf{v}_{vac})^3$ takes into account a change of the transition frequency (see below).

If the distribution of one solvent molecule in space is uniform, $\langle 3 \cos \theta_i^2 - 1 \rangle = 0$. This results in

$$\langle \gamma \rangle = \left(\frac{\mathbf{v}}{\mathbf{v}_{vac}} \right)^3 \frac{\epsilon^{1/2} (\epsilon + 2)^2}{9} \cdot \gamma_{vac} \quad (169)$$

The change of the transition frequency is the second order effect for which a standard text book expression reads

$$\mathbf{v} = \mathbf{v}_{vac} + \frac{1}{h} \sum_{m=1}^5 \left[\frac{|\langle \phi_0 \Psi_g | \hat{w} | \phi_1 \Psi_m \rangle|^2}{F + E_1} - \frac{|\langle \phi_1 \Psi_g | \hat{w} | \phi_0 \Psi_m \rangle|^2}{F - E_1} \right], \quad (170)$$

where for simplicity only the two lowest electronic states of the probe molecule are taken into account and the two terms in Eq. (170) are the corresponding changes of the two lowest energies. After a simple math

$$\mathbf{v} = \mathbf{v}_{vac} - \frac{2E}{h(F^2 - E_1^2)} \sum_{m=1}^3 |\langle \phi_0 \Psi_g | \hat{w} | \phi_1 \Psi_m \rangle|^2. \quad (171)$$

In the explicit expression for the sum we first neglect the cross term

$$\sum_{i,j} \sum_{m=1}^3 \frac{3(\vec{\mu} \cdot \vec{n}_i)(\vec{n}_i \cdot \vec{d}_m) - (\vec{\mu} \cdot \vec{d}_m)}{R_i^3} \cdot \frac{3(\vec{\mu} \cdot \vec{n}_j)(\vec{n}_j \cdot \vec{d}_m) - (\vec{\mu} \cdot \vec{d}_m)}{R_j^3}$$

$$\approx \sum_i \sum_{m=1}^3 \left[\frac{3(\vec{\mu} \cdot \vec{n}_i)(\vec{n}_i \cdot \vec{d}_m) - (\vec{\mu} \cdot \vec{d}_m)}{R_i^3} \right]^2 \quad (172)$$

and then using \vec{d}_m as a basis simplify Eq. (172)

$$\sum_{m=1}^3 \frac{[3(\vec{\mu} \cdot \vec{n}_i)(\vec{n}_i \cdot \vec{d}_m) - (\vec{\mu} \cdot \vec{d}_m)]^2}{R_i^6} = \frac{d^2}{R_i^6} ([3(\vec{\mu} \cdot \vec{n}_i)\vec{n}_i - \vec{\mu}] \cdot [3(\vec{\mu} \cdot \vec{n}_i)\vec{n}_i - \vec{\mu}]) = \frac{d^2 \mu^2}{R_i^6} (3 \cos^2 \theta_i + 1) \quad (173)$$

to obtain finally

$$\nu = \nu_{vac} - \alpha \left\{ \frac{\mu^2 E_1}{hF} \right\} \cdot \sum_i \frac{3 \cos^2 \theta_i + 1}{R_i^6}, \quad (174)$$

This is the well-known dispersive solvent shift [165, 166]. Within the approximation of uncorrelated distribution of the solvent molecules we can add contribution of all solvent molecules to obtain for the mean frequency

$$\langle \nu \rangle \approx \nu_{vac} - \alpha \left\{ \frac{\mu^2 E_1}{hF} \right\} \cdot \frac{8\pi n_{pol}}{3R_{min}^3}, \quad (175)$$

where n_{pol} is the density of solvent molecules².

The factor in curly brackets (see Eqs. (174, 175)) is the part mainly depending on higher electronic states. When they are included, this factor is a sum of terms containing the impurity polarizability, the square of the transition dipole moment μ^2 , and the effective chromophore excitation energy \bar{E} which should be used instead of E_1 [165]. In fact This factor is treated as a parameter below that eventually cancels.

To analyze the width of γ and ν distributions it is convenient to consider an effective interaction between voids and the impurity molecules, which can be described by Eq. (155) with opposite sign and R_i understood as the distance to the i -th void. When densely packed, the host molecules have a density n_s . The concentration of voids $n_v \ll n_s$ and $n_{pol} = n_s - n_v$. The result of addition of the contributions can be evaluated using the *cen-*

2. One can derive Eq. (154) from Eq. (175) assuming $R_{min}^{-3} \propto n_{pol}$. With an assumption $R_{min}^{-3} = \text{const}$ the estimate on Page 98 would change to $\sigma_\gamma / \langle \gamma \rangle \leq 7\%$ if only the variation of ϵ causes the distribution of γ . This is still too small in comparison with 16% obtained in our experiments.

tral limit theorem. First we calculate the mean and the variance for on contribution. The variance of the radiative linewidth σ_γ^2 and that of the transition frequency σ_ν^2 are equal to the number of voids multiplied by the variances calculated with the single void distribution function.

We begin with σ_γ^2 . In the experiment under consideration, the transition frequencies were almost equal for all measured molecules and thus ν/ν_{vac} was a unimportant constant which can be disregarded. In a general case this factor can be taken into account by normalization of each γ by the cube of the corresponding transition frequency. The variance is defined by

$$\sigma_\gamma^2 = \langle (\gamma - \langle \gamma \rangle)^2 \rangle \quad (176)$$

To obtain the mean of $(3 \cos \theta_i^2 - 1)^2$, we should calculate the integral

$$\left\langle \frac{(3 \cos \theta^2 - 1)^2}{R^6} \right\rangle = \frac{1}{V} \int_{R_{min}}^{R_{max}} \left(\int_0^\pi \left(\int_0^{2\pi} \frac{(3 \cos \theta^2 - 1)^2}{R^6} d\phi \right) \sin \theta d\theta \right) R^2 dR = \frac{16\pi}{15VR_{min}^3}, \quad (177)$$

where the condition $R_{max} \gg R_{min}$ and $V \approx 4\pi R_{max}^3/3$ have been used. Thus for a single void

$$\sigma_\gamma^2 = \langle \gamma \rangle^2 \cdot (2\alpha)^2 \cdot \frac{16\pi}{15VR_{min}^3}. \quad (178)$$

The relative standard deviation of the γ distribution is

$$\frac{\sigma_\gamma}{\langle \gamma \rangle} = 2\alpha \sqrt{n_\nu V \cdot \frac{16\pi}{15VR_{min}^3}} = 8\alpha \sqrt{\frac{\pi n_\nu}{15R_{min}^3}} \quad (179)$$

In a similar way

$$\left\langle \frac{(3 \cos \theta^2 + 1)^2}{R^{12}} \right\rangle = \frac{1}{V} \int_{R_{min}}^{R_{max}} \left(\int_0^\pi \left(\int_0^{2\pi} \frac{(3 \cos \theta^2 + 1)^2}{R^{12}} d\phi \right) \sin \theta d\theta \right) R^2 dR = \frac{32\pi}{15VR_{min}^9} \quad (180)$$

and for a single void

$$\sigma_\nu^2 = \left[\alpha \frac{\mu^2 E_1}{hF} \right]^2 \frac{32\pi}{15VR_{min}^9} \quad (181)$$

With a help of Eq. (175) the relative standard deviation of the solvent shift distribution can be written as

$$\frac{\sigma_v}{\nu_{vac} - \langle \nu \rangle} = \frac{1}{n_s - n_v} \cdot \sqrt{\frac{3n_v}{10\pi R_{min}^3}} \quad (182)$$

The Clausius-Mossotti equation [20] in our notations reads

$$\alpha(n_s - n_v) = \frac{3}{4\pi} \cdot \frac{\epsilon - 1}{\epsilon + 2} . \quad (183)$$

This allow us to obtain a relation between relative with of the radiative linewidth distribution and the relative width of the solvent shift distribution which depends only on the relative dielectric constant ϵ , that is Eq. (156).

The estimate of the left hand side of Eq. (156) which is based on the following experimental data — $\sigma_\gamma \approx 4.7$ MHz , $\gamma = 28$ MHz , $\nu_{vac} = 19230$ cm⁻¹ [Ref], $\langle \nu \rangle = 17600$ cm⁻¹ , and $\sigma_v = 185$ MHz [163] gives $\Xi = 1.5$. The evaluation of the right hand side of Eq. (156) gives $\Xi = 0.9$ (for $\epsilon = 2.3$). This theoretical estimate for Ξ can be increased by van der Waals attraction forces which reduce the void concentration in the first solvent shell. This shell contributes to $\nu_{vac} - \langle \nu \rangle$ a value determined by the Eq. (174) but does not effect the ratio σ_γ/σ_v (since σ_γ and σ_v are both proportional to $\sqrt{n_v}$) and does not effect $\langle \gamma \rangle$. All this can be taken into account by introducing a radius \tilde{R}_{min} and assuming that there is no fluctuations in the solvent shell configuration if $R_{min} < R < \tilde{R}_{min}$ but a small change of the solvent density in this region is negligible. In this case the right hand side of Eq. (156) is multiplied by $(\tilde{R}_{min} / R_{min})^3$ [167].

A brief inspection of Eqs. (168) and (174) may give the impression that γ and the location of an impurity in the inhomogeneous band should be strongly correlated. Though there is partial correlation, γ is not a simple function of ν . This is shown in Fig. 41 where a Monte Carlo simulation of a scatter plot for $\gamma / \langle \gamma \rangle$ vs. $\nu / \langle \nu \rangle$ is shown. Thus, though all 380 molecules had almost equal transition frequencies, they could nevertheless have a distribution of lifetimes. In Fig. 41 we have not accounted for the well-known ν^3 dependence [13] on γ , which would cause a stronger positive correlation [142].

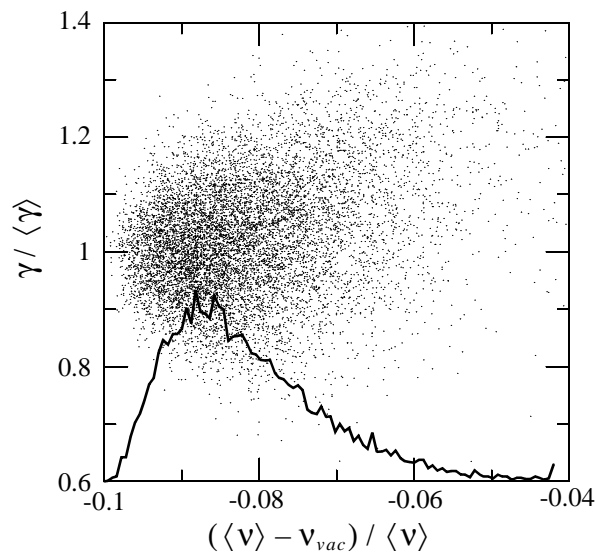


Fig. 41 This figure shows a Monte Carlo simulation of a scatter plot for $\gamma / \langle \gamma \rangle$ vs. $\delta \nu / \langle \nu \rangle$. The solid line is the inhomogeneous band. The radiative lifetime found from the data ($T_1 / \phi_f \approx 5.5$ ns) and the value $\mu^2 / (h\nu) = 30 \text{ \AA}^3$ have been used. $\alpha = 10 \text{ \AA}^3$ (reasonable for a medium-sized n-alkane), $\bar{E} / F = 1$, and $R_{min} = 0.6$ nm, were also assumed. Since crystalline PE is $\sim 20\%$ denser than amorphous PE, the density of voids $n_v = 0.2n_s$, where n_s is the density of packed host molecules. From the Clausius-Mossotti equation the densities $n_v = 1.8 \text{ nm}^{-3}$ and $n_s = 9 \text{ nm}^{-3}$ were found (assuming $\epsilon = 2.3$).

VIII. Perspectives

In my opinion, the development of SMS will follow three main directions: 1) quantum optics, where an ability to work with a single quantum system can be vital; 2) solid state physics and technology, where in the remote future single molecules might be used for data storage and data evaluation; 3) bio- and chemical physics, where single molecules are very promising as nano sensors. These are only code names and all the three require an interdisciplinary approach. Some suggestions are listed below.

Quantum optics. One disadvantage of SMS in comparison with, for example, single ions in an electromagnetic trap, is that the 0-0 emission of single molecules is not detectable because strong stray and scattered laser light has the same frequency as the 0-0 line. But estimations show that careful design can significantly improve the situation and the laser light falling onto a photo detector can be several times weaker than the resonance single molecule emission. If such conditions were achieved, this would open many options for quantum optical experiments. Among them: the direct detection of the Mollow triplet, a splitting of the resonance line in an intense electromagnetic field; a single-molecule Young's experiment, a quantum mechanical analog of the classical Young's experiment but with two single molecules used instead of two slits; a single molecule laser, a laser where the active medium consists of only one molecule.

Solid state physics and technology. Recent progress in the understanding of the physics of amorphous solids has led to a phenomenological theory of two-level systems. Presented results indicate that information about a particular TLS is accessible by monitoring the transition frequency of a single molecule. Single molecule technique can help to develop a microscopic theory of these structures. Especially interesting effects are expected when the whole system is of a nanometer size. If such a scheme turns out to be feasible, this will have a fundamental significance as well as a practical value. The excited state lifetime of a TLS can be very long (up to months) and one can think of using "TLS-single molecule" combinations for data storage and as components of a quantum computer [168]. Chemical synthesis of structures with desirable TLS parameters is probably a key to a success of this scheme.

Bio- and chemical physics. In a large ensemble of molecules, fluctuations are small but their role can be far more important than just a cause for a noise in experimental data. Crystal grow and chemical reactions are driven by fluctuation. After all, life on Earth is probably just a fluctuation in the Universe. On the single-molecule level, these fluctuations are the most pronounced phenomenon and can be a subject of thorough investigations. Single molecules could reveal the origin of non exponential kinetics, and shed extra light on protein folding and on phase transitions. For example, green fluorescing proteins can be used as labels in biologically relevant molecules. A combination with near-field techniques can also add high spatial resolution. Though most biologically relevant studies imply experiments at room temperature, some techniques developed for low temperatures are still applicable. For example, the intensity-time-frequency correlation technique could be applied to enhance time resolution and radiative lifetimes could be used for structural analysis.

IX. Acknowledgments

I am pleased to acknowledge the continuing interest and support which I have received from Professor Urs P. Wild during all the time I have spent in ETH Zürich. The author is also grateful to Daniel Walser, Elizabeth Donley, and Thomas Nonn for their hard and innovative work in the laboratory which sometimes continued past midnight. Robin Purchase is acknowledged for a careful proof reading of the manuscript. I am grateful to all other members of the Wild-group for providing friendly and stimulating environment. Special thanks to Bruno Lambilot and his assistance in many cases which are too numerous to be listed here. This work was funded by the ETH Zürich and Swiss National Science Foundation.

References

1. An issue of *Science* **283** (1999) with review articles by W. E. Moerner & M. Orrit p. 1670, S. Weiss p. 1676, J. K. Grimzewski & C. Joachim p. 1683, and A. D. Mehta, et al. p. 1689 was devoted to single molecules.
2. P. Tamarat, A. Maali, B. Lounis, M. Orrit, *J. Phys. Chem. A* **104** (2000) 1.
3. T. Plakhotnik, E.A. Donley, U.P. Wild, *Annu. Rev. Phys. Chem.* **48** (1997) 181.
4. T. Basché, W. E. Moerner, M. Orrit, U. P. Wild, *Single Molecule Optical Detection and Imaging* (VCH, Weiheim, 1996).
5. Basché Th, Bräuchle C. 1996. *Ber. Bunsenges. Phys. Chem.* 100: 1269-79
6. J. L. Skinner, W. E. Moerner 1996. *J. Phys. Chem.* 100: 13251-62.
7. Kador L. 1995. *Phys. Stat. Sol. (b)* 189: 11-36
8. M. Orrit, J. Bernard, R. Brown, B. Lounis (1996). In *Progress in Optics*, ed. E Wolf, XXXV: 61-144. Amsterdam: Elsevier.
9. X. S. Xie, J. K. Trautman, *Annu. Rev. Phys. Chem.* **49** (1998) 441.
10. W. E. Moerner, L. Kador 1989. *Phys. Rev. Lett.* 62: 2535-38.
11. M. Orrit, J. Bernard, *Phys. Rev. Lett.* **65** (1990) 2716-19.
12. T. Plakhotnik, D. Walser, M. Pirotta, A. Renn. U.P. Wild, *Science* **271** (1996) 1703.
13. L. Mandel, E. Wolf, *Optical coherence and quantum optics* (Cambridge University Press, Cambridge, 1995).
14. H. J. Kimble, M. Dagenais, L. Mandel, *Phys. Rev. Lett.* **39** (1977) 619.
15. F. Diedrich, H. Walther, *Phys. Rev. Lett.* **58** (1987) 203.
16. Th. Basché, W.E. Moerner, M. Orrit, H. Talon, *Phys. Rev. Lett.* **69** (1992) 1516.
17. S. Kummer, S. Mais, Th. Basché, *J. Phys. Chem.* **99**, 17078 (1995).
18. S. Nie, S. R. Emory, *Science* **275** (1997) 1102.
19. K. Kneipp, Y. Wang, H. Kneipp, L. T. Perelman, I. Itzkan, et al. *Phys. Rev. Lett.* **78** (1997) 1667.

References

20. J. D. Jackson, *Classical Electrodynamics*, 2 ed. (John Wiley & Sons, New York, 1975).
21. K. K. Rebane. *Impurity Spectra of Solids*. 1970 New York: Plenum Press.
22. J. M. Fernández-Sánchez, S. Montero, . *J. Chem. Phys.* **90** (1989) 2909-14.
23. T. Schmidt, G. J. Schütz, W. Baumgartner, H. J. Gruber, H. Schindler, *Proc. Natl. Acad. Sci. USA* **93** (1996) 2926.
24. E. Betzig, R. J. Chichester, *Science* **262** (1993) 1422-28.
25. R. A. Keller, W. P. Ambrose, P. M. Goodwin , J. H. Jett , J. C. Martin, M. Wu , *Appl. Spectr.* **50** (1996) 12A-32A.
26. P. Suppan, *J. Photochem. Photobiol. A* **50** (1990) 293-330.
27. W. E. Moerner, T. P. Carter, *Phys. Rev. Lett.* **59** (1987) 2705-08.
28. J. B. Birks, *Photophysics of Aromatic Molecules*. 1970 London: Wiley.
29. S. L. Murov, I. Carmichael, G. L. Hug, *Handbook of Photochemistry*. 1993 New York: Marcel Dekker. 2nd ed.
30. C.J.F. Böttcher, *Theory of electric polarization*. 1973 Amsterdam: Elsevier. pp. 159-73. Vol 1. 2nd ed.
31. W. E. Moerner (ed.), *Persistent Spectral Hole Burning: Science and Applications*, (Springer, Berlin, 1988).
32. P. Tchénio, A. B. Myers, W. E. Moerner, *J. Phys. Chem.* **97** (1993) 2491-93
33. P. Tchénio, A. B. Myers, W. E. Moerner, *Chem. Phys. Lett.* **213** (1993) 325-32
34. A. B. Myers, P. Tchénio, W. E. Moerner, *J. Lumin.* **58** (1994) 161-67
35. A. B. Myers, P. Tchénio, M. Z. Zgierski, W. E. Moerner, *J. Phys. Chem.* **41** (1994) 10377-90
36. L. Fleury, P. Tamarat , B. Lounis, J. Bernard , M. Orrit, *Chem. Phys. Lett.* **236** (1995) 87-95.
37. T. Nonn, T. Plakhotnik. Fluorescence excitation spectroscopy of vibronic transitions in single molecules. *Chem. Phys. Lett.* **336** (2001) 97.
38. D. W. Pohl , D. Courjon , eds. *Near Field Optics*. 1993 Dordrecht: Kluwer Academic 418 pp.

References

39. W. E. Moerner, T. Plakhotnik, T. Irgartinger, U. P. Wild, D. W. Pohl, B. Hecht, .
Phys. Rev. Lett. **73** (1994) 2764-67.
40. T. Plakhotnik, *Optics and Spectroscopy* **79** (1995) 688-95.
41. J. Köhler, J. A. J. M. Disselhorst, M. C. J. M. Donckers, E. J. J. Groenen, j.
Schmidt, W. E. Moerner, *Nature* **363** (1993) 242-44.
42. J. Wrachtrup, C. von Borczyskowski, J. Bernard, M. Orrit, R. Brown, *Nature* **363**
(1993) 244-45.
43. R. Brown, J. Wrachtrup, M. Orrit, J. Bernard, C. von Borczyskowski, *J. Chem. Phys.*
100 (1994) 7182-91.
44. J. Köhler, A. C. J. Brouwer, E. J. J. Groenen , J. Schmidt *Chem. Phys. Lett.* **228**
(1994)47-52.
45. J. Köhler, A. C. J. Brouwer, E. J. J. Groenen , J. Schmidt . *Science.* **268** (1995) 1457-
60.
46. J. Wrachtrup J, C. von Borczyskowski, J. Bernard, M. Orrit, R. Brown *Phys. Rev.*
Lett. **71** (1993)3565-68.
47. J. Wrachtrup, C. von Borczykowski, J. Bernard, R. Brown, M. Orrit, *Chem. Phys.*
Lett. **245**, 262 (1995).
48. J. L. Black, B. I. Halperin, *Phys. Rev. B* **16** (1977) 2879-95.
49. B. Colding, J. E. Graebner, *Phys. Rev. Lett.* **37** (1976) 852.
50. I. D. Abella, N.A. Kurnit, S. R. Hartmann, *Phys. Rev.* **141** (1966) 391.
51. W. H. Hesselink, D. A. Wiersma. *Phys. Rev. Lett.* **43** (1979) 1991.
52. W. A. Phillips, *Proc. Roy. Soc. Lond. A*, **319** (1970) 565.
53. P. W. Anderson, B. I. Halperin, C. M. Varma, *Philos. Mag.* **25**, 1 (1972).
54. W. A. Phillips, *J. Low Temp. Phys.* **7** (1972) 351-60.
55. W. A. Phillips , ed. 1981. *Amorphous Solids: Low Temperature Properties*. Berlin:
Springer.
56. J. R. Klauder, P. W. Anderson, *Phys. Rev.* **125**, 912 (1962).
57. H. Maier, D. Haarer, *J. Lumin.* **64** (1995) 87-93 .
58. K. Fritsch, J. Friedrich, B. M. Kharlamov, *J. Chem. Phys.* **105** (1996) 1798.

References

59. T. L. Reinecke, *Sol. Stat. Com.* **32**, 1103 (1979).
60. P. Esquinazi (editor) *Tunneling systems in amorphous and crystalline solids*, 1998 Springer, Berlin.
61. A. M. Boiron, P. Tamarat, B. Lounis, R. Brown, M. Orrit, *Chem. Phys.* **247** (1999) 119.
62. D. S. Sivia, *Data Analysis: A Bayesian tutorial*, 1996 Oxford, New York.
63. S. L. Meyer, *Data analysis for scientists and engineers*, 1992 Wiley, New York.
64. T. Basché, W. E. Moerner . *Nature* **355** (1992) 335-37
65. S. A. Empedocles, D. J. Norris, M. G. Bawendi, *Phys. Rev. Lett.* **77**, 3873 (1996).
66. T. Plakhotnik, D. Walser, *Phys. Rev. Lett.* **80** (1998) 4064.
67. T. Plakhotnik, *Phys. Rev. B* **59** (1999) 4658.
68. A. Zumbusch, L. Fleury, R. Brown, J. Bernard, M. Orrit, *Phys. Rev. Lett.* **70** (1993) 3584-87.
69. L. Fleury, A. Zumbusch, M. Orrit, R. Brown, J. Bernard, *J. Lumin.* **56** (1993) 15-28.
70. A. Suárez, R. Silbey, *Chem. Phys. Lett.* **218** (1993) 445.
71. R. Kubo, in *Fluctuation, Relaxation and Resonance in Magnetic Systems*, edited by D. Ter Haar (Oliver and Boyd, Edinburgh, 1962).
72. E. Geva, J. L. Skinner, *J. Phys. Chem. B* **101** (1997) 8920.
73. E. A. Donley, T. Plakhotnik *J. Chem. Phys.* (2000) in print.
74. D. Dab, A. Heuer, R. Silbey, *J. Lumin.* **64** (1995) 95.
75. C. Cohen-Tannoudji, J. Dupont-Roc, G. Grynberg, *Atom-Photon Interactions* (Wiley, New York, 1992).
76. A. Abragam, *The principles of nuclear magnetism*, Ch. 10. (Oxford, London 1961).
77. R. Kubo, *Adv. Chem. Phys.* **15**, 101 (1969).
78. R. M. Shelby, C. B. Harris, P. A. Cornelius, *J. Chem. Phys.* **70**, 34 (1979).
79. P. D. Reilly, J. L. Skinner, *J. Chem. Phys.* **101**, 959 (1994).
80. L. Fleury, R. Brown, J. Bernard, M. Orrit, *Laser Physics* **5**, 648 (1995).
81. P. Hu, S. R. Hartmann, *Phys. Rev. B*, **9**, 1 (1974).

References

82. P. Hu, L. R. Walker, *Phys. Rev. B*, **18**, 1300 (1978).
83. K. Barth, W. Richter, *Mol. Cryst. Liq. Cryst.* **283** (1996) 225.
84. W. E. Moerner, T. Plakhotnik, T. Irngartinger, M. Croci, V. Palm, U. P. Wild, *J. Phys. Chem.* **98** (1994) 7382-89.
85. P. W. Anderson, *J. Phys. Soc. Jpn.* **9** (1954) 316.
86. R. Kubo, *J. Phys. Soc. Jpn.* **9** (1954) 935.
87. W.H. Hesselink, D.A. Wiersma, *J. Chem. Phys.* **73**, 648 (1980).
88. S. Voelker, R.M. MacFarlane, J.H. Van der Waals, *Chem. Phys. Lett.* **53**, 8 (1978).
89. R. Brout, W. Viscshler, *Phys. Rev. Lett.* **9** (1962) 54.
90. W. Eisenmenger, A. A. Kaplynskii, (editors), *Nonequilibrium phonons in nonmetallic crystals*, 1986 North Holland, Amsterdam.
91. D. E. McCumber, M. D. Sturge, *J. Appl. Phys.* **34** (1963) 1682.
92. G. Gradl, B. E.Kohler, C. Westerfield, *J. Lumin.* **45** (1990) 83.
93. T. Plakhotnik, D. Walser, A. Renn, U. P.Wild, *Chem. Phys. Lett.* **262** (1996) 379.
94. L. A. Rebane, A. A. Gorokhovskii, J. V. Kikas, *Appl. Phys. B* **29** (1982) 235.
95. T. Plakhotnik, W. E. Moerner, V. Palm, U. P. Wild, *Opt. Commun.* **114** (1995) 83-88.
96. D. Walser, T. Plakhotnik, A. Renn, U. P. Wild, *Chem. Phys. Lett.* **270** (1997) 16.
97. J. M. Pfotenhauer, R. J. Donnelly, *Adv. Heat Transfer* **17**, 65 (1985).
98. A. Kawski, Z. Gryczynski, *Z. Naturforsch.* **41a** (1986) 1195; *ibid.* **42a** (1987) 617.
99. W. Liptay, R. Wortmann, R. B'ohm, N. Detzer, *Chem. Phys.* **120** (1988) 439.
100. R. Wortmann, K. Elich, W. Liptay, *Chem. Phys.* **124** (1988) 395.
101. Y. B. Levinson, p. 91. in *Nonequilibrium phonons in nonmetallic crystals*, W. Eisenmenger, A. A. Kaplynskii, (editors) 1986 North Holland, Amsterdam.
102. B. Baumgartner, M. Engelhardt, K. F. Renk, *Phys. Rev. Lett.* **47** (1981) 1403.
103. D. V. Kazakovtsev, I. B. Levinson, *Sov. Phys. JETP* **61** (1985) 1318.
104. J. C. Hensel, R. C. Dynes, *Phys. Rev. Lett.* **39** (1977) 969.
105. D. Greig, *Progr. in Solid State Chemistry*, **1** (1964) 175.
106. R. Berman, E. L. Foster, *Proc. Roy. Soc. (London)* **A237** (1956) 344.

References

107. R. Berman, P. T. Nettle, F. W. Seard, A. N. Spencer, R. W. H. Stevenson, J. M. Ziman, *Proc. Roy. Soc. (London)*, **A253** (1959) 403.
108. *Thermal conductivity-Nonmetallic Solids*, Y. S. Touloukian, E. H. Buyco, eds., *Thermophysical properties of matter*, Plenum: New York, 1970; Vol. 2.
109. J. Timmermans, *Physico-chemical Constants of Pure Organic Compounds*, Elsevier: New York, 1950.
110. A. I. Kitaigorodsky, *Molecular Crystals and Molecules*, Academic Press: New York, 1973.
111. A. A. Maksimov, Tartakovskii, *Phys. Stat. Sol. (b)* **107** (1981) 55; *Sov. Phys. JETP Lett.* **42** (1985) 569.
112. K. Kawasaki, H. Nakamura, M. Matsuura, p. 1309, *Phonons 89*, S. Hunklinger, W. Ludwig, G. Weiss, eds. World Scientific: Singapore, 1989.
113. Y. Kogure, T. Mughishima, Y. Hiki, *J. Phys. Soc. Japan* **55** (1986) 3469.
114. T. Mughishima, Y. Kogure, Y. Hiki, K. Kawasaki, H. Nakamura, *J. Phys. Soc. Japan* **57** (1988) 2069.
115. L. R. Narasimhan, K. A. Littau, D. W. Pack, Y. S. Bai, A. Elschner, M. D. Fayer, *Chem. Rev.* **90**, 439 (1990).
116. A. G. Redfield, *IBM J. Res. Dev.* **1**, (1957) 19.
117. P. de Bree, D. A. Wiersma, *J. Chem. Phys.* **72** (1980) 1851.
118. T. Nonn, T. Plakhotnik, *Phys. Rev. Lett.* **85** (2000) 1556.
119. C. B. Harris, *J. Chem. Phys.* **67**, 5607 (1977).
120. E. Barkai, R. Silbey, G. Zumofen, *Phys. Rev. Lett.* **84**, 5339 (2000).
121. P. W. Anderson, *Phys. Rev.* **76**, 647 (1949).
122. P. W. Anderson, P. R. Weiss, *Rev. Mod. Phys.* **25**, 269 (1953).
123. S. Bloom, H. Margenau, *Phys. Rev.* **90** (1953) 791.
124. P. de Bree, D. A. Wiersma, *J. Chem. Phys.* **70**, 790 (1979).
125. P. Reineker, H. Morawitz, K. Kassner, *Phys. Rev. B* **29**, 4646 (1984).
126. H. de Vries, D. A. Wiersma, *J. Chem. Phys.* **72** (1980) 1851-63.
127. R. Silbey, K. Kassner, *J. Lumin.* **36**, 283 (1987).

128. R. G. DeVoe and R. G. Brewer, *Phys. Rev. Lett.* **50**, 1269 (1983).
129. A. I. Burshtein, A. A. Zariikov, V. S. Malinovsky, *Phys. Rev. A* **43**, 1538 (1990).
130. S. Ya. Kilin, A. P. Nizovtsev, *Phys. Rev. A* **42**, 4403 (1990).
131. E. Geva, R. Kosloff, J. L. Skinner, *J. Chem. Phys.* **102**, 8541 (1995).
132. D. E. McCumber and M. D. Sturge, *J. Appl. Phys.* **34**, 1682 (1963).
133. T. J. Aartsma and D. A. Wiersma, *Chem. Phys. Lett.* **42**, 520 (1976).
134. A. I. M. Dicker, J. Dobkowski, and S. Völker, *Chem. Phys. Lett.* **84**, 415 (1981).
135. W. P. Ambrose, T. Basché, and W. E. Moerner, *J. Chem. Phys.* **95**, 7150 (1991).
136. F. Jelezko, B. Lounis, and M. Orrit, *J. Chem. Phys.* **107**, 1692 (1997).
137. A. Yariv, *Quantum Electronics* (Wiley, New York, 1967).
138. B. Kozankiewicz, J. Bernard, M. Orrit, *J. Chem. Phys.* **101** (1994) 9377-83.
139. T. Basché, W. P. Ambrose, W. E. Moerner, *J. Opt. Soc. Am. B.* **9** (1992) 829-36.
140. P. J. Flory, *Pure. Appl. Chem.* **56** (1984) 305-12.
141. L. Fleury, et.al., *J. Phys. Chem. B* **101** (1997) 7933.
142. J. J. Macklin, J. K. Trautman, T. D. Harris, L. E. Brus, *Science* **272** (1996) 255.
143. F. Güttler, T. Irngartinger, T. Plakhotnik, A. Renn, U. P. Wild, *Chem. Phys. Lett.* **217** (1994) 393-97.
144. J. Jazny, J. Sepiol, T. Irngartinger, M. Traber, A. Renn, U. P. Wild, *Rev. Sci. Instrum.* **67** (1996) 1425-30.
145. R. van den Berg, A. Visser, S. Völker, *Chem. Phys. Lett.* **144** (1988) 105.
146. D. W. Pack, L. R. Narasimhan, M. D. Fayer, *J. Chem. Phys.* **92** (1990) 41.
147. R. Silbey, J. Koedijk, S. Voelker, *J. Chem. Phys.* **105** (1996) 901.
148. S. Hunklinger, M. Schmidt, *Z. Phys.* **54**, (1984) 93
149. B. M. Kharlamov, D. Haarer, S. Jahn, *Optics and Spectroscopy* **76** (1994) 302.
150. E. Geva, J. L. Skinner, *J. Chem. Phys.* (1997).
151. W. Lukosz, R. E. Kunz, *Opt. Commun.* **20** (1977) 195.
152. D. W. van Krevelen, *Properties of polymers*, 3rd ed. Elsevier, Amsterdam, 1990.
153. D. Dab, A. Heuer, R. Silbey, *J. Lumin.* **64** (1995) 95 .
154. V. Hizhnyakov et al., *J. Lumin.* **72-74** (1997) 415 .

References

155. E. A. Donley, H. Bach, U.P. Wild, and T. Plakhotnik, *J. Phys. Chem.* **103** (1999) 2282.
156. J. K. Trautman, J. J. Macklin, *Chem. Phys.* **205** (1996) 221.
157. M. Prummer et al., *Anal. Chem.* **72** (2000) 443.
158. X. Zhuang, L.E. Bartley, H.P. Babcock, R. Russell, T. Ha, D. Herschlag, S. Chu, *Science* **288** (2000) 2048.
159. H.P. Lu, X.S. Xie, *Nature* **385** (1997) 143.
160. S. M. Barnett, B. Huttner, R. Loudon, *Phys. Rev. Lett.* **68** (1992) 3698.
161. P. F. Jones, *J. Chem. Phys.* **18** (1968) 5444.
162. Th. Sesselmann, W. Richter, D. Haarer, *Europhys. Lett.* **2** (1987) 947.
163. M. Orrit, J. Bernard, A. Zumbusch, R. I. Personov, *Chem. Phys. Lett.* **196** (1992) 595.
164. E. A. Donley, T. Plakhotnik, *Single Molecules* **2** (2001) 23.
165. H. C. Longuet-Higgins, J. A. Pople, *J. Chem. Phys.* **88** (1988) 3516.
166. S. Basu, in *Advances in Quantum Chemistry*, P.-O. Löwdin ed. Academic Press, New York 1964, Vol. 1 pp. 145-169.
167. E. A. Donley, T. Plakhotnik. *J. Chem. Phys.* **114** (2001).
168. A. Ekert, R. Jozsa, *Rev. Mod. Phys.* **68** (1996) 733-53.

Lebenslauf

Persönliche Angaben

Taras Plakhotnik

Geschlecht: Männlich

Geburtsdatum: 26.2.1961

Zivilstand: Verheiratet mit Simonchik Elena am 27.1.1990

Kinder: Tochter Xenia, geboren am 19.4.1991

 Tochter Elizaveta, geboren am 12.11.2000

Nationalität: Russisch

Sprachen: Ukrainisch, Russisch, Englisch (alle fließend), Deutsch (etwas)

Ausbildung

1968-1977. Primar- und Gymnasialbildung in Kiev. Abschluss mit Auszeichnung (*Goldmedaille des Erziehungsministeriums*).

1977-1983. Physikausbildung mit Diplomabschluss mit Auszeichnung am "Moscow Institute for Physics and Technology". Titel: "Experimental study of the intracavity laser spectroscopy method".

1992. Doktorarbeit am "Institute for Spectroscopy of the Russian Academy of Science". Titel: "Comparative study of the high resolution spectra of complex organic molecules cooled in a supersonic free jet and in a crystalline matrix".

Berufstätigkeit

1983-1992 und 1994-1995. Institute for Spectroscopy of the Russian Academy of Science.
 Ingenieur, Juniormitglied des technischen Stabs. Mitglied des wissenschaftlichen Stabs.

1992-1994 und 1995-1997. Akademischer Gast an der ETH Zürich in der Gruppe von Prof. Urs. P. Wild.

seit September 1997 Oberassistent am Laboratorium für Physikalische Chemie der

ETH Zürich.